Une étude expérimentale de la coercivité des aimants NdFeB

Georgeta Ciuta

UNIVERSITÉ DE GRENOBLE

THÈSE

Pour obtenir le grade de

DOCTEUR DE L'UNIVERSITÉ DE GRENOBLE

Spécialité : **Physique des materiaux**

Arrêté ministériel : 7 août 2006

Présentée par

Georgeta CIUTA

Thèse dirigée par **Dominique GIVORD**
codirigée par **Nora DEMPSEY**

préparée au sein de l'**Institut Néel**
dans **le Collège Doctorale de l'Université de Grenoble**

Une étude expérimentale de la coercivité des aimants NdFeB

Thèse soutenue publiquement le **12 juillet 2013**
devant le jury composé de :

Viorel, POP
Prof., Universitatea Babeş-Bolyai Cluj-Napoca, Roumanie, Rapporteur
Volker, NEU
Senior Scientist, Institute for Metallic Materials dpt. Magnetic Microstructures, Dresden, Allemagne, Rapporteur
J.M.D., COEY
FRS, Trinity College, Dublin, Irlande, Membre
Manabe, AKIRA
Ingénieur, Toyota Motor Corporation, Japon, Membre
Alain, SCHUHL
Prof., Institut Néel CNRS/UJF UPR 2940, Grenoble, France, Membre
Dominique, GIVORD
Dr., Institut Néel CNRS/UJF UPR 2940, Grenoble, France, Directeur de thèse
Nora, DEMPSEY
Dr., Institut Néel CNRS/UJF UPR 2940, Grenoble, France, Co-directeur de thèse

Université Joseph Fourier / Université Pierre Mendès France / Université Stendhal / Université de Savoie / Grenoble INP

Acknowledgements

The present manuscript is the result of 3 years of work and the contribution of many people. In this section I would like to address a few thoughts to people that, at some moment, helped me from a personal, scientific and/or financial point of view.

So, starting with the end, I would like to thank the members of the jury that were present during my thesis defense: Viorel Pop, Volker Neu, J. M. D. Coey, Manabe Akira and Alain Schuhl.

Going back to the beginning, Nora and Dominique, thank you for trusting in me (enough) back in 2010 to start a thesis together. I remember the discussion we had with Nora in the exact place showed in the image below just a few months after starting my PhD. You were saying that, if Dominique trusted me enough to propose me a thesis there should be a reason. No matter what that reason was, I am glad it happened.

2010, Tokyo Imperial Palace garden.

Special thanks to my "stepsupervisor" Olivier Fruchart for the rich and fruitful collaboration.

Frédéric, just for the records, when I will be famous I want people to know that sharing the office with you for most of the thesis was one of the important things keeping me rolling. Thank you for your encouragement and motivational speeches. And yes, I know what the capital of Denmark is.

Talking about office colleagues, Nilay, Ozan …even if office colleagues for a short time, it was love at first sight. You are great both of you (you too Ozan ☺). Actually, you are the witness (at work) of me writing my thesis. If we survived that period together, I think we can do anything together. Especially for the way you helped me in the last months, I want to thank you and….bisous bisous. I am not afraid of turks anymore.

Richard, I was really lucky to meet you in the beginning of my thesis. During all the work we did together (all the times I bothered you) I discovered a very nice person and I am sure we will meet again for some salată de boeuf cu pui. Mulțumesc. A fost o adevărată plăcere. Brenda.

Luiz, dear Luiz. You are the first person I saw when I came in Grenoble, in the lab the first day. You and Dominique. What can I say? Maybe "Shut up Luiz!".

Damien ca va? Il fait beau, plein du soleil. Thank you for being so sporty and motivating me also to go running every now and then…mostly tomorrow. Even if you

don't know (yet) to appreciate the beauty (I am talking about Romania of course), hey, thanks for the laugh, scientific and non-scientific discussions.

Dmitry you're next. That's all I say. And maybe…yes, thanks for the Russian approach during coffee breaks, we all learned something.

Tim, thanks for the daily "Geta, are you nervous?" for the period before defense. You can not imagine how much it helped.

André, when I first met you I found you weird. I mean, you are weird but in a nice way. You gave life to our team with your over - exaggerated life experiences. I think I will miss the type of questions only you could ask.

Filippo, we did a good decision when we adopted you. Thanks for the coffees and don't forget to clean your office. It's a mess!!

I am also thanking the team of engineers (Didier, Eric, Laurent, Yves and all the others) for their continuous help. In the same time, I want to mention the administration (Sabine, Veronique, Marielle) that answer my questions and helped to survive the paper work.

Ancuța, cealaltă Ancuța (Teo respectiv), un regret am: că nu ne-am văzut în momentul de fericire, la final. Sper să fie cazul la voi, nu știm niciodată. In rest, se știe, fără multe cuvinte că suntem dure. Sur le pont d'Avignon.

Vreau să mulțumesc de asemenea familiei mele pentru încredere și suport de-a lungul întregilor ani de studiu. Nicu, cred că ar fi fost mult mai greu fără încurajările din partea ta. Reprezentanților la susținere, Iulia & co., vă mulțumesc pentru participare, ajutor și voie bună. Bon dimanche! Nice to meet you!

And now, to my personal coach… "C'est bientot fini". This is the sentence that brought me to the end. I am trained now to write thesis and prepare speeches and more. Merci pour tout et pour me supporter. Douăzeci.

I would like to acknowledge Toyota Motor Corporation for the financial support.

TABLE OF CONTENTS

General Introduction

The discovery of the NdFeB magnets in 1983[1,2,3,4,5] was immediately recognized as an important step in the history of permanent magnets development. The permanent magnetic industry was, at that time, largely dominated by the ferrite magnets, discovered in the Philips laboratories in the 50's. SmCo magnets occupied niche markets, perhaps 5% in value. Their main applications were military, in Travelling Wave Tubes and high performance servo - motors. They had succeeded in entering one large-consumer application, the earphone of the Walkman. NdFeB magnets had strong advantages compared to SmCo: they had larger magnetization, neodymium was much less expensive than samarium and even more important, Fe is one of the most common elements in nature whereas Co was a strategic and expensive material. It was predicted at that time that the NdFeB production would reach 3000 Tons in the year 2000. At that date, the real figure was already 3 times more than the prediction. The NdFeB magnets were essentially used in the voice coil motors of hard disk drives. Other applications concerned high performance motors and MRI magnets.

Since then, the development of the NdFeB magnets has continued beyond all predictions. The energy density of an electrical machine that contains NdFeB magnets is significantly higher than that of a similar machine with a wound rotor. Higher energy density means lighter machines. This is of primordial importance in applications where energy consumption is critical. Toyota Motor Corporation (TMC) has incorporated NdFeB magnets in the motor and the generator of the Prius. A new application of the NdFeB magnets emerges in motors of wind turbines. It permits reducing substantially the weight of the nacelle and requires a much lower generator speed than motors with wound rotor.

In high-performance motor applications, the magnet temperature may reach values of 160 °C - 180 °C. At such temperature the anisotropy of the $Nd_2Fe_{14}B$ is very strongly reduced and with it, the coercivity which represents the resistance of a magnet to demagnetization. A fraction of the neodymium is replaced by dysprosium to preserve sufficient coercivity at the operating temperature. The Dy moments couple antiparallel to the Fe ones, which leads to a very substantial reduction in the material's magnetization. Furthermore, Dy is much more expensive than Nd.

During the last years, it was understood that the development of NdFeB magnets in these very large scale applications will require new processes, permitting the properties of today's magnets to be obtained in new materials which would not contain any dysprosium, to be developed. Various initiatives with this goal have been launched throughout the world. The work presented in this thesis has been developed in the framework of a collaborative action initiated by TMC, and gathering additionally the IFW Dresden and the University of Sheffield. The global objective of this action was to progress in our understanding of coercivity of real materials. The fundamental activity included preparation of model systems, microstructural characterization, magnetic characterization and modeling.

The work presented here concerns essentially 2 different families of NdFeB magnets. The first family consists of thick hard magnetic films deposited by triode sputtering. In contrast to thin magnetic films, the film thickness here is typically 10 times larger than the grain size and thus the materials obtained present a microstructure characteristic of "bulk" materials. The control of the various parameters involved in the material preparation permits controlling the grain size and shape of the grains more easily than in the usual processes used for magnet preparation. These systems can thus be seen as models to study the nature of the links existing between material's microstructure and hard magnetic properties and we have studied more particularly two samples having distinctly different properties.

The second type of material studied is that of bulk materials prepared in the Toyota laboratories. The Toyota research group has developed an original approach in which a given magnet is submitted to an infiltration process with a low melting temperature alloy, which diffuses easily into the grain boundaries. By this process, the coercive properties are progressively, and very significantly, improved, although the grain shape and size remain little affected. A total of 5 samples (the precursor + 4 infiltrated magnets) have been studied in this thesis.

The present work being centered on the study of coercivity in NdFeB hard magnets, we have applied usual analyses, i.e. measurement of the temperature dependence of the coercive field, of its angular dependence and of the activation volume. We have tried as well to enlarge the scope of experimental tools. This has included measurements of minor loops, which have been little explored until today and MFM observations in different remanent states. Beyond the information on the physical mechanisms involved, we have examined whether the parameters extracted from the analysis of the coercivity could be used to characterize materials in a phenomenological manner.

The present manuscript is organized as follows:

- A brief general introduction on permanent magnets is presented in the first chapter. The parameters characterizing magnets are explained, the various types of magnetic materials are presented, the REFeB magnets more particularly.
- Coercivity is described in chapter II. The classical coherent rotation model is explained, and more importantly why real materials do not follow coherent rotation. The models used to characterize coercivity in real materials are described and the hypotheses that sustain them are given.
- Film preparation and other experimental tools used in the context of this work are presented in chapter III. Most important in terms of personal involvement has been thick film preparation using the high deposition rate triode sputtering equipment of Institut Néel. I have also had a strong personal involvement in MFM analysis, with the objective of going beyond qualitative observation.
- Chapter IV is concerned with the experimental analysis of the two families of magnets presented above. An important aspect has been to try understanding the meaning of the values of the parameters and its implication in the physics of the reversal mechanisms.

- Chapter V is focused on an MFM analysis of the thick film magnets during reversal. Very different behaviors are identified, distinguishing weak and strong coercivity materials. The results of these observations are also related to those of the coercivity analysis in chapter IV.
- The main results of this work are recalled in the conclusions. New directions of research are suggested to progress further in the understanding of magnetization processes in hard magnetic materials.
- At the end of the manuscript, complementary information is given in the Annex section.

---

[1] G. C. Hadjipanayis, R. C. Hazelton and K. R. Lawless, Appl. Phys. Lett. 43, 797 (1983);

[2] M. Sagawa, S. Fujimura, N. Togawa, H. Yamamoto and Y. Matsuura, J. Appl. Phys. 55(6), 2083 (1984);

[3] N. C. Koon and B. N. Das, J. Appl. Phys. 55, 2063 (1984);

[4] G. C. Hadjipanayis, R. C. Hazelton and K. R. Lawless, J. Appl. Phys. 55, 2073 (1984);

[5] J. J. Croat, J. F. Herbst, R. W. Lee and F. E. Pinkerton, J. Appl. Phys. 55, 2078 (1984).

I. Introduction

I.1 Characteristics of hard magnetic materials

The performance of a magnetic material is established by measuring the change of its magnetization as a function of a varying applied field, i.e. measuring its hysteresis loop, **Fig. 1. 1** (left). If an increasing magnetic field is applied, the magnetization of the sample will increase and tend towards a maximum, hypothetical value, the saturation magnetization. When the field is reduced, the magnetization decreases, reaching a value of M_r named the remanent magnetization in zero magnetic field. If the field is then applied in the opposite direction, the magnetization will be reduced to zero for a value of the field called the coercive field, H_c.

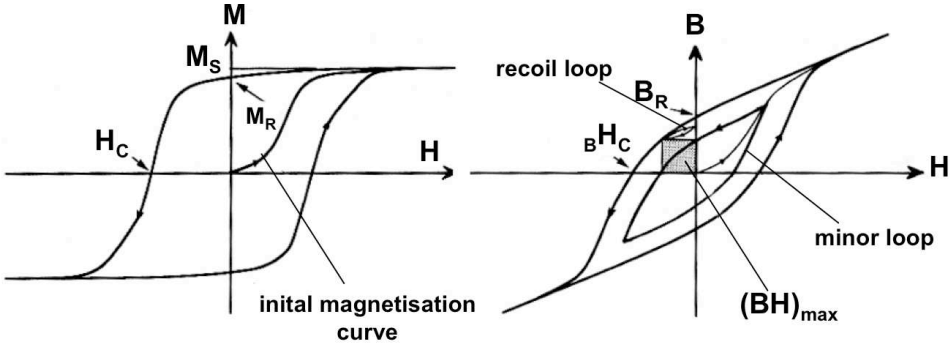

Fig. 1. 1 M (H) (left) and B (H) (right) loops of a permanent magnet.

The remanent magnetization and the coercive field are the two most important parameters that characterize a magnet. A figure of merit typically used to compare different magnets is the maximum energy product, $(BH)_{\max}$, where $B = \mu_0(M + H)$ is the magnetic induction. The product $(BH)_{\max}$ is equal to the maximum of the B and H product, calculated in the 2nd quadrant of the B(H) loop (**Fig. 1. 1**b). It represents the maximum energy that, for a magnet of given volume, can be transformed into work, in a machine that uses such a magnet. Its maximum possible value for an ideal system is $\frac{\mu_0 M_s^2}{4}$, where the spontaneous magnetization (M_s) is the magnetization within a magnetic domain at zero total field.

Most generally, hard magnetic materials present directions that are energetically favorable to the orientation of the magnetization (easy axis magnetization). This is called magnetic anisotropy. The origin of the anisotropy can be either the shape of individual magnetic entities constituting the magnet (shape anisotropy) or the crystalline structure of the involved hard magnetic material (magneto - crystalline anisotropy).

M_r and H_c depend on the one hand on some intrinsic parameters (Spontaneous magnetization (M_s) and Anisotropy field (H_A)) and on the other hand, on the magnet's microstructure. M_r is always smaller than M_s due to grain misalignment and the presence of secondary phases. The dependence of coercivity on the microstructure is not as obvious and it will be discussed more later on.

I.2 Hard magnetic materials

The materials developed to produce permanent magnets are (chronologically): steel alloys, Alnicos, ferrites and rare earth permanent magnets. Before the ferrites were discovered, the magnets needed to be U - shaped, horseshoe - shaped or in the form of long bars, in order to minimize the self-demagnetizing field (shape anisotropy magnets). With the ferrites, which exploit magneto-crystalline anisotropy, the shape constraint was eliminated since these materials had, irrespective of their shape, coercivities bigger than their own demagnetizing field.

$(BH)_{max}$ increased continuously during the 20th century, **Fig. 1. 2**. This was a result of: a) discovery of new materials and b) improvement in processing of already known materials. A big leap was made in the 60s when the RE-TM alloys were discovered. These magnets are characterized by strong magneto-crystalline anisotropy (coming from the RE element) and good magnetization and Curie temperature (from transition metal). SmCo magnets were the first class of RE-TM magnets to be developed. 20 years later, another important step was made with the discovery of $Nd_2Fe_{14}B$-based magnets. The spontaneous magnetization of the $Nd_2Fe_{14}B$ phase is higher than that of the $SmCo_5$ and Sm_2Co_{17} phases involved in the Sm-Co magnets (**Table 1. 1**) thus the increase in maximum energy product.

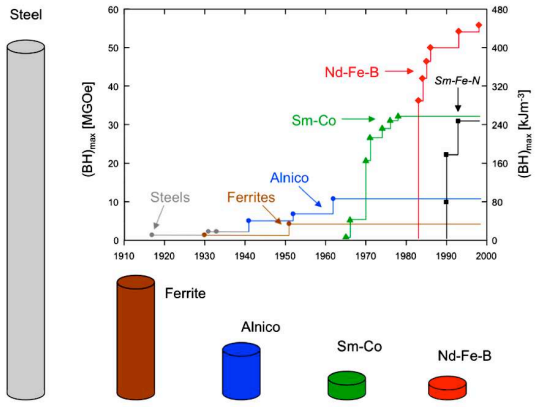

Fig. 1. 2 Evolution in time of $(BH)_{max}$.and schematic presentation of different types of materials with comparable energy density.

The intrinsic properties of some permanent magnets, at 300 K, are compared to those of Fe in **Table 1. 1**.

Material	$\mu_0 M_s$ (T)	K_1 (kJ/m^3)	$\mu_0 H_A$ (T)	$(BH)_{max}$(kJ/m^3)*	T_C (K)
Fe	2.15	0.048	-	-	1044
$BaFe_{12}O_{19}$	0.48	0.33	-	45	740
FePt	1.43	6	11.6	406	750
$SmCo_5$	1.07	17.2	40	231	1020
Sm_2Co_{17}	1.2	4.2	8.5	294	1190
$Nd_2Fe_{14}B$	1.61	4.9	7.7	512	588

Table 1. 1 Intrinsic properties corresponding to some of the permanent magnets, at 300 K[1, 2].

* $(BH)_{\max} = \mu_0 M_s^2 / 4$

I. 3 RE-Fe magnets

The outstanding properties of $RE_2Fe_{14}B$ compounds are given mainly by the strong magneto-crystalline anisotropy provided by the RE element. As what concerns magnetization, the alloys formed with light rare earths (LREE) possess a high magnetization because the Fe magnetic lattice couples parallel with the RE magnetic lattice. On the contrary, the heavy rare earth elements (HREE) align anti-parallel with Fe giving a much-reduced overall magnetization[17]. However, HREE-TM alloys have the advantage of higher H_A (e.g. H_A ($Dy_2Fe_{14}B$) = 15 T; H_A ($Nd_2Fe_{14}B$) = 6.7 T).

From all the possible compounds, the one with Nd, a LREE, has the highest spontaneous magnetization. It implies that these magnets have the potential of achieving the highest maximum energy product.

The $Nd_2Fe_{14}B$ compound crystallizes in a tetragonal structure, space group $P_4$2/mnm[3,4,5]. The lattice parameters are a = 8.8 Å and c = 12.2 Å[6] and the magnetization easy axis is along c-axis above 135 K. The easy axis starts to tilt away from the c-axis below 135 K[7,8]. The angle between the easy axis and c-axis increases progressively from around 0° at T = 135 K to 30° at T = 4.2 K[9].

I.4 Processing of NdFeB - based magnets

The main processing routes for NdFeB - based magnets are schematically shown in **Fig. 1. 3**[33].

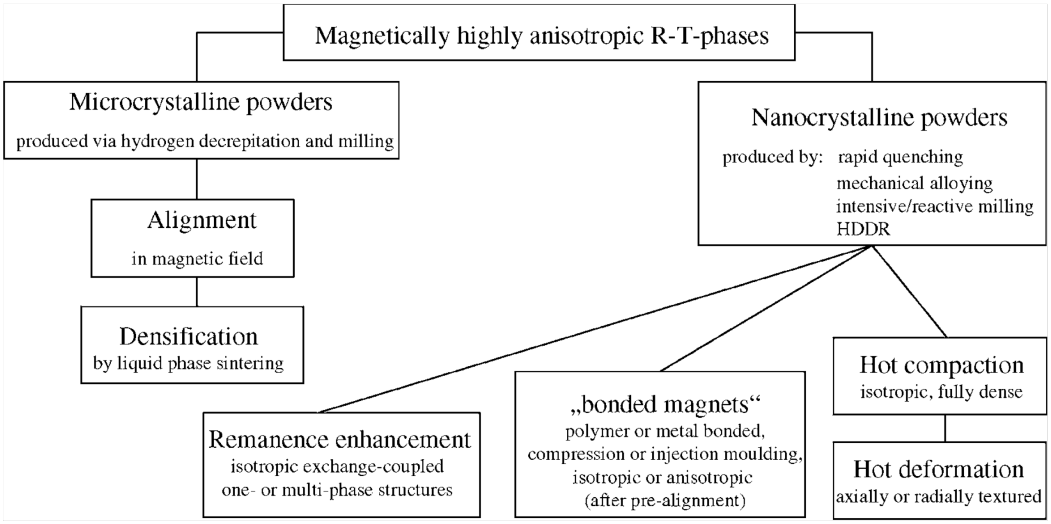

Fig. 1. 3 Principal routes followed to process highly anisotropic R-T phases (thus NdFeB)[33].

The process of making magnets starts always by alloying the individual elements (typically using induction melting). The next step is the powder production from the melted alloy. Using hydrogen decrepitation and milling, a microcrystalline powder is obtained. This powder is then aligned in magnetic field and compacted. These are the sintered magnets.

A second possibility is to make nano-crystalline powder from the starting alloy (e.g. rapid quenching + milling of the resulting ribbons). This powder can be

compacted as it is or mixed with a polymer (or a metal) producing the so-called "bonded magnets".

The highest $(BH)_{max}$ is obtained in anisotropic sintered NdFeB-magnets.

NdFeB has been prepared also in film form using both sputtering[10,11,12,13,14] and Pulsed Laser Deposition[15,16] techniques. Thin films have potential applications in data storage, while thicker films are being developed for use in micro-systems. The microstructure of the hard magnetic layer may be controlled to a certain extent, through a control of preparation conditions. This allows an optimization of the extrinsic properties, and makes films good candidates for studying magnetization reversal.

I.5 NdFeB - based magnets. State of the art

Energy applications, like hybrid electric vehicles (HEV) and windmills, are becoming more and more important. For permanent magnet based devices, there is a need for magnetic materials with high $(BH)_{max}$ operational up to high temperature (180 °C). As discussed previously, NdFeB magnets have the highest $(BH)_{max}$ so they are appealing for this kind of application. The problem is that above 100 °C, the coercivity of NdFeB is decreases rapidly with temperature so that at the maximum working temperatures, the H_c of NdFeB is not sufficient. In order to obtain enough coercivity at high temperatures, an increase of H_c at room temperature is needed.

One way of improving coercivity of NdFeB-based magnets is to increase the anisotropy field by adding HREE like Dy as $Dy_2Fe_{14}B$ has much higher anisotropy field than $Nd_2Fe_{14}B$. In this case, a part of Nd atoms in the 2:14:1 phase are replaced with Dy atoms. The inconvenience of Dy addition is the decrease of saturation magnetization caused by the antiparallel alignement of Dy magnetic moments and Fe magnetic moments[17]. The second problem with the Dy is its cost, heavy rare earth, being more expensive than the light rare earths. In this specific case, Dy is approximately 10 times more expensive than Nd. What is more, Dy is a strategic element, with most of the known resources concentrated in China.

In order to reduce the amount of Dy, the introduction of this element only at the grain surface is a solution. In these magnets the reversal is thought to start at defects present at grain boundaries. By increasing H_A at the grain surface, the coercivity should be increased. Two main techniques are used: the two powders technique and grain boundary diffusion. In the first case, a mixture of two powders ($Nd_2Fe_{14}B$-based powder and Dy-based powder) is generally aligned under magnetic field, pressed, sintered at temperatures around 1000°C and annealed at lower temperatures. The second powder can be for example Dy_2O_3[18,19,20], DyH_x[21], DyGa[22] or Dy_2S_3[23]. The resultant microstructure can be considered as made of core-shell grains separated by secondary phases. The core is typically 2:14:1 Dy- free, the shell 2:14:1 with some Nd atoms being replaced by Dy atoms and the intergranular phases differ from one composition to another. The thickness of the Dy-rich shell can, sometimes, be bigger than the size of the Dy-free core in which case the amount of Dy is still high.

In 2005, another technique, grain boundary diffusion (GBD) was reported[24,25]. Dy-free sintered NdFeB-based magnets are coated with Dy-based powders (Dy_2O_3, DyF_3) and then heat-treated. In this case Dy is diffused along the grain boundaries, forming a thin shell of $(NdDy)_2Fe_{14}B$ around the $Nd_2Fe_{14}B$ grains and O and F form intergranular oxides with Nd. The thin shell has an increased anisotropy and it has a positive effect on the H_c of these magnets. The amount of Dy is significantly reduced compared to other techniques and the decrease of remanent magnetization is almost zero. Hirota et al.[25] report a decrease of M_r with 7% in the case of two powders technique and only 0.2% when GBD was used.

Alternatively, NdFeB-based magnets (with no Dy) were coated with a sputtered layer of pure Dy and then annealed to allow Dy diffusion at the grain interfaces[26]. Ding et al.[27] reported an increase in coercivity with preservation of remanence in magnets obtained by sintering of ribbons obtained from arc melting of a NdFeB-based alloy. Prior sintering, the ribbons were immersed in a mixture of DyF_3 powder and ethanol, dried and annealed.

Recently, Li et al.[28] studied the distribution of Dy in a commercial magnet using SEM, TEM and 3DAP analysis. They suggest that the problem is not as simple as thought. The increase of coercivity after addition of Dy might be due to the anisotropy increase but not only. The intergranular phases are also different (magnetically) and they could help in decoupling better the grains. It is clear that the study related to Dy in NdFeB magnets is still an important one and efforts for understanding in more detail what happens with Dy addition are still ongoing.

Another way of increasing the H_c is by improving the microstructure. It is known that the coercivity increases when the grain size decreases (down to a few 10's of nm). In sintered magnets, below 3 μm grain size the coercivity is lowered due to oxidation. Using the so-called pressless process (PLP), Sagawa et al. managed to obtain magnets with high H_c and grain size < 3 μm under Ar atmosphere[29].

In magnets based on NdFeB the intergranular phases play an important role. There are two major types of secondary phases considered [30]: i) very thin (1-2 nm) metallic Nd-rich phases separating the main phase grains and ii) crystalline oxides (Nd_2O_3, NdO)[31] at triple junction points.

The exact chemical composition of the first type of secondary phase is difficult to identify, considering the small sizes implied. Nevertheless, important progress was made in the last years due to high-resolution characterization techniques like TEM and atom probe. It is commonly believed that the thin layer separating neighboring grains is non-magnetic and it enhances coercivity via magnetic decoupling of the grains[32,33,34]. More recently, Sepehri-Amin et al.[35] detected iron in the thin grain boundary using atom probe elemental analysis. They prepared a thin layer of the same composition as the one detected at the grain boundaries and they concluded that the phase is a soft magnetic one with a saturation magnetization of ≈ 440 emu cm^{-3}. In this case, the magnetization reversal mechanism must be different. They suggest that the 2:14:1 grains are magnetically coupled via the grain boundary phase which act to pin domain walls.

The coercivity of NdFeB - based magnets can be also increased by improving the magnetic decoupling of the 2:14:1 phase. This is typically done by adding non - magnetic elements that preferentially stay at the grain boundary. The most used element for this purpose is Cu.

The effect of Cu on the magnetic properties of NdFeB was already studied in different kinds of magnets: i) sintered magnets obtained starting from a NdFeBCu-based powder[36,37,38,39]; ii) sintered magnets obtained starting from a mixture of NdFeB - based powder and Cu powder[40,41,42,43,44,45]. The general conclusion of all of these studies, indifferent of the exact composition, starting powder size, final grain size etc. is the same: the addition of Cu improves coercivity of NdFeB-based magnets by the formation of additional inter-granular phases (with Nd and/or O) that decouple the 2:14:1 grains. The presence of the low temperature eutectic $NdCu_2$ facilitates the formation of a continuous inter-granular phase. Recently, S. Sepehri-Amin et al., reported another way of introducing Cu in the magnets, using NdCu powder[46]. They start from a mixture of NdFeB-based and NdCu powders and get magnets with 2:14:1 nano-sized grains enveloped in a Nd-rich (Cu containing) phase. Coercivity of 2.6T was obtained. The Toyota Motor Corporation developed the so-called infiltration process in order to introduce Cu to the Nd-rich grain boundaries[47]. Details about this process are given in chapter III.

It is clear that the microstructure has a decisive role in the coercivity mechanism of NdFeB-based magnets. Nevertheless, the exact nature of the microstructure - coercivity link is not understood and as already mentioned, its study has been one of the important objectives of this thesis.

[1] J. M. D. Coey, Magnetism and Magnetic materials book, Cambridge, 2010, 614p;

[2] C. Ndao , PhD thesis (2010);

[3] J. F. Herbst, J. J. Croat, F. E. Pinkerton and W. B. Yelon, Phys. Rev. B 29, 4176 (1984);

[4] D. Givord, H. S. Li and J. M. Moreau, Sol. State Comm. 50, 497 (1984);

[5] C. B. Shoemaker, D. P. Shoemaker and R. Fruchart, Acta Cryst. C 40, 1665 (1984);

[6] C. Abache and H. Oesterreicher, J. Appl. Phys. 57, 4112 (1985);

[7] D. Givord, H. S. Li, J. M. Moreau, R. Perrier de la Bâthie and E. Du Trémolet de Lacheisserie, Physica B 130, 323 (1985);

[8] D. Givord, H. S. Li and R. Perrier de la Bâthie, Sol. State Comm. 51, 857 (1984);

[9] M. Sagawa, S. Fujimura, H. Yamamoto, Y. Matsuura and S. Hirosawa, J. Appl. Phys. 57(1), 4094 (1985);

[10] F. J. Cadieu: In Physics of Thin Films, Francombe, M., Vossen, J. (eds.) vol. 16, Academic Press Inc., (1992);

[11] B. A Kapitanov, N.V Kornilov, Ya. L Linetsky and V. Yu Tsvetkov, JMMM 127, 289-297 (1993);

[12] S. Parhofer, G. Gieres, J. Wecker, and L. Schultz, J. Magn. Magn. Mater. 163, 32 (1996);

[13] L. K. E. B. Serrona, R. Fujisaki, A. Sugimura, T. Okuda, N. Adachi, H. Ohsato, I. Sakamoto, A. Nakanishi, M. Motokawa, D. H. Ping, and K. Hono, J. Magn. Magn. Mater. 260, 406 (2003);

[14] N. M. Dempsey, A. Walther, F. May and D. Givord, Appl. Phys. Lett. 90, 092509 (2007);

[15] U. Hannemann, S. Fähler, V. Neu, B. Holzapfel, and L. Schultz, Appl. Phys. Lett. 82, 3710 (2003);

[16] Nakano, M., Katoh, R., H. Fukunaga. Fabrication of Nd–Fe–B Thick-Film Magnets by High-Speed PLD Method. IEEE Trans. Magn. 39, 2863-2865 (2003);

[17] I. A. Campbell, J. Phys. F 2, L47 (1972);

[18] M. Doser and G. Keeler, J. Appl. Phys. 64, 5311 (1988);

[19] F. Z. Lian, L. Ai, X. S. Zhang and H. H. Zhao, JMMM 127, 190 (1993);

[20] L. Li, J. Yi, Y. Peng and B. Huang, JMMM 308, 80 (2007);

[21] R.S. Mottram, A. Kianvash and I. R. Harris, J. Alloys Comp. 283, 282(1999);

[22] C.H. de Groot, K. H. J. Buschow, F. R. de Boer and K. de Kort, J. Appl. Phys. 83, 388 (1998);

[23] A. M. Gabay, M. Marinescu, W. F. Li, J. F. Liu and G. C. Hadjipanayis, J. Appl. Phys. 109, 083916 (2011)

[24] H. Nakamura, K. Hirota, M. Shimao, T. Minowa and M. Honshima, IEEE Trans. Magn. 41, 3844 (2005);

[25] K. Hirota, H. Nakamura, T. Minowa and M. Honshima, IEEE Trans. Magn. 42, 2909 (2006);

[26] D. Li, S. Suzuki, T. Kawasaki and K-i. Machida, Jpn. J. Appl. Phys. 47, 7876 (2008);

[27] Y. Ding, R. J. Chen, Z. Liu, D. Lee and A. R. Yan, J. Appl. Phys. 107, 09A726(2010);

[28] W.F. Li, H. Sepehri-Amin, T. Ohkubo, N. Hase and K. Hono, Acta Mat. 59, 3061 (2011);

[29] M. Sagawa, in: S. Kobe, P.J. McGuinness (Eds.), Proceedings of the 21st Workshop on Rare-Earth Permanent Magnets and their Applications, Jozef Stefan Institute, Ljubliana, Slovenia, p183 (2010);

[30] T. G. Woodcock, Y. Zhang, G. Hrkac, G. Ciuta, N. M. Dempsey, T. Schrefl, O. Gutfleisch and D. Givord, Scripta Materialia 67, 536 (2012);

[31] T. G. Woodcock and O. Gutfleisch, Acta Mat. 59, 1026 (2011);

[32] M. Sagawa, S. Fujimura, N. Togawa, H. Yamamoto and Y. Matsuura, J. Appl. Phys. 55(6), 2083 (1984);

[33] O. Gutfleisch, J. Phys. D: Appl. Phys. 33, R157 (2000);

[34] F. Vial, F. Joly, E. Nevalainen, M. Sagawa, K. Hiraga and K. T. Park, JMMM 242, 1329 (2002);

[35] H. Sepehri-Amin, T. Ohkubo, T. Shima and K. Hono, Acta Mat. 60, 819 (2012);

[36] A. Kianvash and I. R. Harris, J. Appl, Phys. 70, 6453 (1991);

[37] H. J. Engelmann, A. S. Kim and G. Thomas, Scripta Materialia 36, 55 (1997);

[38] H. Lemke and G. Thomas, Scripta Materialia 37, 1651 (1997);

[39] S. Pandian, V. Chandrasekaran, G. Markandeyulu, K. J. L. Iyer and K. V. S. Rama Rao, J. Appl. Phys. 92, 6082 (2002);

[40] O.M. Ragg and I. R. Harris, J. Alloys Comp. 256, 252 (1997);

[41] A. Yan, X. Song, Z. Chen and X. Wang, JMMM 185, 369 (1998);

[42] R. S. Mottram, A. J. Williams and I. R. Harris, JMMM 234, 80 (2001);

[43] X. G. Cui, M .Yan, T. Y. Ma and L. Q. Yu, Phys. B 403, 4182 (2008);

[44] P. Yi, M. Lin, R. Chen, D. Lee and A. Yan, J. Alloys Comp. 491, 605 (2010);

[45] C. Sun, W. Q. Liu, H. Sun, M. Yue, X. F. Yi and J. W. Chen, J. Mater. Sci. Technol. 28, 927 (2012);

[46] H. Sepehri-Amin, D. Prabhu, M. Hayashi, T. Ohkubo, K. Hioki, A. Hattori and K. Hono, Scripta Mat. 68, 167 (2013);

[47] A. Kato, S. Tetsuya, S. Noritsugu, K. Hideshi and S. Takashi (Toyota Motor Corporation), *High coercive field NdFeB magnet and construction method therefor*, JP2010010665 (2010).

II. Theory of Coercivity

II.1 Origin of Coercivity. Anisotropy.

Coercivity characterizes the resistance of a ferromagnetic (or ferrimagnetic) material to demagnetization. The coercive field refers to the magnetic field needed to bring the magnetization to zero, along a certain direction, once it was previously saturated along that direction.

The classification of magnetic materials into "hard" or "soft" materials is based on the value of the coercive field. The present work is concentrated on hard magnetic materials with H_c values typically higher than 0.1 T.

The intrinsic parameter that governs coercivity is the magnetic anisotropy, which implies the existence of energetically favorable directions for magnetization either related to the crystalline axes – magneto-crystalline anisotropy - or related to the macroscopic shape of the sample – shape anisotropy. The axis corresponding to the lower energy state is called the easy axis while that corresponding to high energy is the hard axis. The physics of anisotropy is explained in several books like for example the ones of G. Bertotti[1], R. Skomski and J.M.D. Coey[2] or lectures of P. Bruno[3].

Further, the case of uni-axial systems with strong anisotropy will be treated since the materials we are studying enter into this category. In this type of system, there is only one easy axis and the anisotropy energy density is approximated to:

$$E(\theta) = K_1 \sin^2\theta + K_2 \sin^4\theta + K_3 \sin^6\theta + \ldots \qquad \textbf{(2. 1)}$$

where K_i is the i-th order anisotropy constant and θ is the angle between the magnetization and the easy axis. Generally, only the first term is considered but there are special cases where the next terms become important as well, especially at low temperature. If (2. 1) is reduced to the first term and $K_1 > 0$, two equivalent energy minima are present, corresponding to $\theta = 0$ and $\theta = \pi$ as seen in **Fig. 2. 1**. This translates into a preference for the magnetization to lie along the z easy-axis, with either the positive or the negative orientation. In the absence of any external magnetic field, the system will occupy one of the two possible states with equal probability.

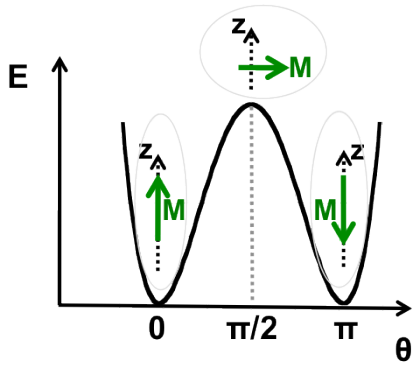

Fig. 2. 1 Schematic of the energy barrier in the case of a uni-axial system with no external applied magnetic field.

The two energy minima are separated by a maximum, at $\theta = \pi/2$. This corresponds to a magnetization hard axis and the energy needed to align the magnetization along any direction perpendicular to the easy axis, is the anisotropy energy.

Consider now that the magnetization is aligned along the easy axis at $\theta = 0$ and a magnetic field is applied along the same axis, at $\theta = \pi$. In the Stoner-Wohlfarth model, the magnetization is assumed to rotate uniformly. The associated energy becomes:

$$E(\theta) = K_1 \sin^2 \theta + \mu_0 M_s H \cos\theta \qquad \textbf{(2. 2)}$$

where M_s is the spontaneous magnetization and H the applied magnetic field.

The energy profile changes accordingly:

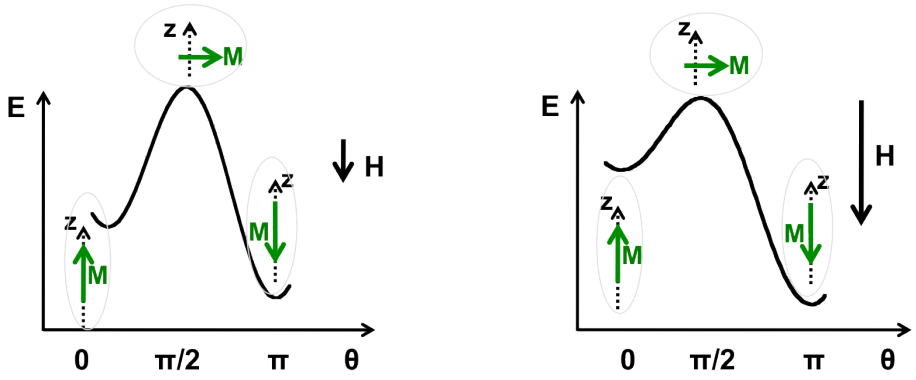

Fig. 2. 2 Evolution of the energy barrier in the presence of an increasing magnetic field.

As the field strength is increased, the energy minimum corresponding to the magnetization anti-parallel to H ($\theta = 0$) is progressively raised whereas the minimum corresponding to the magnetization parallel to H ($\theta = \pi$) is lowered (see **Fig. 2. 2**). In low applied field, the magnetization remains anti-parallel to the field. At $H = H_c$ the energy barrier vanishes and the magnetization flips and aligns along the applied field. In this Stoner-Wohlfarth model, the coercive field is the anisotropy field. We will see below that this model applies only to ideal systems.

In real systems, coercivity is an extrinsic physical property, which depends on the material's anisotropy but is also strongly influenced by the material's microstructure. There are different possibilities for the reversal to happen and they will be discussed in the next section.

II.2 Types of magnetization reversal in uniaxial high anisotropy systems

II.2.1 Nucleation

Nucleation implies the occurrence of instabilities in a saturated magnetic state for a certain value of an applied field, H_N, the nucleation field. In the Stoner-Wohlfarth model, discussed briefly in the first part of this section, the coercive field is equal to the nucleation field. In real systems, reversal begins at defects and it may be decomposed into two stages, nucleation and propagation. The larger of these two fields determines the value of the coercive field. Two cases of nucleation type reversal will be presented and the formula for the corresponding nucleation field will be given.

Coherent rotation. Stoner-Wohlfarth model.

In the Stoner-Wohlfarth (SW) model[4], the magnetization can be considered homogeneous and the magnetic moments parallel at any moment. The model is valid in particular for very small magnetic particles.

We consider that the easy axis is the z-axis and it coincides with the direction of the applied field. The energy density is given by equation (2. 2).

The system will "look for" the position where its energy is minimized. Accordingly, the equality $\partial E / \partial \theta = 0$ gives:

$$2K_1 \sin\theta\cos\theta - \mu_0 M_s H \sin\theta = 0$$

$$\sin\theta(2K_1\cos\theta - \mu_0 M_s H) = 0 \qquad \textbf{(2. 3)}$$

$$\text{if } \sin\theta = 0 \text{ then } E(\theta = 0) \text{ and } E(\theta = \pi) \text{->} E_{\min} \qquad \textbf{(2. 4)}$$

$$\text{if } 2K_1\cos\theta - \mu_0 M_s H = 0 \text{ then } E(\cos\theta = \mu_0 M_s H / 2K_1) \text{->} E_{\max} \qquad \textbf{(2. 5)}$$

Considering that the nucleation field, at which the first instability in the moment configuration will occur, corresponds to $E_{\min} = E_{\max}$, one gets:

$$H_n = \frac{2K_1}{\mu_0 M_s} \qquad \textbf{(2. 6)}$$

which is the anisotropy field.

Full reversal follows nucleation. Thus, for coherent rotation, the coercive field, identical to the nucleation field, is equal to the anisotropy field. It considers that going from one easy direction to the other, the magnetization changes just the direction, not its magnitude and it is obliged to pass through the hard axis magnetization, thus it has to pay the anisotropy field in order to arrive in the next position. Schematically, this process can be seen in **Fig. 2. 3**. Position (1) and (3) correspond to the two minima while (2) is the hard axis magnetization.

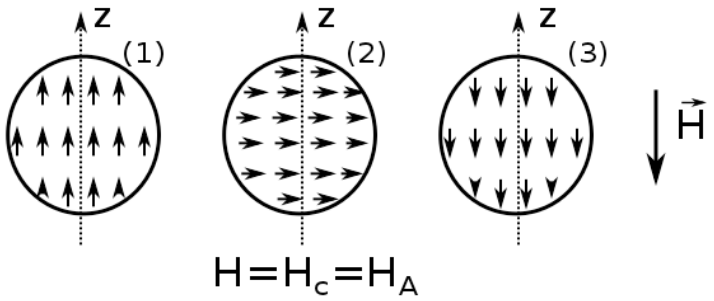

Fig. 2. 3 Schematic representing coherent rotation in uni-axial systems.

All that was mentioned about coherent rotation is valid for the case where the field is applied along the easy direction. Interesting information can be extracted if the field is applied along other directions. This topic will be discussed in one of the next sections, where the angular dependence of coercivity for different types of reversal will be presented.

Magnetization curling

Another nucleation type of magnetization reversal is the one called magnetization curling. Contrary to the SW model, the magnetization does not remain homogeneous during rotation. Flux closure occurs to reduce the magnetostatic energy. While in the case of coherent rotation the exchange energy was totally ignored, in this case, the exchange energy has to be paid but it is compensated by the gain in magnetostatic energy.

Fig. 2. 4 represents schematically the curling reversal in a cylinder. The nucleation field was calculated in the case of an ellipsoid of revolution[5,6]:

$$H_N = \frac{2K_1}{\mu_0 M_s} - NM_s + \frac{cA}{\mu_0 M_s R^2} \qquad \textbf{(2. 7)}$$

The three terms involved are: magneto-crystalline anisotropy, self-magnetostatic energy and exchange energy. A is the exchange constant, R the radius of the ellipsoid and c a constant that depends on the demagnetizing factor N, of value 8.666 for spheres and 6.678 for long cylinders.

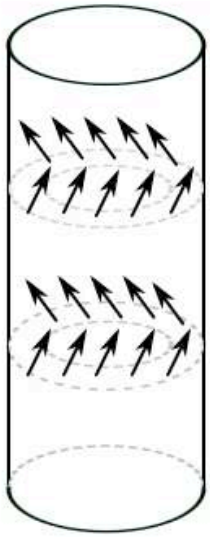

Fig. 2. 4 Schematic of magnetic curling in a cylinder.

II.2.2 Nucleation versus Pinning

For very high anisotropy systems, the difference in calculated coercive field values for coherent rotation and curling are minor. Nevertheless, the coercivity values measured experimentally are always smaller than the values given by both the coherent rotation model and the curling model. This is the so-called Brown paradox and can be explained by the fact that the microstructure has a strong influence on coercivity. In reality, the presence of areas with lower anisotropy decreases a lot the value of the coercive field. Nucleation starts at the lower anisotropy regions and it will then propagate into the entire structure that is in contact with that zone. So, a small defect can induce the reversal of an important part of the system. After it nucleates, reversal may propagate in the entire system, for the same field. In this case, reversal is controlled by nucleation. Alternatively, the nucleus formed may remain pinned at magnetic heterogeneities, in which case reversal is said to be pinning controlled.

In this context, nucleation consists in the formation, under a certain applied field, of small nuclei (domains) with reversed magnetization separated, via domain walls or domain wall like moment configurations, from the rest of the material, which is still in its saturated state. After nucleation, the formed nucleus may: i) disintegrate spontaneously (if the energy is not enough to maintain it); ii) remain pinned or iii) grow into the rest of the magnetic body. In this latter case, the propagation of magnetization reversal through the entire system proceeds for the same field value as nucleation occurs. This corresponds to the case of nucleation type materials, which are essentially homogeneous in the bulk. The domain wall energy does not depend on its position and the nucleus of reversed magnetization formed initially, grows to encompass the entire material, thus minimizing Zeeman energy.

Conversely, it may happen that the growth of reversed domains is impeded by some inhomogeneities in the material. In this case, the domain wall may be trapped at some low energy defect region and an increased value of the applied field is needed in order to be able to move further the domain wall. This is the case of domain wall pinning. It is obvious that the pinning mechanism implies the existence of reversed magnetic domains (related to the saturated state) so we could say that there are no purely pinning type materials since we need to produce, one way or another, some reversed regions.

So, we have a system decomposed into domains, with alternating magnetization orientations, separated by magnetic domain walls. A domain wall can be imagined as a membrane that can be moved using the Zeeman energy due to the applied field. Its energy, for uniaxial systems considered here, is $\gamma = 4\sqrt{AK_1}$. This membrane can move freely until it encounters some pinning defects with, for instance, K_1 smaller than the value of the base material. At that point, the wall is stuck, the position being energetically favorable. In order to move the wall further, the applied field must be increased. The concept of domain wall pinning is shown schematically in **Fig. 2. 5**. for a very simple case. After saturation, (1), the direction of the applied field is reversed. The nucleation

starts at (2), the domain wall is formed, it starts to move but at (3) it encounters some defect points and is trapped there. A bigger value of the field unblocks the wall and in (4) saturation in the opposite direction is achieved.

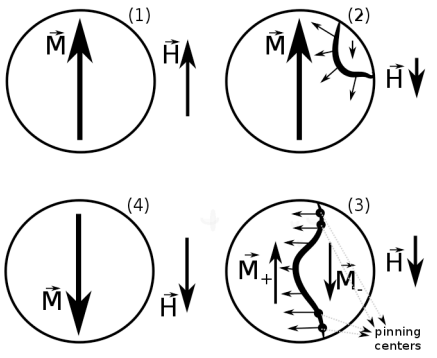

Fig. 2. 5 Depiction of magnetization reversal in the case of nucleation-pinning reversal mechanism.

There are different pinning modes depending on the domain wall characteristics (energy, width, magnetic properties), pinning site characteristics (dimensionality: point or planar, magnetic nature) and the way they interact with each other.

Friedberg and Paul[7] and Hilzinger and Kronmüller[8] calculated the pinning field defined as the maximum applied field for which there exists a static domain wall solution in the case of a magnetic planar defect (grain boundary) and a 180° domain wall:

$$H_p = 3^{-3/2}\frac{K_1}{M_s}\frac{d_w}{\delta_w}\left(\frac{A_1}{A_1'} - \frac{K_1'}{K1}\right) \qquad \textbf{(2. 8)}$$

Here, K_1, M_s, A_1, are the anisotropy constant, spontaneous magnetization, exchange constant characterizing the material outside the domain wall and A1′, K1′ are the exchange constant and anisotropy constant related to the defect. d_w and δ_w represent the widths of the defect and of the domain wall, respectively.

Kronmuller et al.[9] calculated the field for point defects:

$$H_c = \frac{1}{M_s}\left(\frac{K_1}{\delta_w^{1/2}} + \frac{A}{\delta_w^{5/2}}\right)\rho^{1/2} \qquad \textbf{(2. 9)}$$

with ρ the defect density and all the other parameters characterizing the main phase.

As a general rule, the pinning is believed to be more effective for defects comparable in size with the domain wall width and for domain walls where K_1 varies drastically with the position.

In conclusion, defects can have both a positive and a negative effect on the value of the coercivity. When they serve as nucleation points, they represent weak points of a magnet while, when playing the role of pinning sites, they can retard the reversal to higher applied fields, thus increasing the resistance to demagnetization.

In some cases, the defect region source of domain wall pinning may be associated to the same defect that is the source of nucleation. Then, the volume of magnetization reversed at nucleation is extremely small, not detectable by magnetization measurements. It is not possible to separate experimentally such pinning-controlled coercivity from true nucleation. In this case, Givord and Rossignol[10] proposed to use the expression “passage” rather than “pinning”.

II.3 Methods to characterize coercivity

In the previous paragraphs, different types of magnetization reversal were presented. Considering the experimental results in the case of uniaxial high anisotropy systems, we can say that the mechanism of coercivity is a complex one that implies more than one, possibly all of the above mentioned events: nucleation at lower anisotropy defect points, formation of domain walls, propagation of these domain walls into the main phase, pinning – depinning in the case of inhomogeneous materials. Each of these events takes place for a certain value of the external applied field, the highest of them being the coercive field. Understanding why a certain process happens for that certain field and relating it to the microstructure is an important and difficult problem in permanent magnet research. Knowing how the microstructure should be optimized and doing so, one can exploit better the intrinsic properties of the given material.

Why is this problem difficult? Because it is impossible to probe directly the microstructure-reversal link, the critical lengths implied being too small to be accessible to experiment. That's why indirect measurements are used to study this problem. The most important ones, that will be discussed further, are:

a) Temperature and time dependence of coercivity;
b) Angular dependence of coercivity;
c) Minor loop analysis.

II.3.1 Temperature and time dependence of coercivity

Hysteresis loops measured at different temperatures on NdFeB-based magnetic materials show a continuous decrease of coercivity with increasing temperature. The rate of the decrease may vary from one material to another as shown for ex. in [11,12].

Starting from $H_c(T)$ measurements, different models are being used to analyze the magnetization reversal type.

The most used approach to analyze $H_c(T)$ is the so-called micromagnetic model (MM). In the framework of this model, the coercive field was found to have the form:

$$H_c = \alpha \frac{2K_1}{\mu_0 M_s} - N_{eff} M_s \qquad \textbf{(2. 10)}$$

Expression (2. 10) was initially introduced on purely phenomenological grounds[13,14]. Kronmüller and co-workers[15] showed that the above mentioned equation may be derived from linearization of the classical micro-magnetic equations in the case of inhomogeneous systems, characterized by a strong magneto-crystalline anisotropy with local deviations of the anisotropy constant. Nucleation reversal starts at points where anisotropy is a fraction of the anisotropy of the bulk. The parameter α in eq. (2. 10) indicates how much the anisotropy is lowered in the nucleation starting points.

In [16], $H_c(T)$ is treated considering three regions of temperature. The regions are chosen knowing that in the $Nd_2Fe_{14}B$ system, there is a spin reorientation at around 135 K and the anisotropy changes from uni-axial to cone like.

a) 135 K < T < 460 K

$$H_c = \alpha_K \alpha_\psi^{\min} \frac{2K_1}{M_s} - N_{eff} M_s \qquad \textbf{(2. 11)}$$

α_K is a structure related parameter that was calculated in the case of a $2r_0$ width planar inhomogeneity with no anisotropy, as being:

$$\alpha_K = 1 - \frac{1}{4\pi^2} \frac{\delta_w^2}{r_0^2} \left(-1 + \sqrt{1 + \frac{4K_1 r_0^2}{A}}\right)^2 \qquad \textbf{(2. 12)}$$

If $2\pi r_0 \geq \delta_w$ and the defect has no anisotropy, then (2. 12) becomes:

$$\alpha_K = \frac{\delta_w}{\pi r_0} \qquad \textbf{(2. 13)}$$

$\alpha_\psi^{\min}$ corresponds to $\psi \cong \frac{\pi}{4}$ and it is derived from:

$$\alpha_\psi = \frac{1}{\cos\psi} \frac{1}{(1 + tg^{2/3}\psi)^{3/2}} \left(1 + \frac{2K_2}{K_1} \frac{tg^{2/3}\psi}{1 + tg^{2/3}\psi}\right) \qquad \textbf{(2. 14)}$$

It takes into consideration the grain misalignment, ψ being the angle between the c-axis of the grain and the applied field.

Equation (2. 11) can be re-written as:

$$\frac{H_c}{M_s} = \alpha_K \alpha_\psi^{\min} \frac{2K_1}{M_s} \frac{1}{M_s} - N_{eff} \qquad \textbf{(2. 15)}$$

The plot $\frac{H_c}{M_s}$ vs. $\alpha_K \alpha_\psi^{\min} \frac{2K_1}{M_s}$ will have a linear behavior and the values for α_K and N_{eff} can be extracted. Knowing α_K, r_0 results naturally from (2. 13).

b) T < 135 K

The relative influence of K_1 and K_2 changes significantly with temperature for $Nd_2Fe_{14}B$ as **Fig. 2. 6** shows. Already at 200 K, the two constants become very close in value and, in the range of temperatures considered here, K_2 plays an important role.

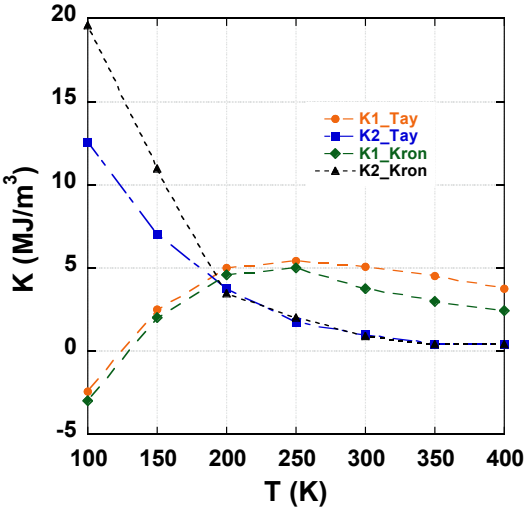

Fig. 2. 6 Temperature dependence of $Nd_2Fe_{14}B$ anisotropy constants (K_1 and K_2) taken from two different sources[17,18].

The coercive field is then:

$$H_c = \alpha' \frac{4}{3\,6^{1/2} M_s} \left(\frac{K_1 + 2K_2 + K_d}{K_2}\right)^{3/2} \quad \textbf{(2. 16)}$$

where $K_d = \frac{1}{2} M_s^2 (N_\perp - N_\parallel)$ [15] and α' encompasses the effect of grain surfaces. This last parameter can be extracted, like in the previous case, by plotting the right graph.

c) T > 460K

At these high temperatures, K_1 and K_2 have very low values and the coercivity is mainly due to domain wall pinning. For planar defects:

$$H_c = \frac{2\delta_w}{3\pi r_0} \frac{2K_1}{M_s} - NM_s \quad \textbf{(2. 17)}$$

The plot $\frac{H_c}{M_s}$ vs. $\frac{2K_1}{M_s^2}$ provides the values for N and r_0.

Briefly resumed, in many publications, the coercive field is simply expressed as in (2. 10). N_{eff} and α are considered as temperature independent parameters even if, strictly speaking, they are not. Values of α > 0.3 are taken as proof that reversal occurs by nucleation[11], since the micromagnetic model as developed, predicts that in this case, the nucleation field is larger than the propagation field.

A second model, called the Global Model (GM) was proposed by Givord et al.[19, 20]. It does not relate the coercivity directly to the anisotropy of the main phase. The concept of activation volume is introduced and the coercivity is related to this parameter that can be accessed experimentally.

The GM states that reversal is initiated in a critical volume, v_n, with the formation of a heterogeneous magnetic configuration, reminiscent of a domain wall, of energy γ_n, under a critical field:

$$H_{crit} = \alpha' \frac{\gamma_n}{v_n^{1/3} \mu_0 M_s} \quad \textbf{(2. 18)}$$

α' being a phenomenological parameter and M_s the spontaneous magnetization of the main phase.

Thermal activation is also considered, at finite temperatures. In this case:

$$v_n = v_a = \frac{k_B T}{S_v M_s} \quad \textbf{(2. 19)}$$

S_v is the viscosity coefficient, experimentally accessible from magnetic after-effect measurements. This will be discussed further at the end of this chapter. Further assumptions:

v_n (critical volume), assumed to be proportional to δ_n^3 (domain wall width in critical volume) is the critical volume in which reversal is initiated, assumed to be equal to the experimentally derived activation volume v_a;

γ_n (wall energy in critical volume) assumed proportional to γ (wall energy main phase);

A_n (exchange constant in critical volume) assumed to be proportional to A (exchange constant of the main phase).
The coercive field is expressed as:

$$H_c = \alpha \frac{\gamma}{v_a^{1/3} \mu_0 M_s} - N M_s - 25 S_v \quad \textbf{(2. 20)}$$

Using the notation $H_0 = H_c + 25 S_v$, equation (2. 20) becomes:

$$H_0 = \alpha \frac{\gamma}{v_a^{1/3} \mu_0 M_s} - N M_s \quad \textbf{(2. 21)}$$

or $$\frac{H_0}{M_s} = \alpha \frac{\gamma}{v_a^{1/3} \mu_0 M_s^2} - N \quad \textbf{(2. 22)}$$

The two parameters: α and N can be extracted by plotting $\frac{H_0}{M_s}$ vs. $\frac{\gamma}{v_a^{1/3} \mu_0 M_s^2}$.

To conclude this section, it can be noted that both the MM (2. 10) and GM models (2. 20) assume simple proportionality between an intrinsic property of the main phase (K or γ) and the same property in the defect region.

An interesting aspect of the global model emerges in the case where the anisotropy may be expressed in terms of 2nd order anisotropy only:

$$v_a \sim \delta_n^3 \approx (\frac{A_n}{K_n})^{3/2} \Rightarrow K_n \sim \frac{A_n}{v_a^{2/3}}$$

$$\gamma_n \sim \sqrt{A_n K_n} \sim \frac{A_n}{v_a^{1/3}}$$

Eq. (2. 18) becomes:

$$H_{crit} \sim \alpha' \frac{A_n}{v_a^{2/3} M_s} = \alpha \frac{A}{v_a^{2/3} M_s} \quad \textbf{(2. 23)}$$

In expression (2. 23), the contribution of anisotropy is implicitly included in the activation volume, an experimental quantity. An expression for the temperature dependence of the coercive field is obtained which does not rely on the hypothesis that the anisotropy (or the domain wall energy) in the defect region is proportional to the main phase anisotropy. This relation can not be used in the case of NdFeB magnets where higher order anisotropy constants must be considered, in particular at low temperature.

Magnetic viscosity

Magnetic viscosity measurements give access to the activation volume, a parameter used into the global model just described. When the system is in a metastable state and this state is separated from lower energy states by energy barriers of the same order of magnitude as the thermal energy, thermal activation will contribute to magnetization reversal. The energy landscape is fixed and a certain characteristic time τ is needed for the progressive rearrangement of the magnetic structure to be produced and states with lower energy to be reached. This time is given by the Arrhenius law:

$$\tau = \tau_0 e^{\frac{E_a}{k_B T}} \quad \textbf{(2. 24)}$$

τ_0 is a constant of the order of 10^{-10} seconds and E_a is the characteristic height of the barriers that will be surpassed after time τ. The bigger the ratio between E_a and the thermal energy, the longer the time spent in front of these barriers.

A way to bring the system into a metastable state and reveal thermal activation effects consists in placing the system in an applied field not too far from the coercive field. During a certain measurement time t, the magnetization changes progressively and it is this phenomenon that is called magnetic viscosity, **Fig. 2. 7**b.

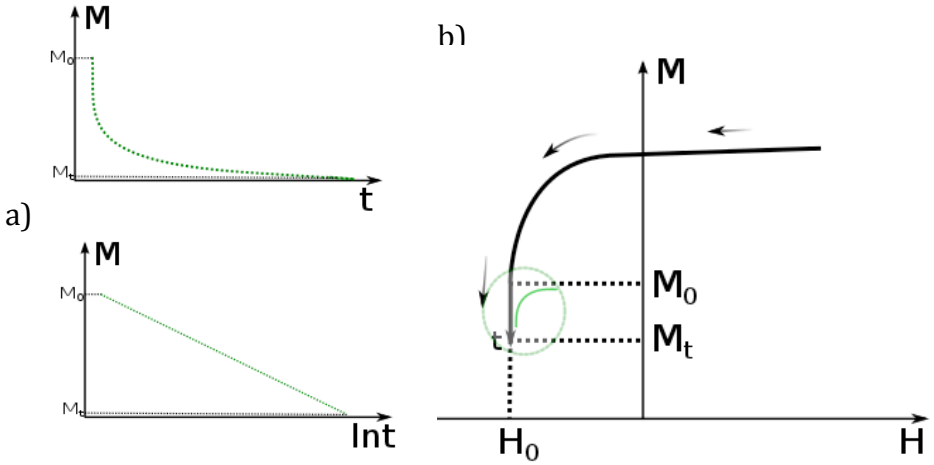

Fig. 2. 7 Evolution of magnetization with t and lnt schematic (a) for an applied field close to coercivity, as shown in (b).

It is often observed experimentally[17,21,22] that the magnetization changes linearly with the natural logarithm of time, as the scheme in **Fig. 2. 7**a shows, the slope of the magnetic variation being called the magnetic viscosity, S. Mathematically this can be expressed as:

$$M_t = M_0 - S \ln t \quad \textbf{(2. 25)}$$

It can be shown that relation (2. 25) applies in the case where the energy barrier distribution function is broad. Then, the moments that reverse at time t can be taken as those for which the energy barrier is given by (2. 24), replacing τ by t.

Under these conditions, relation (2. 24) gives access to the parameter that is used in the definition of activation volume, namely the magnetic viscosity coefficient, S_v:

$$S_v = \frac{S}{X_{irr}} \quad \textbf{(2. 26)}$$

This takes into consideration only irreversible changes of the magnetization with the applied field through the irreversible magnetic susceptibility ($X_{irr} = X_{tot} - X_{rev}$). X_{rev} characterizes that part of the magnetic moments that rotate towards the field but once the field would be brought to zero, they would go back to their initial position because their minimum energy state will still be along the direction of saturation.

II.3.2 Angular dependence of coercivity

Measuring the hysteresis loops (and thus coercivity) with the field applied at different angles from the easy axis is a powerful tool that can be used to approach the type of mechanism governing reversal in a certain material. One of the most common experiments consists in saturating the sample along the easy direction and applying the field at an angle with the easy direction, as it is shown in **Fig. 2. 8**.

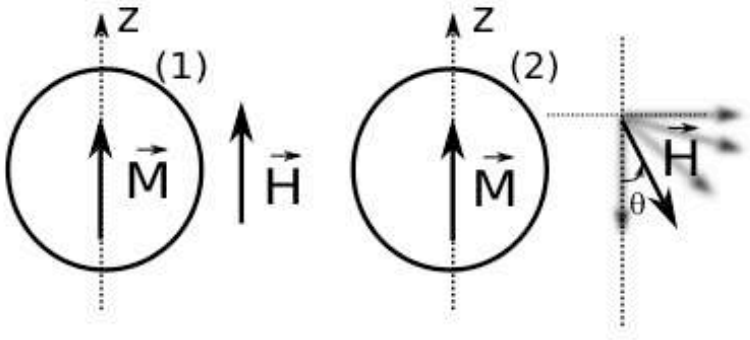

Fig. 2. 8 Angle definition used in angular dependence of coercivity experiments.

The variation of the coercive field (H_c) as a function of the applied fields' angle ($0 \le \theta \le \pi/2$) can, in theory, say if reversal is mainly nucleation or pinning.

In the case of Stoner - Wohlfarth systems, the angular dependence of coercivity is [4]:

$$\frac{H_c(\theta)}{H_c(0)} = \frac{1}{(\sin^{2/3}\theta + \cos^{2/3}\theta)^{3/2}} \qquad \textbf{(2. 27)}$$

In the case of pinning materials (or passage) in which reversal is mainly due to magnetic domain wall movement through the material, the theory predicts:

$$\frac{H_c(\theta)}{H_c(0)} = \frac{1}{\cos\theta} \qquad \textbf{(2. 28)}$$

It is known also as the Kondorski law and it is a particular case ($N_z = 0$) of the (more general equation) [23]:

$$\frac{H_c(\theta)}{H_c(0)} = \frac{(N_A + N_x)\cos\theta}{N_z \sin^2\theta + (N_A + N_x)\cos^2\theta} \qquad \textbf{(2. 29)}$$

N_x, N_z - demagnetizing coefficients and $N_A = H_A / M_s$.

For comparison, (2. 27) and (2. 28) are plotted in **Fig. 2. 9**. The coercivity decreases from $H_c = H_A$ at $\theta = 0°$ to $H_c = \frac{H_A}{2}$ at $\theta = 45°$ and increases again up to $H_c = H_A$ for $\theta = 90°$ for Stoner - Wohlfarth systems.

In the second case, the coercivity increases constantly with the angle, with almost insignificant change for $\theta \le 45°$ and $H_c \to \infty$ at $\theta = 90°$. At large angles, the coercive field for pinning diverges.

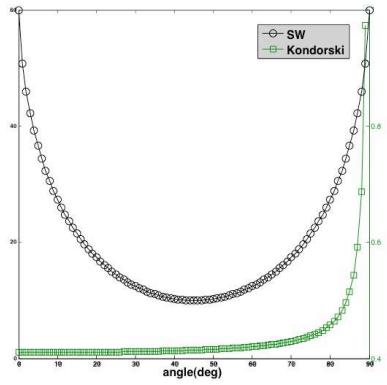

Fig. 2. 9 SW compared to Kondorski law for describing the angular dependence of coercivity.

Both types of curves presented in **Fig. 2. 9** characterize ideal systems with strong uniaxial magneto-crystalline anisotropy. Experimentally, for NdFeB-based materials, a "smoothened" $\frac{1}{\cos\theta}$ behavior, due to the distribution of grain orientation around the average magnetization direction, is typically reported[24,25].

[1] G. Bertotti, *Hysteresis in Magnetism. For physicists, materials scientists and engineers,* Academic Press, 558p (1998);

[2] R. Skomski and J.M.D Coey, *Permanent magnetism*, Taylor & Francis, 420p (1999);

[3] P. Bruno, Physical origins and theoretical models of magnetic anisotropy, "Magnetismus von Festkörpern und grenzflächen", edited by P.H. Dederichs, P. Grünberg and W. Zinn, 24. IFF-Ferienkurs, 24.1-24.8, Forschungszentrum Jülich (1993);

[4] E.C.Stoner and E.P. Wohlfarth, Phil. Trans. of the Roy. Soc. Lond. Series A, math. And Phys. Sc. 240, 599 (1948);

[5] Y. Ishii, J. Appl. Phys. 70, 3765 (1991);

[6] A. Aharoni, Introduction to the Theory of ferromagnetism, Oxford University Press, Oxford, 319p (1996);

[7] R. Friedberg and D. I. Paul, Phys. Rev. Lett. 34, 1234 (1975);

[8] H.R. Hilzinger and H. Kronmüller, Phys. Lett., 51A, 59 (1975);

[9] H. Kronmüller et al., Int. J. Magn. 5, 27 (1973);

[10] D. Givord, M. Rossignol and V.M.T.S. Barthem, JMMM 258, 1 (2003);

[11] H. Kronmüller and K.D. Durst, JMMM 74, 291 (1988);

[12] A. Fukuno, K. Hirose and T. Yoneyama, J. Appl. Phys. 67, 4750 (1990);

[13] F. Kools, J. Phys. C6, 349 (1985);

[14] S. Hirosawa, K. Tokuhara, Y. Matsuura, H. Yamamoto, S. Fujimura and M. Sagawa, JMMM 61, 363 (1986);

[15] H. Kronmuller, K. D. Durst and G. Martinek, JMMM 69, 149 (1987);

[16] J. Hu, X.C. Kou and H. Kronmüller, Phys. Stat. Sol. (a) 138, K41 (1993);

[17] D.W. Taylor, thesis Lab. Magn. L. Neel, Grenoble (1992);

[18] K.D. Durst and H. Kronmüller, JMMM 59, 86 (1986);

[19] D. Givord, P. Tenaud and T. Viadieu, IEEE Trans. Magn. 24, 1921 (1988);

[20] V.T.M.S Barthem, D. Givord, M. F. Rossignol and P. Tenaud, Physica B 319, 127 (2002);

[21] R. Street and J. C. Woolley, Proc. Phys. Soc. 62, 562 (1949);

[22] Q. Yao, R. Grössinger, W. Liu, W.B. Cui, F. Yang, X.G. Zhao and Z. D. Zhang, JMMM 324, 2854 (2012);

[23] R.M. Grechishkin, S. S. Soshin and S. E. Ilyashenko, 1st Int. Workshop on Simulation of Magnetization Processes, SMP95_72 (1995);

[24] D. Elbaz, D. Givord, S. Hirosawa, F. P. Missell, M. F. Rossignol and V. Villas-Boas, J. Appl. Phys. 69, 5492 (1991);

[25] F. Cebollada, M. F. Rossignol and D. Givord, Phys. Rev. B 52, 13511 (1995).

III. Sample preparation and characterization techniques

Preparation

During this thesis, two types of samples were analyzed:

• Sintered bulk NdFeB - based samples provided by the Toyota Motor Corporation (TMC). The starting alloy is subjected to a melt spinning process. The resulting ribbons are sintered under pressure (200 MPa) at 650 °C for 3 min. The sintered piece is hot forged at 750 °C and the result is what is hereafter called "base material". Further, the base material may undergo a NdCu infiltration treatment. A piece of NdCu is placed on top of the magnet and the entire system is annealed at 600 °C for 165 min. During the heat treatment, NdCu becomes liquid (see phase diagram Annex 8) and penetrates into grain boundaries. As a result, the grains are better decoupled magnetically. The infiltration process is schematized in **Fig. 3. 1**.

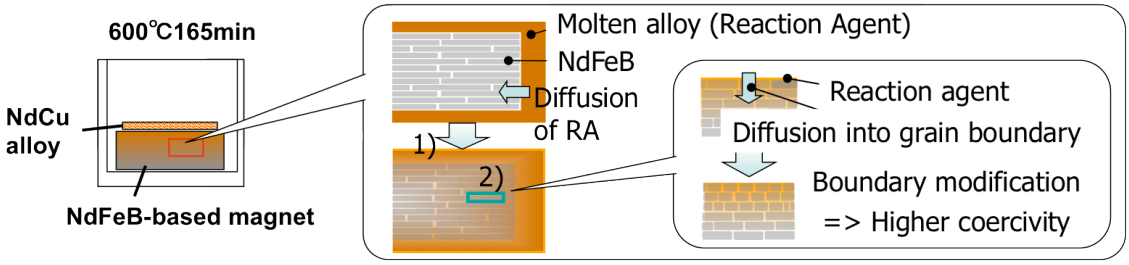

Fig. 3. 1 Schematics of the infiltration process (performed on the bulk TMC samples) and its results (T. Shoji, TMC).

• Thick NdFeB - based (or SmCo) films – deposited by triode sputtering. This technique is described next.

III.1 Triode Sputtering

The bombardment of a material with energetic particles can give rise to its pulverization if the kinetic energy of the particles is greater than the binding energy characteristic of that material. This process, observed in the beginning as a limiting factor for the lifetime of discharge tubes, was afterwards transformed into a useful technique either for deposition of thin films or etching/cleaning of surfaces. There are different types of sputtering techniques, the one we used is triode sputtering, presented schematically in **Fig. 3. 2**. Electrons are provided, through thermionic emission, from a tungsten filament, in a vacuum chamber. They are accelerated towards a positively polarized electrode (anode). On their way, they ionize Ar atoms present in the chamber, giving rise to plasma. The positive ions, Ar^+, are then accelerated towards the negatively polarized target and can induce different effects: emission of secondary electrons, reflection of the ions, implantation of Ar^+ in the target, pulverization of the surface of the target. The last one is the important one for deposition and it occurs if the energy of the ions is sufficiently high. The pulverized material will then deposit everywhere in

the chamber, including on the substrate that is positioned in front of the target. A magnetic field is used to confine the plasma and to increase the ionization rate by "spiraling" the path of the electrons towards the anode.

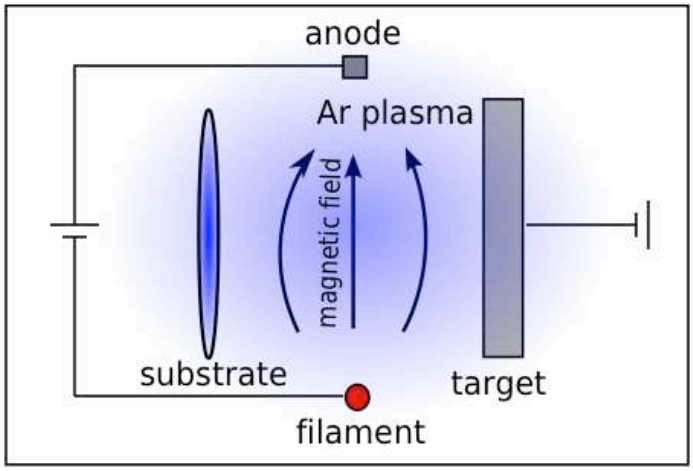

Fig. 3. 2 High deposition rate triode sputtering scheme.

Sputtering system:

Base pressure: 10^{-6} mbar;
Sputtering pressure: 10^{-3} mbar;
Substrate – target distance: 4 - 10 cm (typically 7.5 cm);
Filament current ≤ 180 A;
Anode voltage/current: 80 V/8 A;
Targets:
- 4-target holder;
- target size ≤ 10 cm^2;
- target voltage ≤ 900 V;

Substrate holder:
- stationary or rotating *;
- substrate size ≤ 10 cm diameter;
- heating ≤ 800 °C;
- bias voltage ≤ 200 V †.

The main advantage of this sputtering system is the high deposition rate that can go up to 20 μm/h, depending on the target material, size, voltage, target-substrate distance.

Permanent magnets with very good magnetic properties, like NdFeB[1], SmCo[2] and FePt[3] were prepared using this triode sputtering machine.

After deposition, the films may be crystallized via a thermal treatment that can be done either in-situ or ex-situ. For ex-situ annealing, a homemade Mo resistance furnace was used in most of the cases. It could reach a maximum

* Rotation improves homogeneity in thickness, composition and magnetic properties across the substrate;

† Films may be etched.

temperature of 1200 °C and a maximum ramp rate of around 10 °C/s for samples ≤ 4 cm in diameter. Recently, a Rapid Thermal Annealing (RTA) furnace was acquired. Substrates of maximum size 10 cm can be annealed, for temperatures up to 1300 °C and ramp rates between 1 °C/s and 300 °C/s.

Characterization

III.2 Vibrating Sample Magnetometer (VSM)

Magnetic measurements were performed using either VSM or VSM SQUID magnetometers.

Faraday's law of induction states that when the magnetic environment of a coil is changed, there will be a voltage induced in that coil ($V \propto -\frac{\Delta\Phi}{\Delta t}$). Many magnetometers work using this principle. A net magnetic moment is induced in the sample to be measured by placing it in the magnetic field produced by a super-conducting coil. The sample is placed in the center of the detection coils, coils that will measure the voltage induced as a result of the vibration of the sample in the magnetic field. The measured voltage is proportional to the magnetization of the sample ($V \propto -\frac{\Delta\Phi}{\Delta t} \Rightarrow \int V(t)\,dt \propto -\int \frac{\Delta\Phi}{\Delta t} dt \propto \int \Delta B \propto \int \Delta H + \int \Delta M \propto \int \Delta M$). In this expression, $\int \Delta H = 0$ due to the anti-parallel winding of the detection coils.

In a VSM, the magnetic moment of the sample is extracted directly from the voltage induced in the detection coils. In the case of a VSM-SQUID, the detection coils are connected to a SQUID element that works like a very sensitive current-to-voltage converter and allows measuring (indirectly) very weak magnetic fields. The scheme of a VSM-SQUID is shown in **Fig. 3. 3**. If the SQUID element is ignored, the scheme corresponds to a VSM.

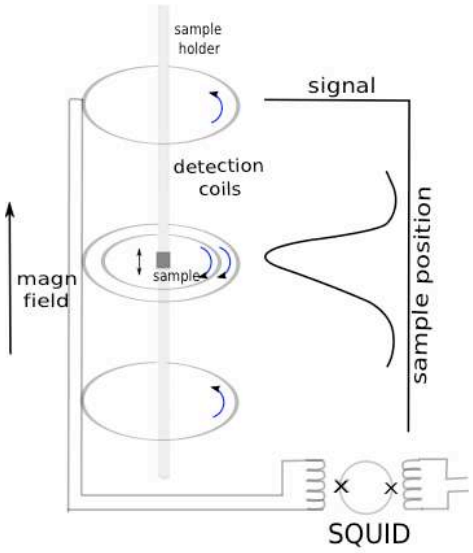

Fig. 3. 3 Schematics of a VSM-SQUID magnetometer. The blue arrows indicate the clockwise-anticlockwise configuration of the detection coils that cancel the effect of the applied field.

The machines used for this work are an Oxford VSM and Quantum Design VSM SQUID.

Characteristic features are given in **Table 3. 1**:

	VSM	**VSM-SQUID**
Maximum field	8 T	7 T
Sensitivity	10^{-8} Am^2	10^{-11} Am^2
Temperature Range	RT	1.8 K - 400 K
Max. magnetic moment	10^{-3} Am^2	10^{-2} Am^2

Table 3. 1 Main parameters of the VSM and VSM-SQUID instruments used for magnetic measurements.

To perform angular-dependent measurements, special sample holders were developed for each instrument.

III.3 Scanning Electron Microscopy (SEM)

In the scanning electron microscopy technique, images are formed by the collection and amplification of the electrons backscattered or emitted from the surface of a sample when this sample is scanned with a high-energy electron beam. The two important aspects that differentiate the electron microscope from an optical one are the resolution and the high depth of field.

This technique exploits the effects produced by electrons when they interact with matter. The interaction of electrons with solids being complex, there are different types of information that can be extracted, the ones mostly used in SEM analysis are shown in **Table 3. 2**.

Operational Mode	Electrons detected	Information
Emissive	Secondary electrons	Topography
Reflective	Backscattered electrons	Topography Atomic number sensitivity
X-Ray	Photons in X-ray band	Quantitative chemical analysis (EDX)

Table 3. 2 Effects of the interaction of electrons with matter.

The investigation of chemical composition can be either qualitative or quantitative. The qualitative information consists of the contrast given by the different atomic numbers of the elements, the so-called atomic number contrast. For the quantitative study, Energy dispersive X-ray analysis (EDX) is used. When the electron beam strikes the sample, X-rays may be emitted. Due to the fact that each element emits X-rays differently, this technique can be used to identify and quantify the chemical composition of the sample.

The resolution of the microscope depends on different factors, one of the important ones being the spot size of the primary electron beam, which in turn depends on the type of electron gun. In this case, a field emission gun (FEG) was used. It permits a higher resolution (10 nm) compared to other types of guns, like for ex. a thermionic emission gun.

For imaging, low voltage (3 keV) and small working distances (3 mm) were used (in - lens detector) while for quantitative chemical analysis, higher voltages (15 keV) and larger working distances (8 mm) were used.

III.4 X-Ray Diffraction (XRD)

X-rays are electromagnetic radiation with short wavelength. For diffraction studies, used to reveal the structure of crystals, wavelengths in the range of 0.5-2.5 Å are used.

Diffraction is essentially a scattering phenomenon in which a large number of atoms cooperate. The atoms of a crystal are arranged periodically on a lattice. They scatter incident X-rays in all directions. In some of these directions, the scattered beams are in phase and constructive interference takes place. The angle of diffraction, for a given wavelength, can be obtained from Bragg's law, see **Fig. 3. 4**.

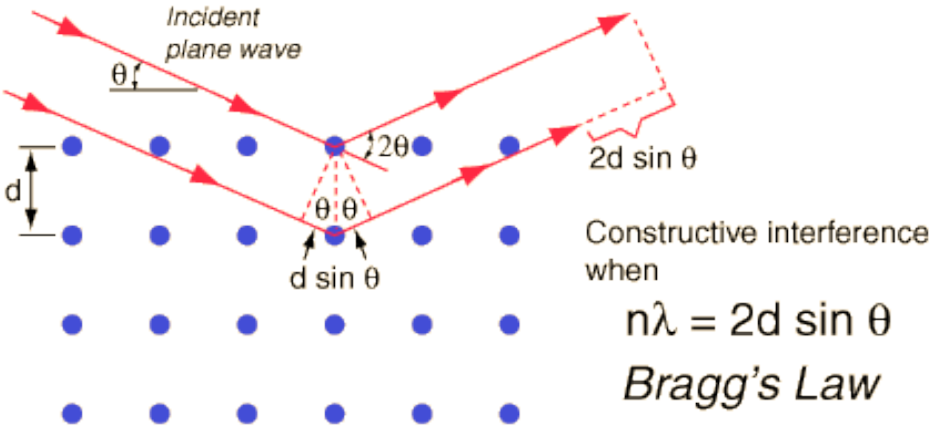

Fig. 3. 4 Schematic showing the geometry of X-ray diffraction technique[4];

In the equation from **Fig. 3. 4**, n is the order of reflection, λ is the wavelength of the X-ray beam, d is the distance between the planes of atoms and θ is the incident angle.

The angle at which a beam of a given wavelength is diffracted by a given set of lattice planes is determined by the crystal system to which the crystal belongs and to its lattice parameters. It means that from the angles of diffracted beams one can extract information about the crystal structure and the size of the unit cell.

The most common use of X-ray diffraction is structure analysis of a given sample by measuring angles and intensities of Bragg reflections.

Texture analysis, that indicates if there is a preferred orientation of the crystallites, can also be done. This preferred orientation is described in terms of pole figures that represent the difference in diffracted intensity as a function of directions of the sample. During a measurement, a specific value of the Bragg angle is chosen (2θ). By varying the tilt angle from sample surface normal direction and the rotation angle of the sample around its surface normal and collecting the intensity of the diffracted beam for each direction, one gets a pole figure.

In this work, both crystalline structure analysis and texture determination were performed using a Co X-ray source, with λ=1.78897 Å.

III.5 Magnetic Force Microscopy (MFM)

Atomic force microscopy (AFM) is another type of microscope that provides high resolution, typically 10 nm, in ambient conditions. It is the atomic equivalent of Braille reading (**Fig. 3. 5**) and it was developed in 1986[5] as a particular case of the Scanning Tunneling Microscopy (STM) concept[6].

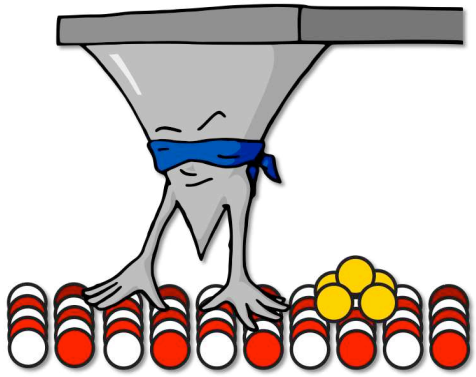

Fig. 3. 5 "AFM man Braille reader", from www

The surface of the sample is "read" with the aid of a sharp silicon tip by monitoring the interaction force between the tip and the sample. Depending on the nature of the force, different information about the sample can be obtained: topographical - AFM, electrical - EFM, magnetic – MFM etc.

The two main functioning modes of AFM are the contact mode (tip always in contact with the sample) and tapping mode (tip vibrating close to the sample) decreasing the contact time. We used this 2nd technique to obtain magnetic information in the lift-mode MFM, a two-step technique that allows separation of the magnetic and topographic information. In a first step, the topography is registered by scanning the sample in the tapping AFM mode, very close to the surface. A second scan, at a sufficiently high distance from the sample to minimise the Van der Waals interaction, will follow the topography registered in step I. Here, the long-range forces are the source of the signal. We suppose, in our samples, that these forces are purely magnetic.

How can we measure the interaction force between the sample and the sharp tip? Most microscopes use the laser deflection technique. The tip is attached to a silicon cantilever. A laser beam is sent to the back of this cantilever and its reflection is captured by a 4-segment diode, the detector in **Fig. 3. 6**. The deflection detected by the diode is proportional to the force. By treating the output of the diode, a 2D image of any surface is obtained.

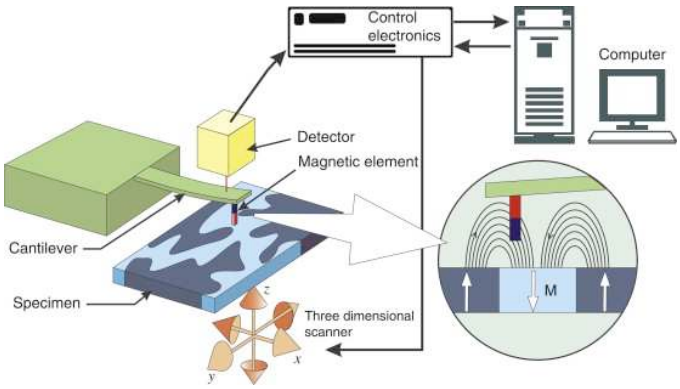

Fig. 3. 6 Schematic of a typical Magnetic Force Microscope (MFM)[7].

In the tapping mode, the cantilever vibrates at its resonant frequency. The oscillation is thus described by the resonance frequency, resonance amplitude and the phase, **Fig. 3. 7**. When there is some interaction force, these parameters change. One way of recording the image is to keep the amplitude fixed with the aid of a feedback loop and register the change in the phase. The phase shift is proportional to the force gradient, whatever the source of the force. As it can be seen in **Fig. 3. 7**, an attractive force will lower the resonance frequency and a repulsive one will increase it. The phase will change accordingly. This is called phase imaging semi-contact mode.

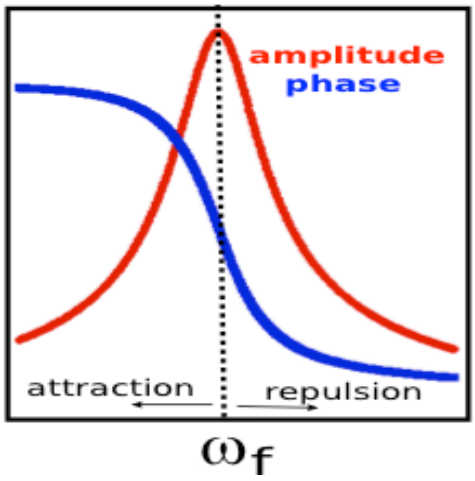

Fig. 3. 7 AFM probe's resonance frequency shift under attractive/repulsive forces

Information about the types of probes that were used is given in Chapter V and the theory of the modelisation of the probe and probe-sample interaction is presented in Annex 1 and Annex 2.

[1] N. M. Dempsey, A. Walther, F. May and D. Givord, Appl. Phys.Lett. 90, 092509(2007);

[2] A. Walther, D. Givord, N. M. Dempsey, K. Khlopkov and O. Gutfleisch, J. Appl. Phys. 103, 043911(2008);

[3] C. Ndao , PhD thesis, 2010;

[4] http://hyperphysics.phy-astr.gsu.edu/hbase/quantum/bragg.html;

[5] G. Binnig, F. Quate and Ch. Gerber, Phys. Rev. Lett. 56, 930 (1986);

[6] G. Binnig and H. Rohrer, Scientific American 50, 253 (1985);

[7] L. Abelmann, *Magnetic Force Microscopy*, Encyclopedia of Spectroscopy and Spectrometry (2nd edition), 1415 (2010).

IV. Macroscopic characterization of coercivity in bulk and thick film NdFeB - based systems

Coercivity analysis was performed on two types of NdFeB samples, bulk and thick films, based on three experimental protocols: $H_c(T)$ and activation volume, $H_c(\theta)$, minor hysteresis loops.

In section IV.1 the temperature dependence of the coercive field and of the activation volume will be treated in the framework of both the micro-magnetic and global models. Measurements of the angular dependence of the coercive field and that of minor hysteresis loops will be discussed in section IV.2 and IV.3.

IV.1 Experimental analysis of the temperature dependence of the coercive field and of the activation volume

The samples that will be discussed in this section are listed in **Table 4. 1**. Bulk NdFeB - based magnets that were subjected to a NdCu infiltration treatment to increase H_c were provided by TMC. The infiltration process is described in chapter III. The base material is the material with no infiltration. In the name of the samples, "x % infiltrated", x represents the amount of NdCu to-be-infiltrated as a percentage of the base material.

For this analysis, we were provided with 5 platelets (6x6x1 mm^3) with different values of coercivity (**Table 4. 1**).

The temperature dependence of H_c in a series of films (**Table 4. 1**) will also be presented and the results compared to those of the bulk samples.

Sample		**$\mu_0 H_c$ (T) 300 K**
TMC bulk	Base material	1.46
	5% infiltrated	1.9
	10% infiltrated	2.1
	20% infiltrated	2.2
	30% infiltrated	2.42
Néel thick films	High H_c	2.5
	Medium H_c	1.2
	Low H_c	0.6

Table 4. 1 List of samples analyzed in this chapter.

IV.1.1 TMC bulk samples

Measurements at temperatures between 100 K and 400 K were done on cubes of 1x1x1 mm^3 cut by spark erosion from the original platelets. The hysteresis curves measured on the base material are shown in **Fig. 4. 1**. From 400 K down to 150 K, the hysteresis cycles have a normal square shape, with the coercive field progressively increasing from 0.65 T to 3.44 T. A minor phase shoulder is seen at low applied fields, which may be attributed to surface defects and misaligned grains, as discussed in [1]. At 150 K, another, more important shoulder appears and it becomes even more significant at 100 K. This is due to the low temperature (135 K) spin reorientation transition in the $Nd_2Fe_{14}B$ compound[2,3]. To note that the evaluation of magnetization in **Fig. 4. 1** might be overestimated (exact density of magnets not known). Nevertheless, this will not alter the analysis presented further, because, in the analysis, the spontaneous magnetization given in Annex 4 is used.

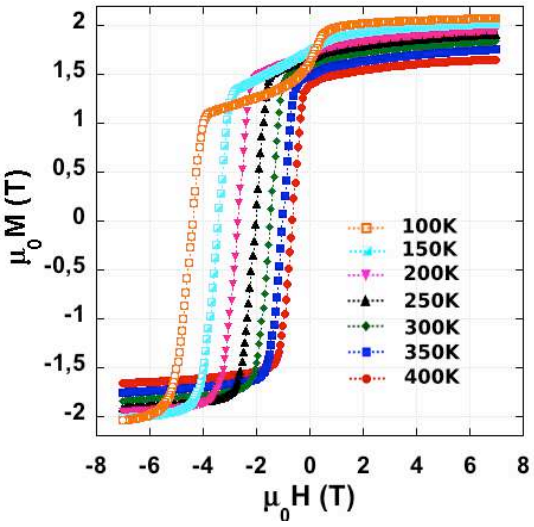

a)

Fig. 4. 1 Hysteresis curves corresponding to the TMC base material (see **Table 4. 1**), measured at different temperatures, in the range 100 K – 400 K.

The same type of curves was obtained for all the other samples. They are presented in Annex 10.

On each measured hysteresis cycle, the coercive field was determined using the following procedure: first, the magnetization variation in the vicinity of the coercive field was fitted to a polynomial function (see the continuous red line in **Fig. 4. 2**a for the base material at 400 K, between 0 and -1.4 T, corresponding to the experimental black dots). Then, using the values of magnetization and field from the fitted line, the derivative of magnetization variation M (H) was calculated (**Fig. 4. 2**b). The maximum of this curve represents the maximum of magnetic susceptibility and the corresponding field, also called switching field, is taken as the coercive field. At the switching field, the maximum number of reversal events occurs. In the case of bulk magnets presented here, the switching field and the coercive field are close in value, which is not the case in all the magnets.

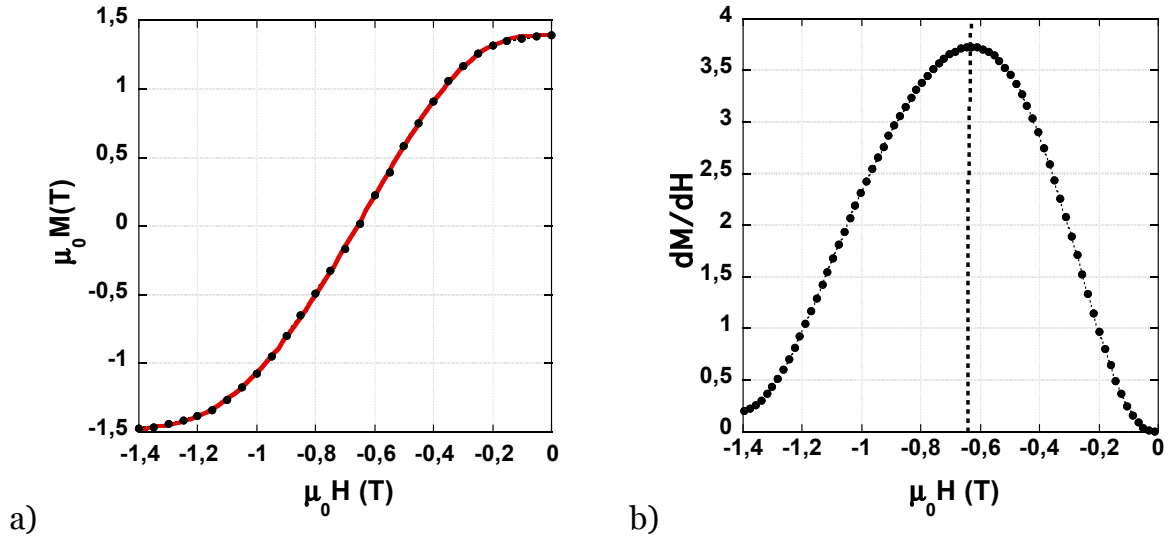

Fig. 4. 2 M(H) in the vicinity of the coercive field measured on the base material at 400 K **(a)** and the corresponding susceptibility function of the applied field plot **(b)**. The black dots in **(a)** correspond to experimental points; the red (continuous) line is the polynomial fit and the dotted vertical line in **(b)** corresponds to H_c.

Using the above procedure, the temperature dependence of the coercive field, $H_c(T)$, was evaluated for all the TMC samples (**Fig. 4. 3**).

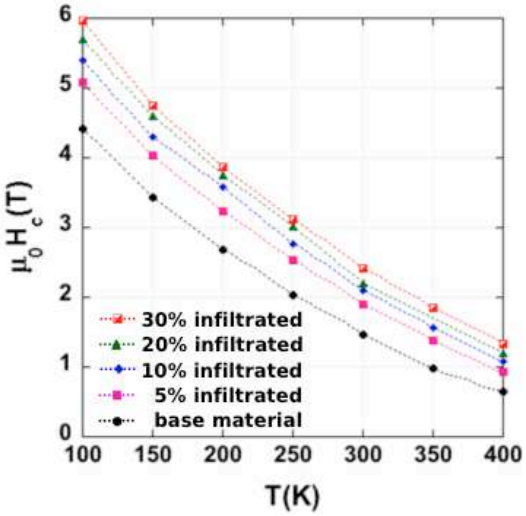

Fig. 4. 3 $H_c(T)$ for all the TMC bulk samples measured.

The coercivity of the base material increases from 0.65 T at 400 K to 4.4 T at 100 K. The behavior of the other samples is similar, though translated to higher coercive field values, with a maximum for the 30% infiltrated sample (H_c = 1.36 T at 400 K and H_c = 5.9 T at 100 K). From one sample to another, the biggest increase is between the base material and the 1st infiltrated sample. Afterwards, the increase from one sample to the other is almost constant and smaller in amplitude.

Before going further with the analysis of $H_c(T)$ within the two models, the increase of H_c with the infiltration degree will be considered in more detail for clarification.

In **Fig. 4. 4**, the increase of coercivity with the infiltration percentage is graphically presented at 4 different temperatures. The absolute value of the coercive field is shown in **Fig. 4. 4**a and the coercive field values, normalized to the 30% infiltrated sample coercivity, are shown in **Fig. 4. 4**b. The coercive field increases with increasing the degree of infiltration. Consider for example the 400 K data, the coercivity of the 5% infiltrated sample is 45% higher than that of the base material, that of the 10% infiltrated is 20% higher than that of the 5% infiltrated and that of the 30% infiltrated is only 11% higher than that of the 20% infiltrated one. We will show later that the degree of infiltration translates mainly in the degree of grain decoupling. This observation thus suggests that one tends to approach full grain decoupling as infiltration progresses.

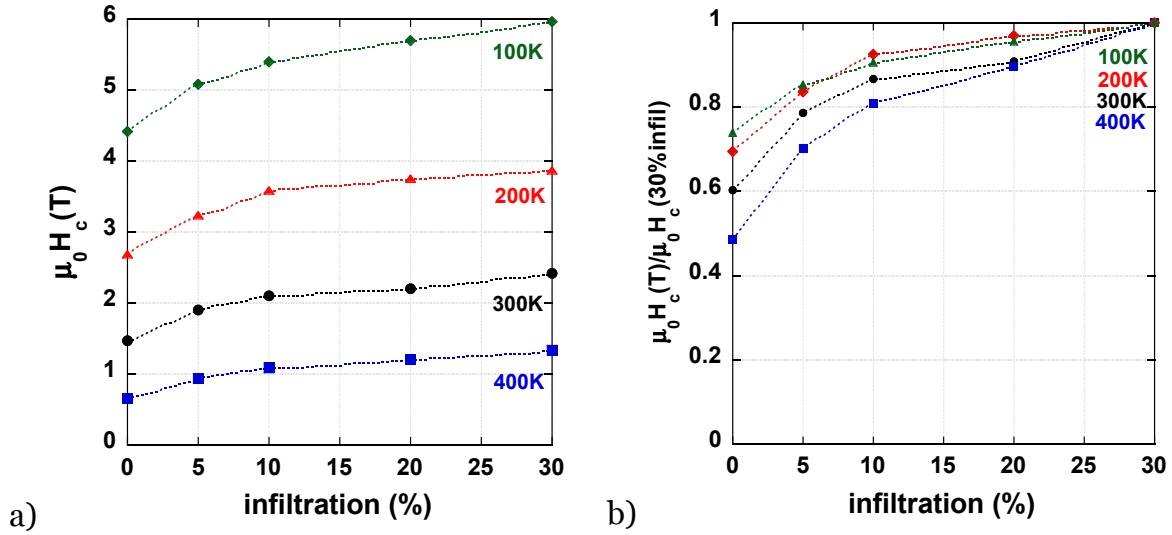

Fig. 4. 4 Coercivity as a function of infiltration degree measured at 4 different temperatures (100 K, 200 K, 300 K and 400 K) **(a)** and coercivity normalized to the 20% infiltrated sample's coercivity at same temperatures **(b).**

Another observation, from **Fig. 4. 4**b is that the increase from the base to the 1st infiltrated material is most significant at high temperature i.e. the decoupling of the grains becomes more effective at higher temperatures.

a) Analysis of $H_c(T)$ within the Micro-magnetic Model (MM)

Now we have all that we need to apply the MM analysis to the temperature dependence of H_c in these samples. This model was described in chapter II, section II.3.1. For the temperatures we are interested in, equation (2.10) applies:

$$H_c = \alpha \frac{2K_1}{\mu_0 M_s} - NM_s$$

The coefficients N and α can be determined by plotting (H_c/M_s) as a function of ($2K_1/M_s^2$) as shown in **Fig. 4. 5** for the base material. The parameter α is considered a constant. Its value indicates how much the anisotropy field is reduced due to micro-structural features. The black points in **Fig. 4. 5** are the experimental data obtained using the values of M_s and K_1 given in Annex 4. (For anisotropy constant, the values taken from[4] are used). The linear fit gives a value of 1.049 for N and 0.53 for α.

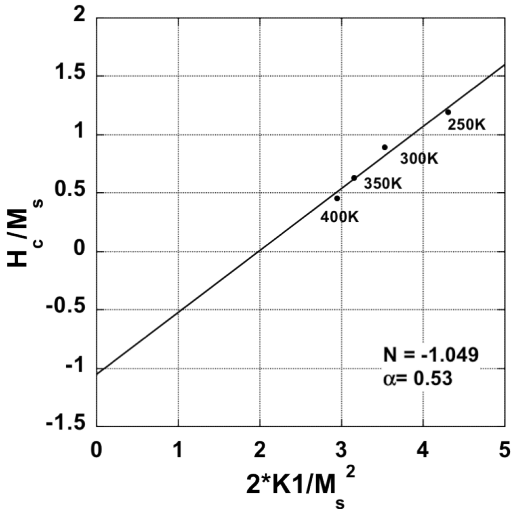

Fig. 4. 5 (H_c/M_s) vs. ($2K_1/M_s^2$) for the base material, experimental results (black dots) and linear fit (continuous line).

The same analysis was applied for the other samples and the corresponding values for N and α as a function of the degree of infiltration are presented in **Fig. 4. 6**. The value of α is around 0.5-0.6 and N is around 1 for all the samples.

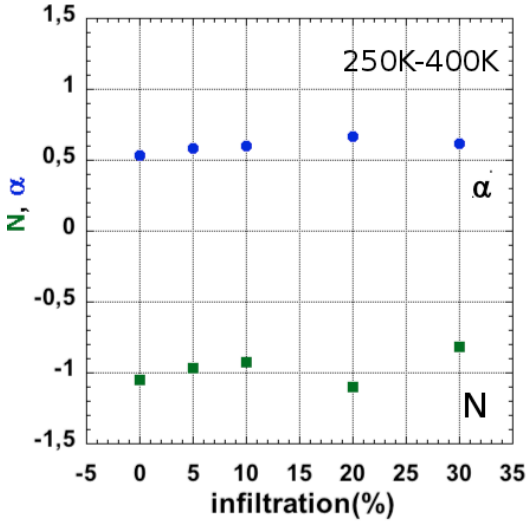

Fig. 4. 6 N and α (obtained using the micro-magnetic model analysis) as a function of infiltration degree for the TMC bulk samples.

To follow Kronmüller's model rigorously, α should be considered to change with temperature via the relation: $\alpha = \delta/\pi r_0$ where r_0 is the size of the defect. Then (H_c/M_s) should be plotted as a function of $(2\delta K_1/M_s^2)$, **Fig. 4. 7**a. The slope of this plot is equal to $1/\pi r_0$ so r_0 can be estimated. In **Fig. 4. 7**b, r_0 as a function of the infiltration degree is shown. The values are close to 1.5 nm - to be compared to the domain wall width in $Nd_2Fe_{14}B$, which varies from ≈ 2 nm at 4.2 K to ≈ 4 nm at 400 K.

a) b)

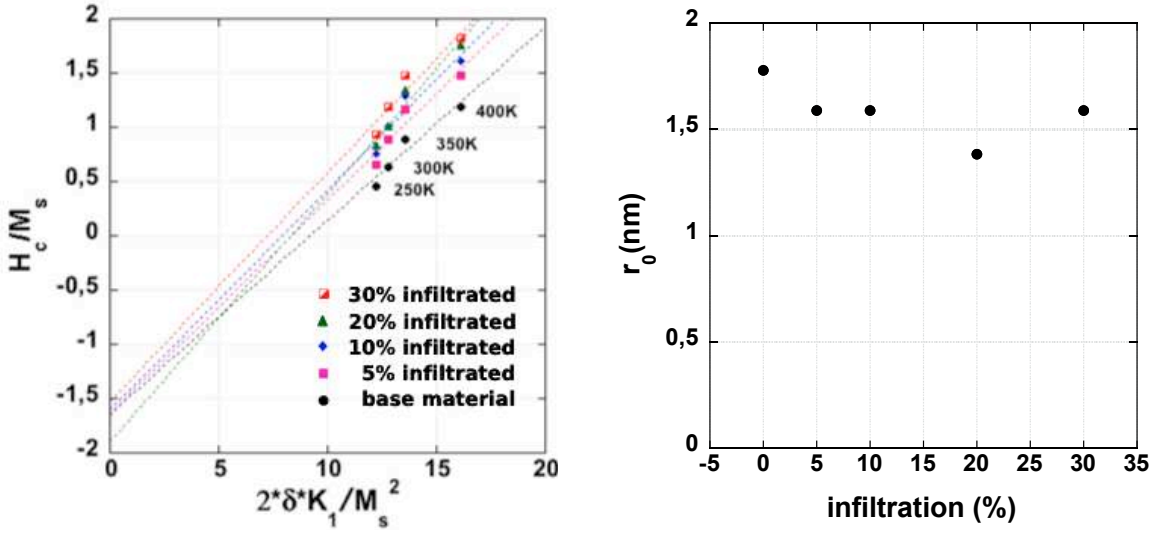

Fig. 4. 7 (H_c/M_s) as a function of $(2\delta K_1/M_s^2)$ for all TMC bulk samples **(a)** points - experimental; dotted lines - fit lines; and value of the size of the defect evaluated as a function of the infiltration degree **(b)**.

b) Analysis of $H_c(T)$ within the Global Model (GM)

The basic concepts behind this model were already presented in chapter II. In this case, another experimental parameter needs to be derived, the activation volume, (equation (2.19)):

$$v_a = \frac{k_B T}{S_v \mu_0 M_s}$$

where $S_v=S/X_{irr}$ can be calculated from experimental measurements. In the definition of S_v, the magnetic viscosity S is defined as dM/dlnt, the change of magnetization with time for a constant applied field and a constant temperature.

The protocol to calculate v_a is presented next for the base material at 400 K as an example. After saturating the sample in a direction along the easy axis of the material, a demagnetizing field is applied and the magnetization is measured for duration of typically 1 h. For each sample, we performed these measurements for a few values of the field at each temperature indicated in **Fig. 4. 1**. We know that time effects are more obvious when the field under which we observe them is close to the coercive field. In this situation, the height of the energy barriers is high enough for magnetization to not be reversed by the applied field alone and low enough so that in a few seconds after the field is applied, due to temperature fluctuations, jumps from an "up-state" to a "down-state" will happen. The M (t) curves for the base sample at 400 K are shown in **Fig. 4. 8**b and M (lnt) in **Fig. 4. 8**d. We observe the linear behavior of M with lnt and the slope of these lines is called the magnetic viscosity, S. The next parameter to be estimated is the irreversible susceptibility. For that, we make the difference between the total experimental susceptibility (from **Fig. 4. 8**a) and the reversible susceptibility that represents the slopes of the recoil loops in **Fig. 4. 8**c.

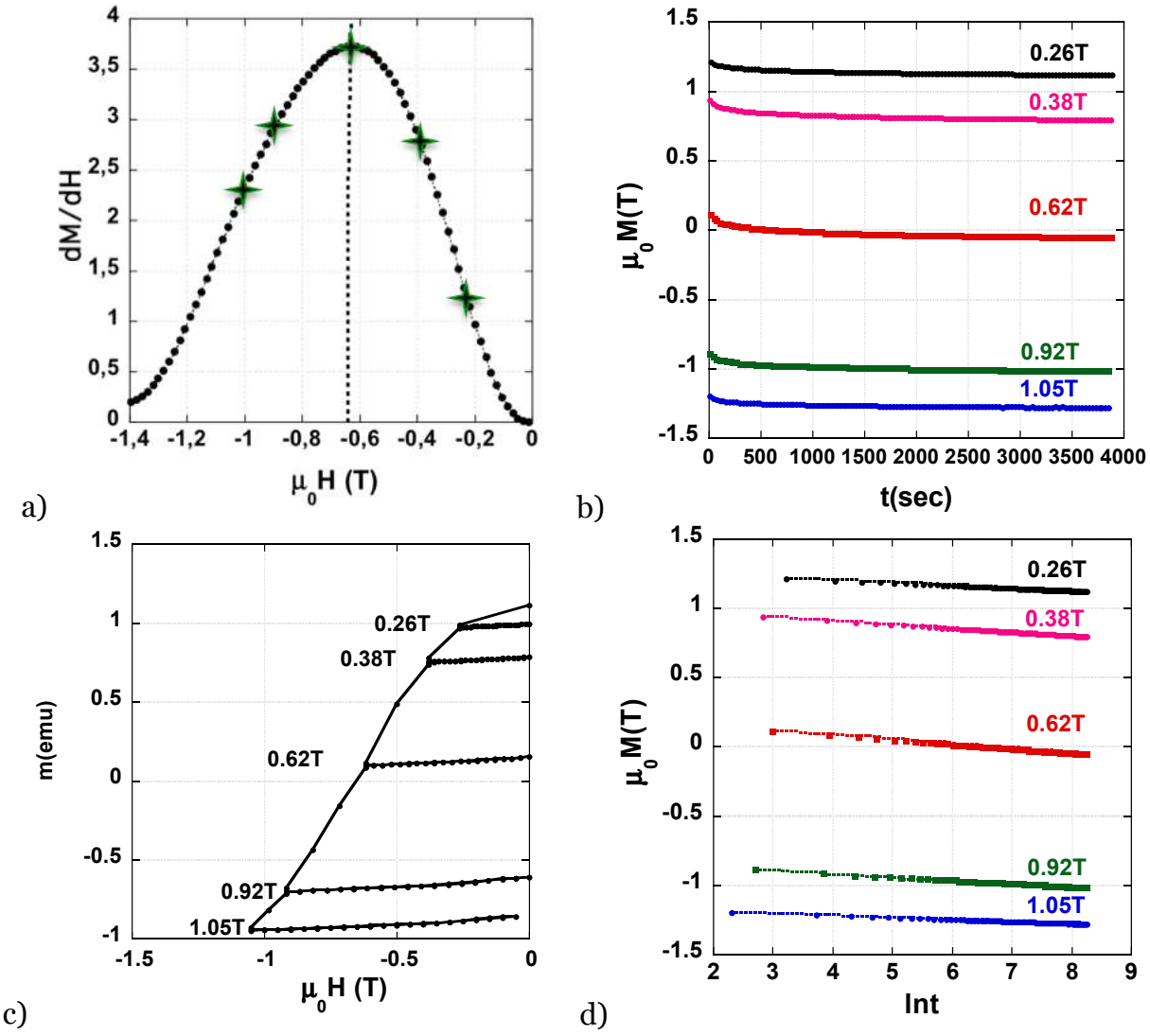

Fig. 4. 8 Magnetic susceptibility as a function of the applied field (a) Magnetization as a function of time (1h) for different values of the field (b); recoil loops used to estimate the reversible susceptibility corresponding to different magnetic fields (c) and magnetization as a function of Int (d). These measurements were performed on the base material at 400 K.

In **Fig. 4. 9**a, **Fig. 4. 9**b and **Fig. 4. 9**c, S, X_{irr} and S_v are plotted versus the applied field and the magnetization corresponding to that applied field for the base material, at 400 K. However, since the magnetization varies with time, the value of the applied field alone cannot be used to characterize the magnetization state. Rather, a given magnetic state may be considered to be determined by the value of the material's magnetization. It is thus more significant to plot S and X_{irr} as a function of the magnetization at which these parameters have been obtained. Both the magnetic viscosity and the irreversible susceptibility present a maximum close to the coercive field (see **Fig. 4. 9** for the base material at 400 K). Taking the ratio of the two we get the magnetic viscosity coefficient, S_v, that is basically constant in the magnetization window considered here.

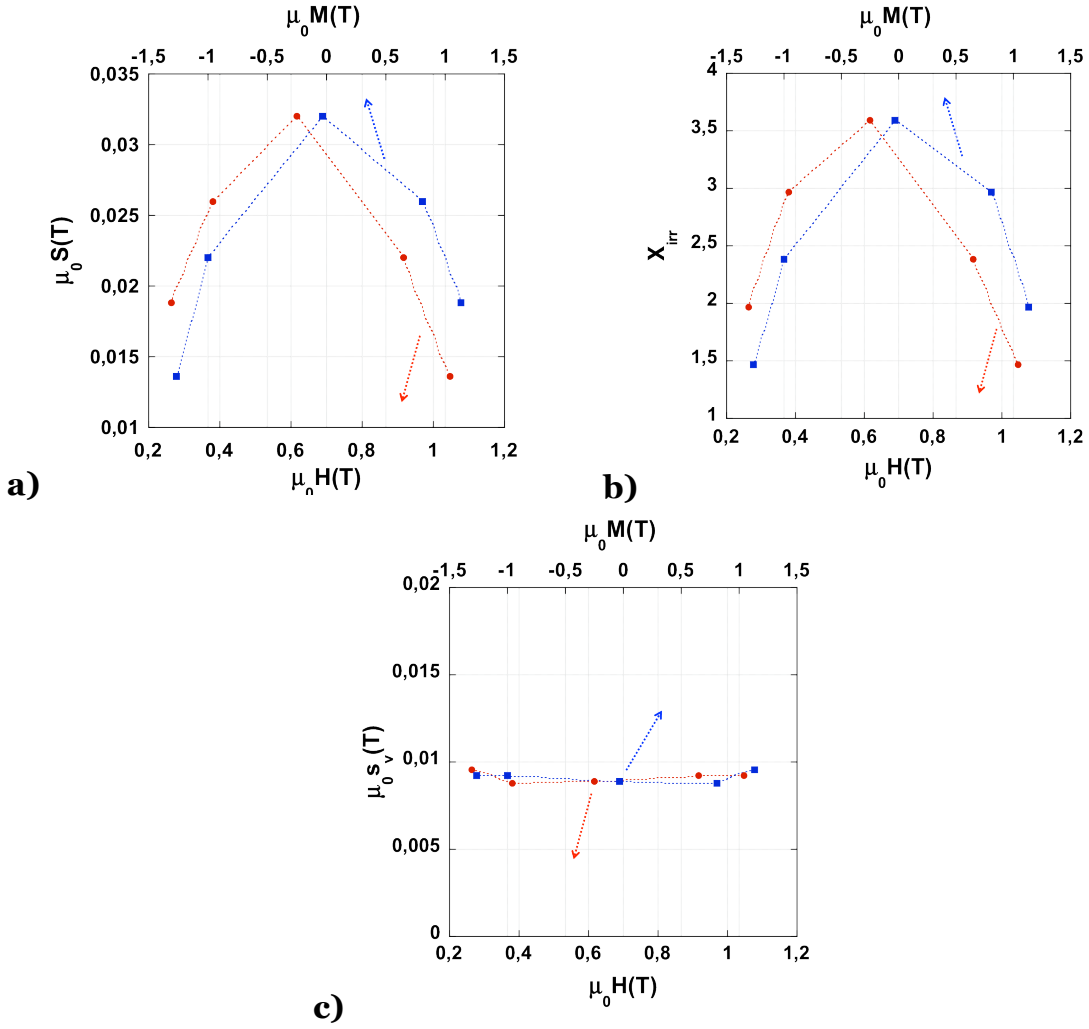

Fig. 4. 9 Magnetic viscosity, S **(a)**, irreversible susceptibility, X_{irr} (b) and magnetic viscosity coefficient, S_v (c) as a function of field and magnetization corresponding to the base material at 400 K.

The same type of measurements and calculations were applied for all the samples at different temperatures, from 100 K to 400 K and the activation volume was derived in each case. The results are shown in **Fig. 4. 10** for all the bulk samples. For a specific sample, at a fixed temperature, the activation volume's size does not change significantly for different values of the demagnetizing applied field. By decreasing the temperature, v_a decreases, the influence of temperature becoming less and less important. So, the activation volume is a parameter that characterizes the sample at a certain temperature and it does not depend on the value of the field applied, when close to the coercive field.

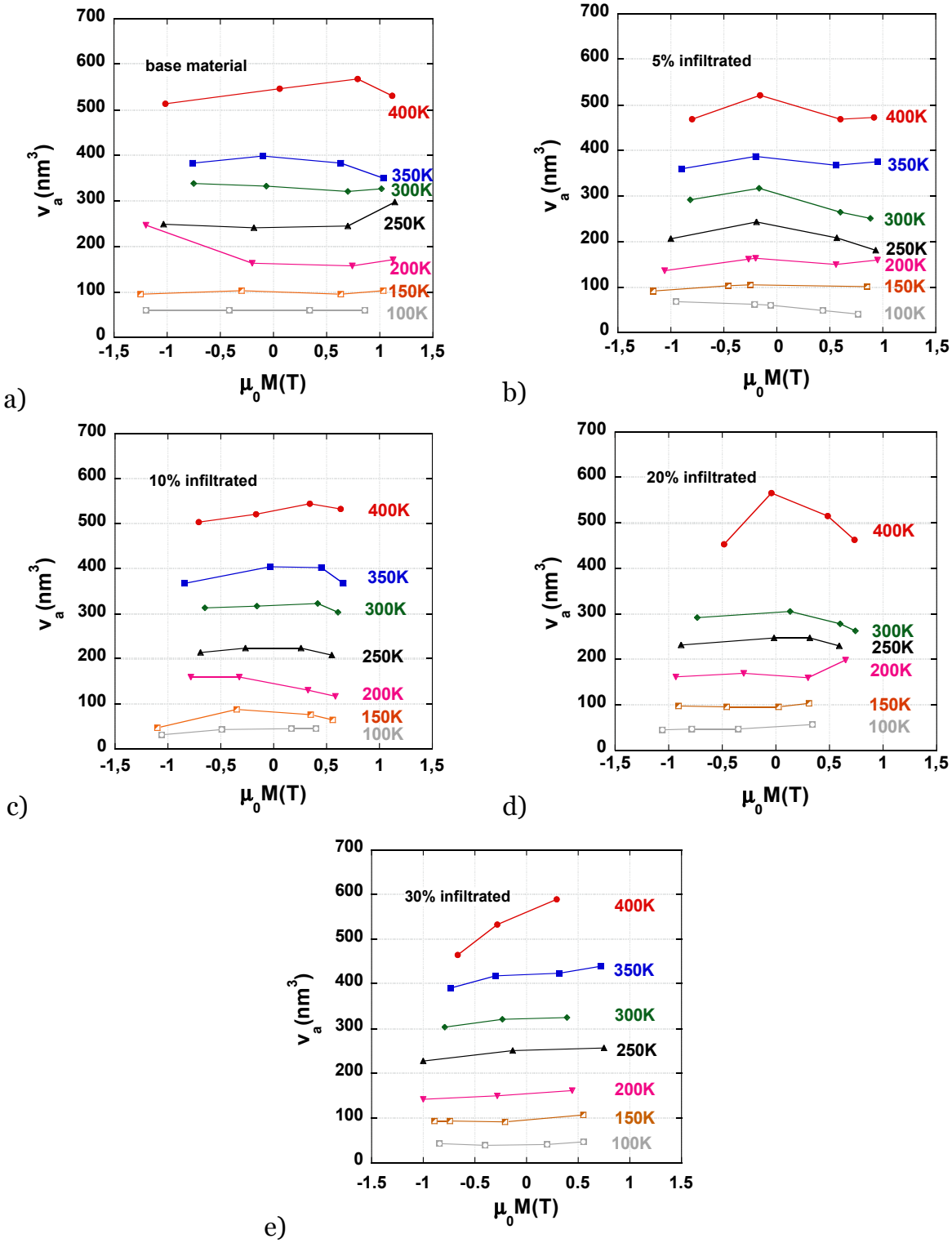

Fig. 4. 10 Activation volume as a function of magnetization, at different temperatures for: base material **(a)**; 5% infiltrated sample **(b)**; 10% infiltrated sample **(c)**; 20% infiltrated sample **(d)** and 30% infiltrated sample **(e).**

For each sample, a unique value, corresponding to μ_0M=0 T, was determined for each temperature from the graphs in **Fig. 4. 10**. That is the v_a characterizing the sample at that specific temperature. Extracting these numbers and plotting them as a function of the temperature, one gets the curves in **Fig. 4. 11**a. The graph in this

figure shows the way activation volume varies with temperature in the case of all the considered bulk samples.

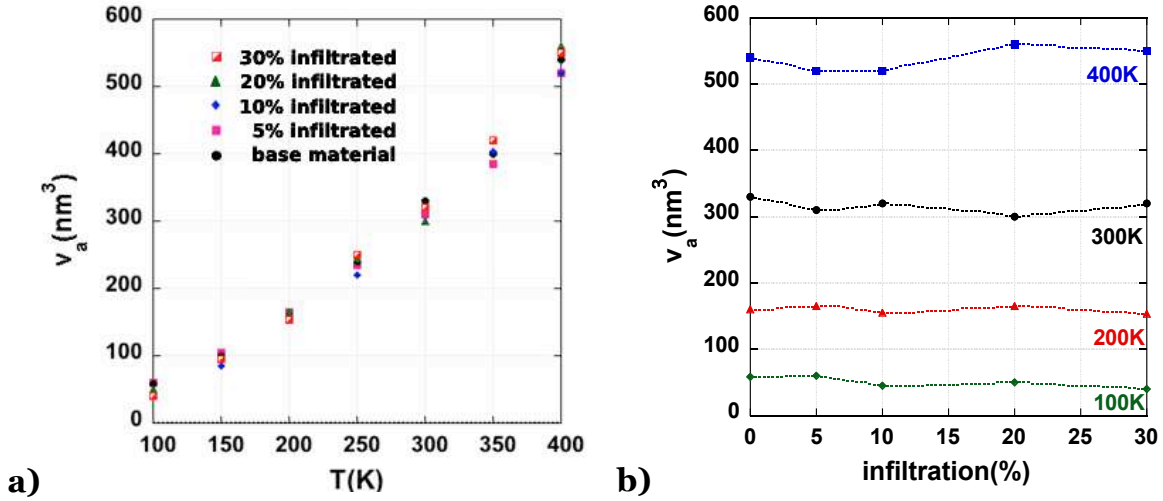

Fig. 4. 11 Activation volume as a function of temperature for the 5 samples (a) and activation volume as a function of the infiltration degree for 100 K, 200 K, 300 K and 400 K (b).

For all the samples, v_a increases monotonously from values of around 50 nm at 100 K up to values of around 550 nm at 400 K. At a given T, it does not change much from one sample to the other.

The curves in **Fig. 4. 11**b present the activation volume as a function of infiltration degree (and thus coercivity) at 100 K, 200 K, 300 K and 400 K.

As discussed for ex. in [5] the activation volume is associated to the formation of a non-uniform magnetic configuration, which must be reminiscent of a magnetic domain wall. Thus it is legitimate to compare the size of the activation volume with the size of magnetic domain walls in $Nd_2Fe_{14}B$. The ratio between v_a and the cube of the domain wall is 2-3 at 100 K and it increases with T to reach 7 at 400 K (**Fig. 4. 12**). Similar results were presented for bulk magnets[6].

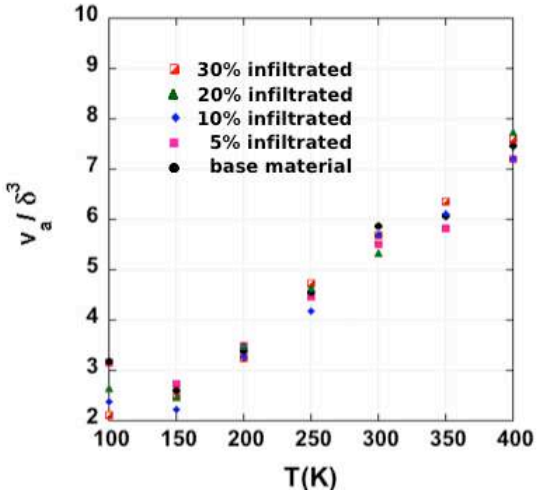

Fig. 4. 12 (v_a/δ^3) as a function of temperature for all TMC bulk samples.

If the coercive field in **Fig. 4. 3** is corrected for thermal activation effects, equivalent to a field amounting to $25S_v$, one obtains the curves shown in **Fig. 4. 13**

($H_0=H_c+25S_v$). H_0 represents the field needed to reverse the magnetization if thermal energy would not be involved.

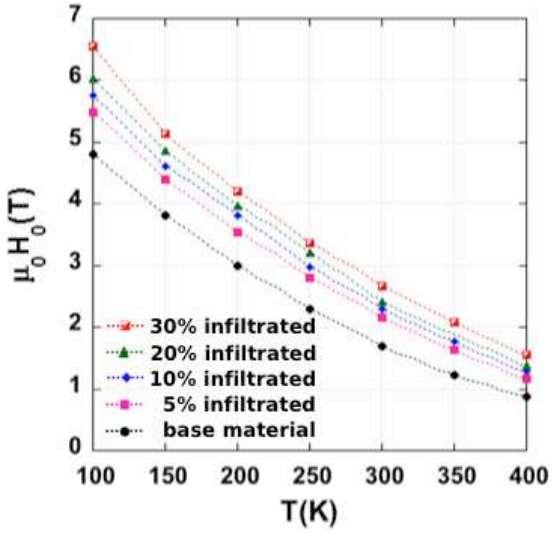

Fig. 4. 13 Coercive field corrected for thermal effects ($H_0=H_c+25S_v$) as a function of temperature for TMC bulk samples

Plotting (H_0 / M_s) versus $\gamma / (\mu_0 M_s^2 v_a^{1/3})$ **Fig. 4. 14a**, we can extract N and α, **Fig. 4. 14**b. The values of α are all around 1.2-1.3 while N increases for the samples 10% infiltrated and above, compared to the base material and 5% infiltrated samples.

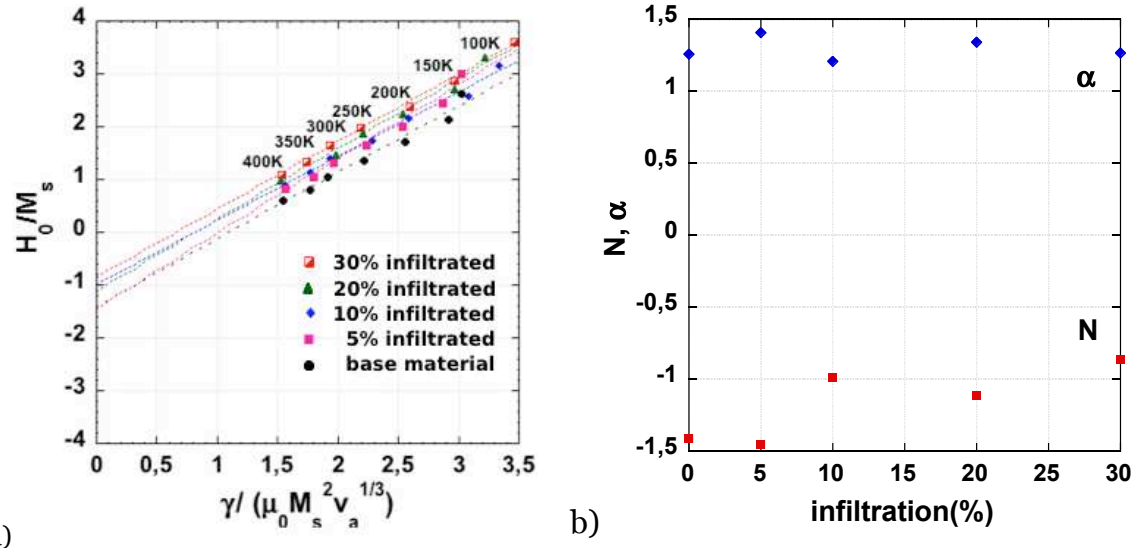

a) b)

Fig. 4. 14 (H_0/M_s) versus $\gamma / (\mu_0 M_s^2 v_a^{1/3})$ for TMC bulk samples **(a)** dots - experimental points; discontinuous lines: linear fit; N and α as a function of the infiltration degree **(b)**.

TMC bulk samples. Micro-magnetic Model vs. Global Model

The values of N and α, obtained using the global (N^G and α^G) and the micro-magnetic (N^M and α^M) model, respectively, are presented in **Table 4. 2**.

Sample	N^G	N^M	α^G	α^M
Base material	1.42	1.05	1.26	0.54
5% infiltrated	1.46	0.97	1.41	0.58
10% infiltrated	0.99	0.93	1.21	0.6
20% infiltrated	1.12	1.1	1.34	0.66
30% infiltrated	0.87	0.8	1.27	0.61

Table 4. 2 Values of N and α obtained for TMC bulk samples using the global model (N^G and α^G) and micro-magnetic model (N^M and α^M).

The physical meaning of α is not the same in the two models. In the micro-magnetic model, it is assumed that the reversal starts in areas with much lower anisotropy than the bulk and α gives an indication about how much the anisotropy is lowered in those volumes. The values found here are around 0.6. According to Kronmüller this corresponds to reversal by nucleation[7]. In the global model, the parameter α does not have a simple physical meaning. It relates the coercive field to some parameters of the main hard phase. In both models, the parameter N is expected to represent the size of the demagnetizing field.

The small variation of α from one sample to another in the sample series suggests that the area where reversal starts is magnetically similar for all samples. The same idea can be associated to the insignificant variation of the activation volume across the serie of samples, at a specific temperature (see **Fig. 4. 11**b). If we take into consideration that the size of the activation volume is of the same order of magnitude as the cube of the magnetic domain wall corresponding to bulk $Nd_2Fe_{14}B$ (**Fig. 4. 12**), then we may say that the magnetic properties of the critical volume are not much different from those of the bulk material.

Since α fluctuates across the series around a constant value, it can be assumed that the observed fluctuation is due to measurement uncertainty. This suggests to fix arbitrarily the same value of α for all the samples (let's say 0.6 for MM and 1.3 for GM). The variation of the re-calculated N thus obtained is shown in **Fig. 4. 15**. The absolute value of N decreases continuously from the sample with the lowest coercive field (base material) to the one with the maximum coercive field (30% infiltrated).

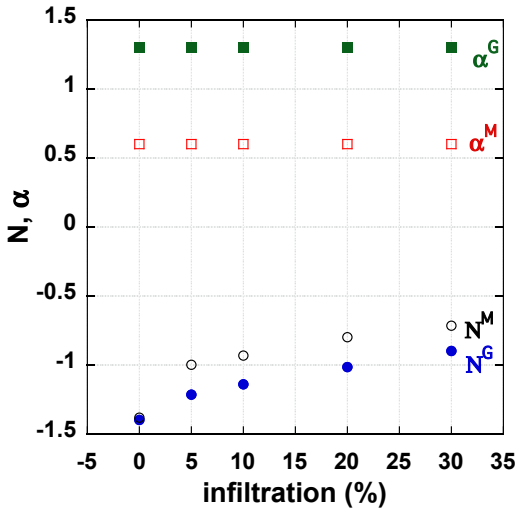

Fig. 4. 15 Values of N and α obtained for TMC bulk samples using the global model (N^G and α^G) and micro-magnetic model (N^M and α^M) when the value of α is fixed (0.6 for MM and 1.3 for GM). N is taken negative here to make the graph easier to read.

Thus, from the coercivity and activation volume function of temperature analysis, it can be concluded that the difference in H_c between the samples is mostly due to differences in demagnetizing fields (through N). These fields are inhomogeneous throughout the sample. The activation volume will be formed at the positions where the sum of the applied field and the dipolar one is maximal.

IV.1.2 Thick films

Coercivity analysis of two thick films of NdFeB based magnetic material was carried out in the framework of the global model*. The films were prepared using the triode sputtering technique. One of them has grains slightly elongated and high coercivity at room temperature (2.5 T at 300 K) and the second one has a columnar microstructure and a medium† coercivity (1.2 T at 300 K).

The hysteresis loops for the high H_c and medium H_c samples that were measured at temperatures between 300 K and 4.2 K are shown in **Fig. 4. 16**. The behavior of the high coercivity sample is similar to the bulk ones, with the appearance of the shoulder at low temperatures. When considering the second sample, the slope of the demagnetization loop changes at temperatures <=150 K. Even if the switching field increases continuously when lowering the temperature, as shown in **Fig. 4. 17**, the field value corresponding to the intersection of the demagnetization curve with the field axis increases down to 100 K and then it decreases.

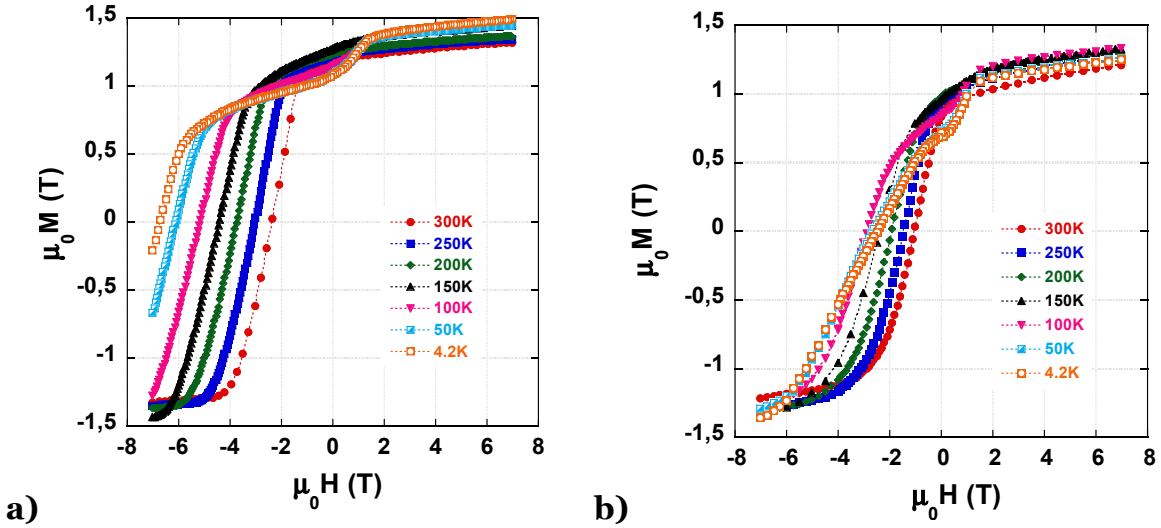

Fig. 4. 16 Hysteresis loops measured at temperatures between 300 K and 4.2 K for a high H_c thick film (a) and a medium H_c thick film (b).

From the graphs above, the coercive (switching as always in this chapter) field function of temperature, $H_c(T)$, is deduced and plotted in **Fig. 4. 17** for the high coercivity (full dots) and medium coercivity sample (full squares).

In the same graph, **Fig. 4. 17**, the coercive field corrected for thermal activation effects, as a function of temperature, $H_0(T)$, is also shown, for the high H_c

---

* The analysis in the framework of the MM model was not possible in this case because of the limitation in temperature of the magnetometer that was used when the analysis of these films started.

† To differentiate between different thick films analyzed in this thesis, they are named either "high H_c" when $H_c > 1.5$ T, "medium H_c" if $0.8\ T < H_c < 1.5$ T or "low H_c" when $H_c < 0.8$T.

sample(empty dots) and the medium H_c sample (empty squares). The difference between the $H_c(T)$ and $H_0(T)$ represents the field equivalent to thermal activation effects. It is around 280 mT for high H_c and 230 mT for medium H_c at 300 K, it decreases slowly with decreasing temperature, to reach 60 mT at 4.2 K for both samples. At this temperature, the thermal activation effects are almost negligible.

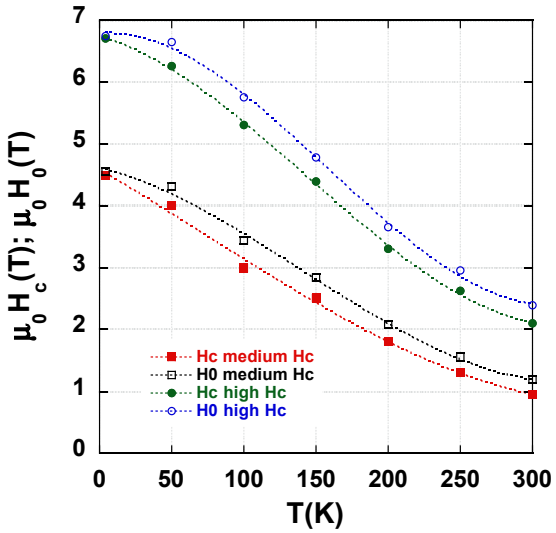

Fig. 4. 17 H_c and H_0 (=H_c+25S_v) function of temperature for a high H_c and a medium H_c thick films.

Following the usual procedure, the viscosity coefficient and activation volume were derived from the experimental results, **Fig. 4. 18**a and **Fig. 4. 18**b. S_v passes through a maximum at about 150 K and it is very small at 4.2 K. The activation volume increases from a value of 17 nm at 4.2 K for the two samples up to around 350 nm for the columnar sample and 270 nm for the high H_c sample, at RT.

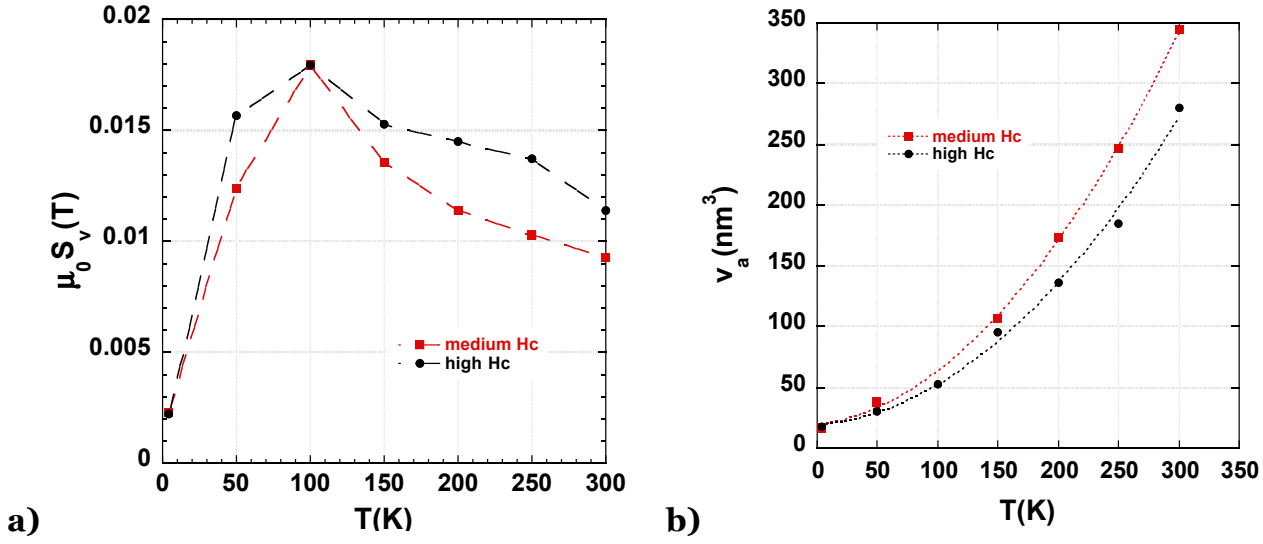

Fig. 4. 18 Magnetic viscosity coefficient, S_v, as a function of temperature **(a)** and activation volume as a function of temperature **(b)** for the high H_c and medium H_c thick films.

The ratio v_a/δ^3 (T) is in agreement with previous studies on bulk samples. It stays between 2 and 6, **Fig. 4. 19**.

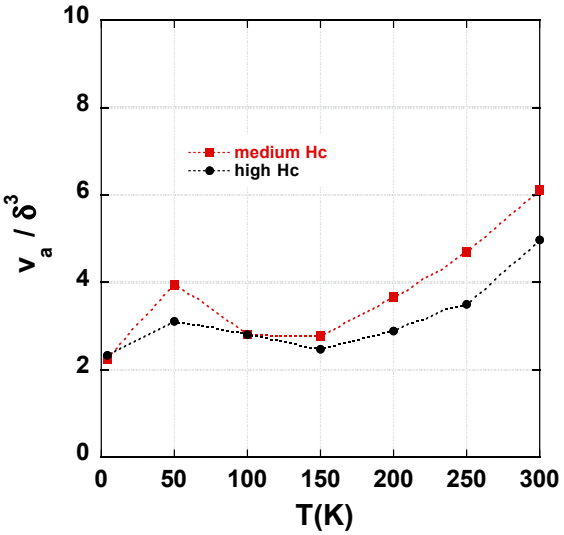

Fig. 4. 19 (v_a/δ^3) as a function of temperature for high and medium H_c thick films.

Applying the global model, the graph from **Fig. 4. 20** is obtained. The black and red dots correspond to experimental data for the two films. The dotted lines represent a linear fit giving the values for N and α : (N= -1.18; α= 1.25) for high H_c and (N= -1.04; α= 0.9) for medium H_c.

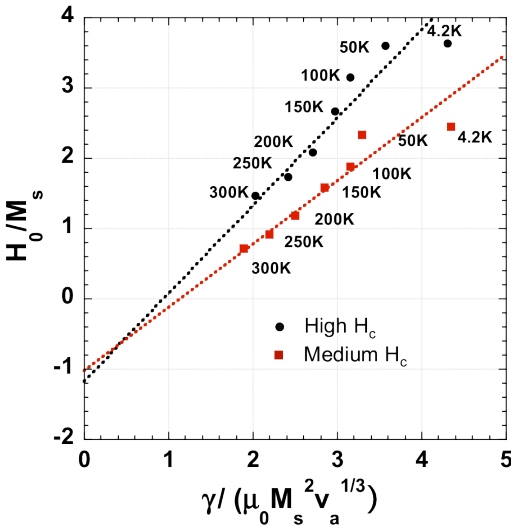

Fig. 4. 20 (H_0/M_s) vs. ($\gamma/\mu_0 M_s^2 v_a^{1/3}$) for high H_c and medium H_c thick films.

The activation volume is always bigger for the medium H_c sample above the spin reorientation temperature, **Fig. 4. 18**b. This, together with the difference in grain size and in the degree of magnetic decoupling between grains, could explain the difference in coercivity between the two thick films considered here.

IV.2 Angular dependence of coercivity

The evolution of coercivity with the angle between the direction of the applied field and the direction of the easy axis was studied experimentally. The samples that were used in the experiments are of the same type studied above: either bulk sintered magnets provided by TMC or thick films of NdFeB deposited by triode sputtering.

In the interest of comparing the results with expected behavior for different reversal processes, an analytical model was developed. The details of the calculations are presented in Annex 3.

IV.2.1 Experimental results. Bulk samples provided by TMC

Angular dependency measurements were performed on 4 samples provided by TMC: the base material, the 5, 10 and 20 % infiltrated (see above, page 37). The samples were parallelepipeds of 5x5x0.5 mm^3 on average. After saturation along the easy direction, the sample was rotated by a certain angle (0° to 85°), the direction of the field was inverted and the demagnetization curve measured. The demagnetization part of the hysteresis loops for all the samples, measured at 300 K, for a series of angles, are shown in **Fig. 4. 21.**

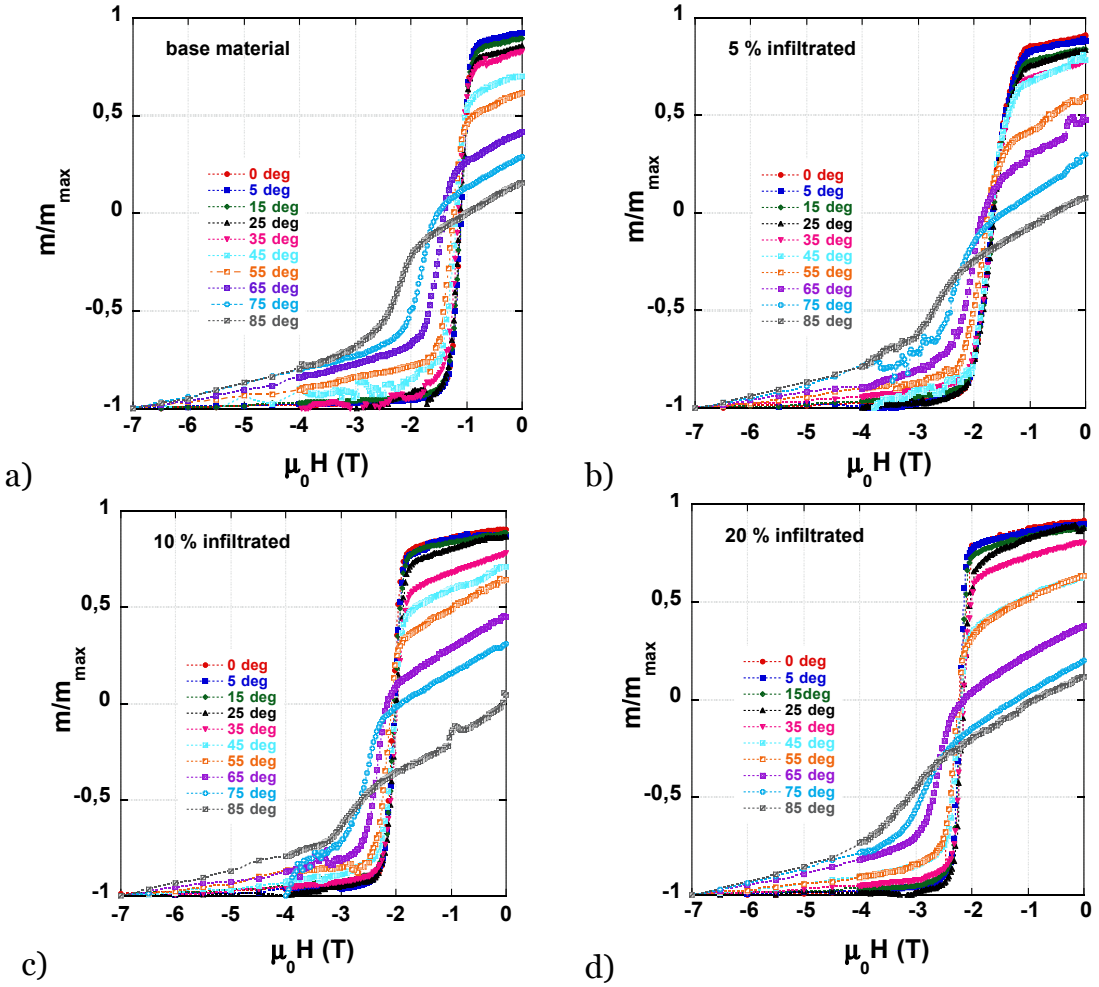

Fig. 4. 21 Demagnetization hysteresis loops measured at 300 K, for different orientations of the applied field, for TMC bulk.

The angular dependence of the switching field derived from the curves in **Fig. 4. 21** are displayed in **Fig. 4. 22**a. The same curves, normalized to the coercivity at $\theta = 0°$, are shown in **Fig. 4. 22**b. As a reminder, 0° means the applied field is antiparallel to the magnetization direction. The coercive field increases continuously with the angle for all samples. However, the rate of increase varies from one sample to another. Actually, up to 45° the coercive field does not change in a significant manner. At larger angles, the increase is more important and a maximum of 2 $H_c(0)$ is obtained for the base material at 85°. The observed behavior is closer to the Kondorsky $1/\cos(\theta)$ law than to the SW one (see chapter II) for all the samples, the base material (lowest H_c) being the one where the increase in H_c at large angle is the strongest. These results are essentially similar with previous results[8,9,10]. In particular, it is found that the $1/\cos(\theta)$ law tends to be better followed in samples having relatively lower coercivity.

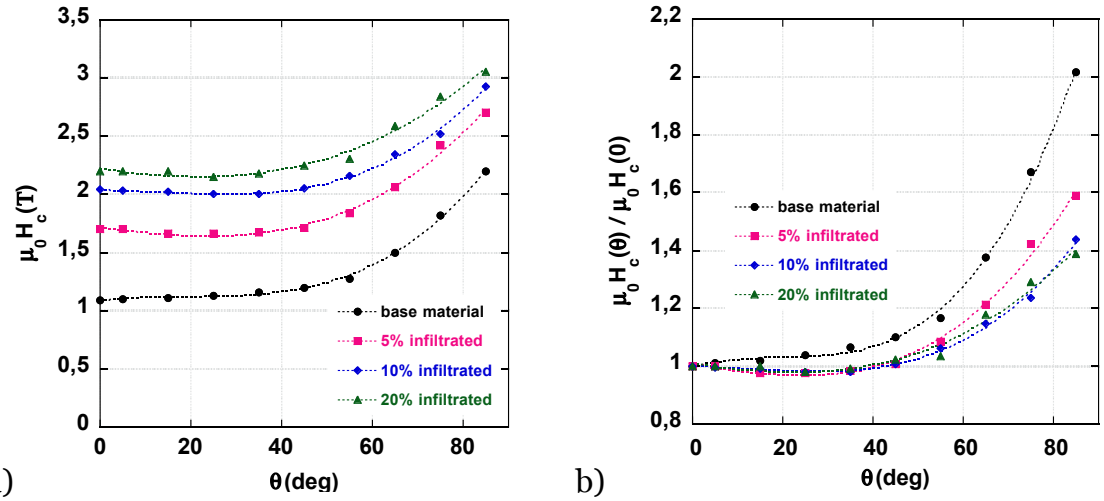

Fig. 4. 22 Angular dependence of the coercive field, measured at 300 K, for all the TMC bulk samples (a) and the angle dependence of the coercive field normalized to $H_c(0°)$ (b).

For comparison, the base material was measured in the same way, at 175 K, above the spin reorientation temperature. Results are shown in **Fig. 4. 23**a. **Fig. 4. 23**b and **Fig. 4. 23**c show the $H_c(\theta)$ curves for 300 K and 175 K, respectively. The angular dependence of H_c is similar in both cases except at larger angle, where the coercivity at 175 K tends to saturate whereas at 300 K it continues increasing with the angle.

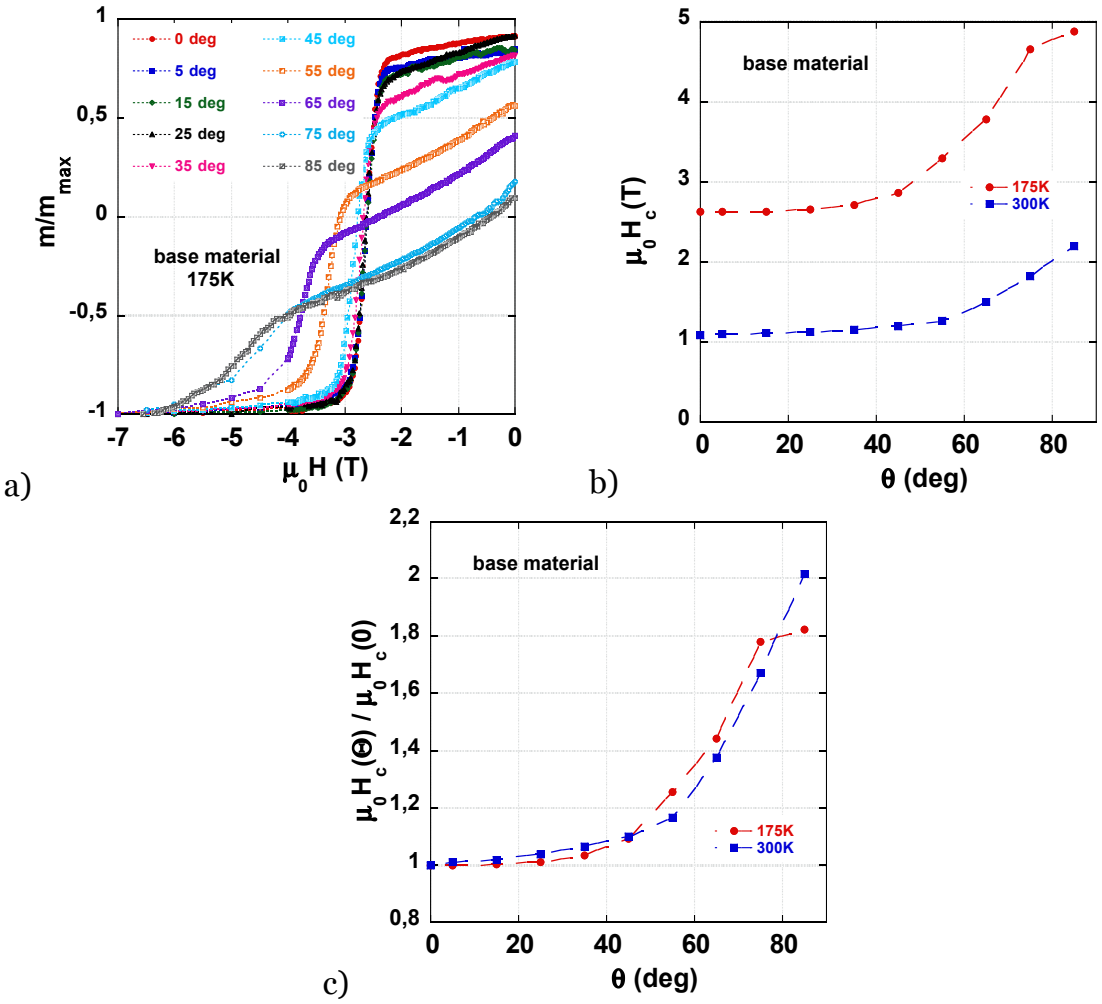

Fig. 4. 23 Demagnetization loops of the bulk base material, measured at 175 K for different orientations of the applied field (a); coercivity evolution as a function of the angle of the applied field for the base material, at 300 K and 175 K (b); the same two curves from (b) with the coercive field normalized to the value of $H_c(0°)$ (c).

IV.2.2 Experimental results. NdFeB-based thick films

The variation of H_c as a function of θ for a high coercivity NdFeB-based thick film ($\mu_0 H_c$=1.5T at 300 K) is shown next. The demagnetization curves for this sample are shown in **Fig. 4. 24**a.

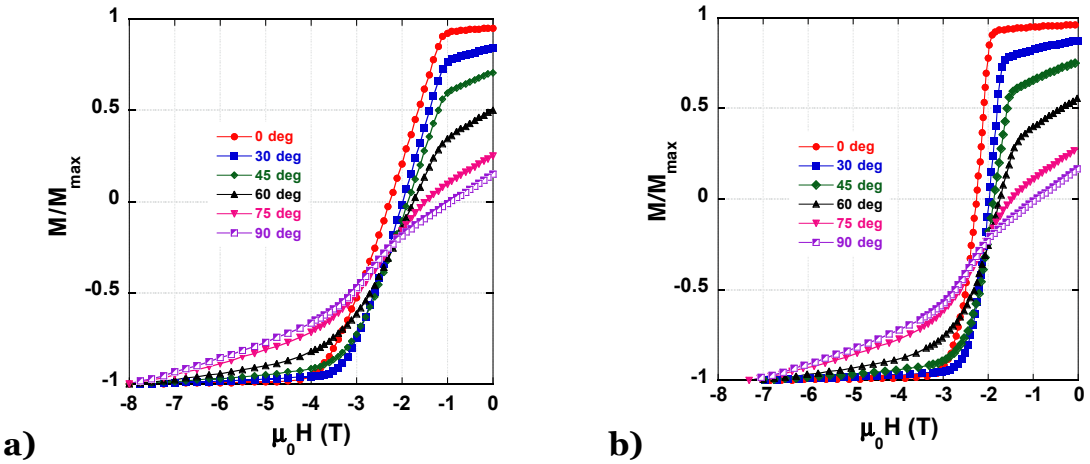

Fig. 4. 24 Demagnetizing loops corresponding to a high H_c thick NdFeB film, for different θ a) as measured; b) after correcting for demagnetizing effects;

The curves were corrected for demagnetizing field (-NM/cos(θ) with N=2/3), using the indications presented in [11]. The curves after correction are shown in **Fig. 4. 24**b). The coercive field normalized to the 0° coercive field as a function of the angle is shown in **Fig. 4. 25** for both cases, corrected and non-corrected. The behavior is similar to the one found in bulk samples and presented in the previous section. The relatively slight differences between the two curves cannot easily be exploited because of the large demagnetizing field present in this system and the uncertainty in how the applied corrections may affect the results.

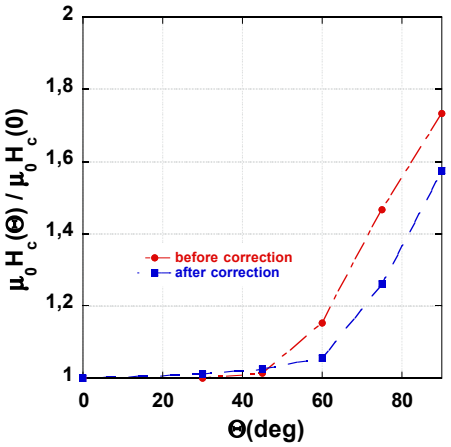

Fig. 4. 25 $H_c(\theta)$ for a NdFeB thick film, w/ and w/o demag. field correction.

IV.2.3 Fit of the experimental curves with calculated ones

In Annex 3, two models to calculate hysteresis loops for assemblies of uni-axial decoupled particles are described: the first corresponding to the SW model and the second one to the Kondorski model ($1/\cos(\theta)$ law) – see chapter II. In the first case, the coercivity of a fully textured system is equal to the anisotropy field while the second model "allows" magnetization to reverse for values of field that are smaller than the anisotropy field.

If we compare the angular dependence of coercivity given by the calculation (**Fig. A3.7**a and **Fig. A3.7**b) to the results obtained from experiments (**Fig. 4. 22**b and **Fig. 4. 25**) we observe that, qualitatively, the Kondorski ($1/\cos(\theta)$)law, taking into account an angular distribution of easy axes, described better the experimental results than the SW law.

A direct comparison of the measured and calculated hysteresis loops was tried, as shown in **Fig. 4. 26** for the base material and 20 % infiltrated bulk samples at 0° and 65°. The two samples have the least and the most inter-granular phases, respectively. At 0°, the experimental and calculated curves match closely (**Fig. 4. 26**a and **Fig. 4. 26**c) except for the base material at field values around -1 T. By contrast, at 65° **(Fig. 4. 26**b and **Fig. 4. 26**d), the experimental slopes of the magnetization variation are more abrupt than the calculated variations. The slopes of the linear part of the loops are compared in **Table 4. 3**.

	Base material	**20 % infiltrated**
65 deg_exp.	1.87	1.54
65 deg_calc.	0.7	0.53

Table 4. 3 Slopes of the linear part of the curves in **Fig. 4. 26**.

The abrupt drop of the experimental loops may be tentatively attributed to collective effects that were not considered in the calculations. It can be seen that the beginning of the slopes coincide but then, the experimental one falls off quicker. If there are grains that are magnetically coupled, once one was reversed, it will reverse all the other ones that are coupled and this could explain the observed big drop in magnetization. We can also see that the difference in slope between the calculated and the experimental loops is smaller in the case of the sample that contains grains which are mostly decoupled, the 20 % infiltrated sample - **Table 4. 3**.

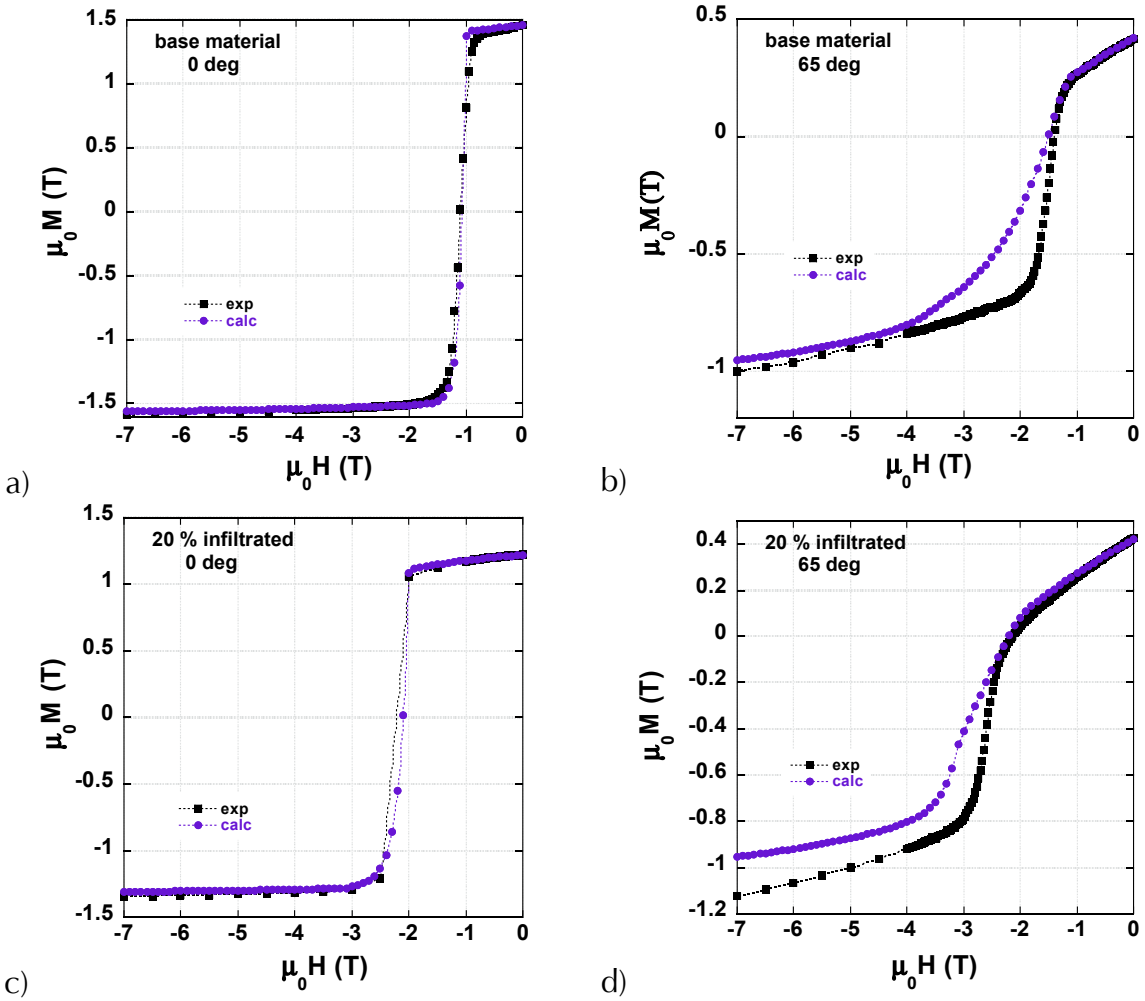

Fig. 4. 26 Experimental vs. calculated hysteresis loops corresponding to the base material for $\theta = 0°$ (a) and $\theta = 65°$ (b) and the 20 % infiltrated sample for $\theta = 0°$ (c) and $\theta = 65°$ (d).

IV.3 Minor loops

The most common and easy technique of analyzing magnetic materials consists of measuring major hysteresis loops. It gives important information like the value of coercive field, that of the remanence etc. Together with the first magnetization curve, it can also provide information about the magnetic domain structure, the movement of domain walls and rotation of magnetic domains. A less exploited area is that of minor loop analysis. The resulting data depend on the applied field and its physical interpretation can be more complicated.

Starting from a thermally demagnetized state of a sample, the experimental procedure followed here consists in progressively increasing the applied magnetic field. This is shown schematically in **Fig. 4. 27**: starting from H=0, the field is increased to $+H_{a1}$, decreased to $-H_{a1}$ and increased back up to a $H_{a2}>H_{a1}$, decreased back to $-H_{a2}$, etc. The procedure was followed up to a maximum of the applied field, H_{amax} of 7T when the minor loops become actually the major loop characterizing the system.

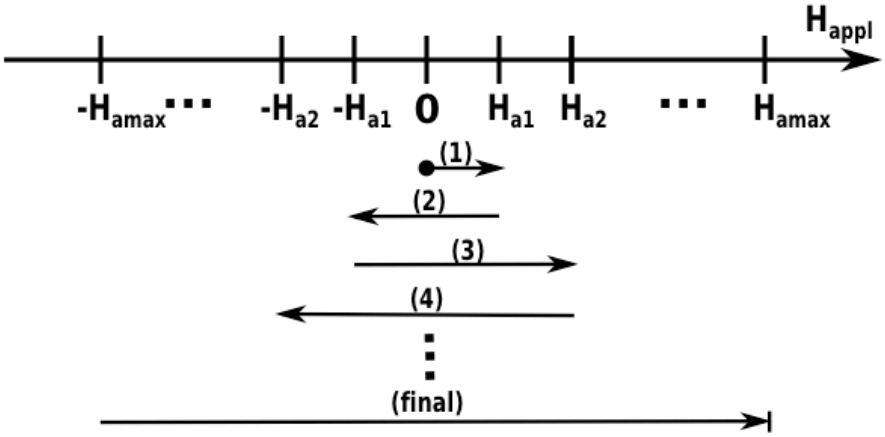

Fig. 4. 27 Schematic representation of the minor loop measurement procedure.

The type of measurement described in the previous paragraph was applied to two thick NdFeB films, a high coercivity (H_c= 2.3 T at 300 K) and a low coercivity (H_c=0.6 T at 300 K) one, at two temperatures: 300 K and 200 K. A small step of 0.1 T was chosen up to 1.1 T in order to be able to resolve the development of coercivity in small fields. The results are compared for the high and low coercivity sample at 300 K in **Fig. 4. 28**a and **Fig. 4. 28**b with a "zoom in" on the -1.1 T - +1.1 T part of the curves, **Fig. 4. 28**c and **Fig. 4. 28**d.

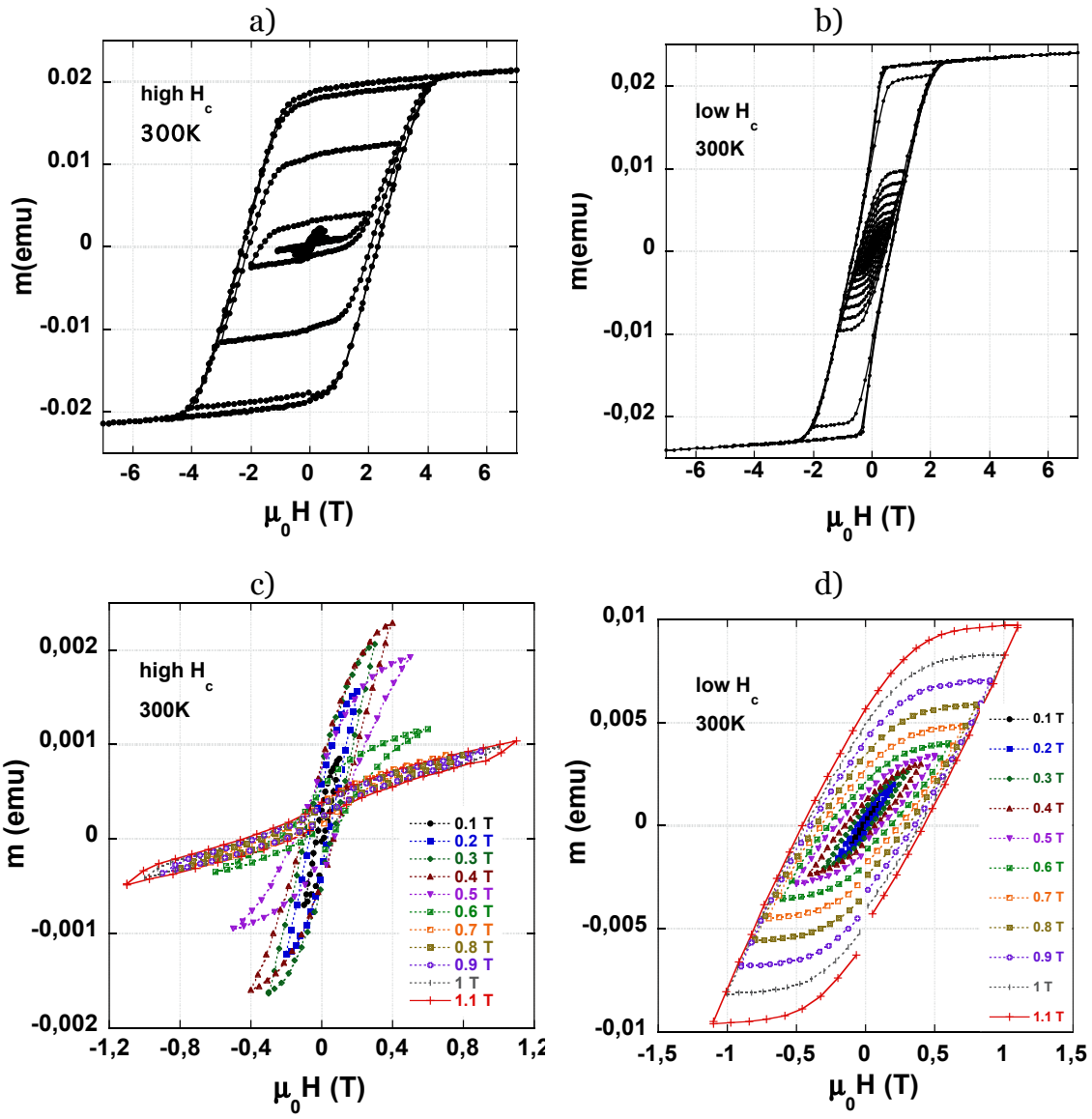

Fig. 4. 28 Experimental minor loops measured at 300 K, for high H_c((a) and (c)) and low H_c ((b) and (d)) thick films.

The applied field dependence of coercivity found in the two samples is very different. In the high H_c sample (**Fig. 4. 28**a and **Fig. 4. 28**c), the magnetization processes are essentially reversible up to 1.1 T. For higher applied fields, the coercivity develops and it reaches very quickly a value close to the one characterizing the whole sample. Note that the negative magnetization is smaller in magnitude (for fields smaller than 2 T) than the one obtained after application of the same, but positive field. This means that processes induced by the positive field do not occur in a negative field of the same amplitude.

Conversely, the evolution of coercivity in the low coercivity sample is progressive, from low field values up to maximum field. Furthermore, the hysteresis loops are symmetric for all field values, i.e. the magnetization $+M_{ra}$ obtained after applying $+H_a$ is equal to $-M_{ra}$ obtained after applying $-H_a$.

The results at 200 K are shown in **Fig. 4. 29** and the loops are similar to the ones measured at 300 K.

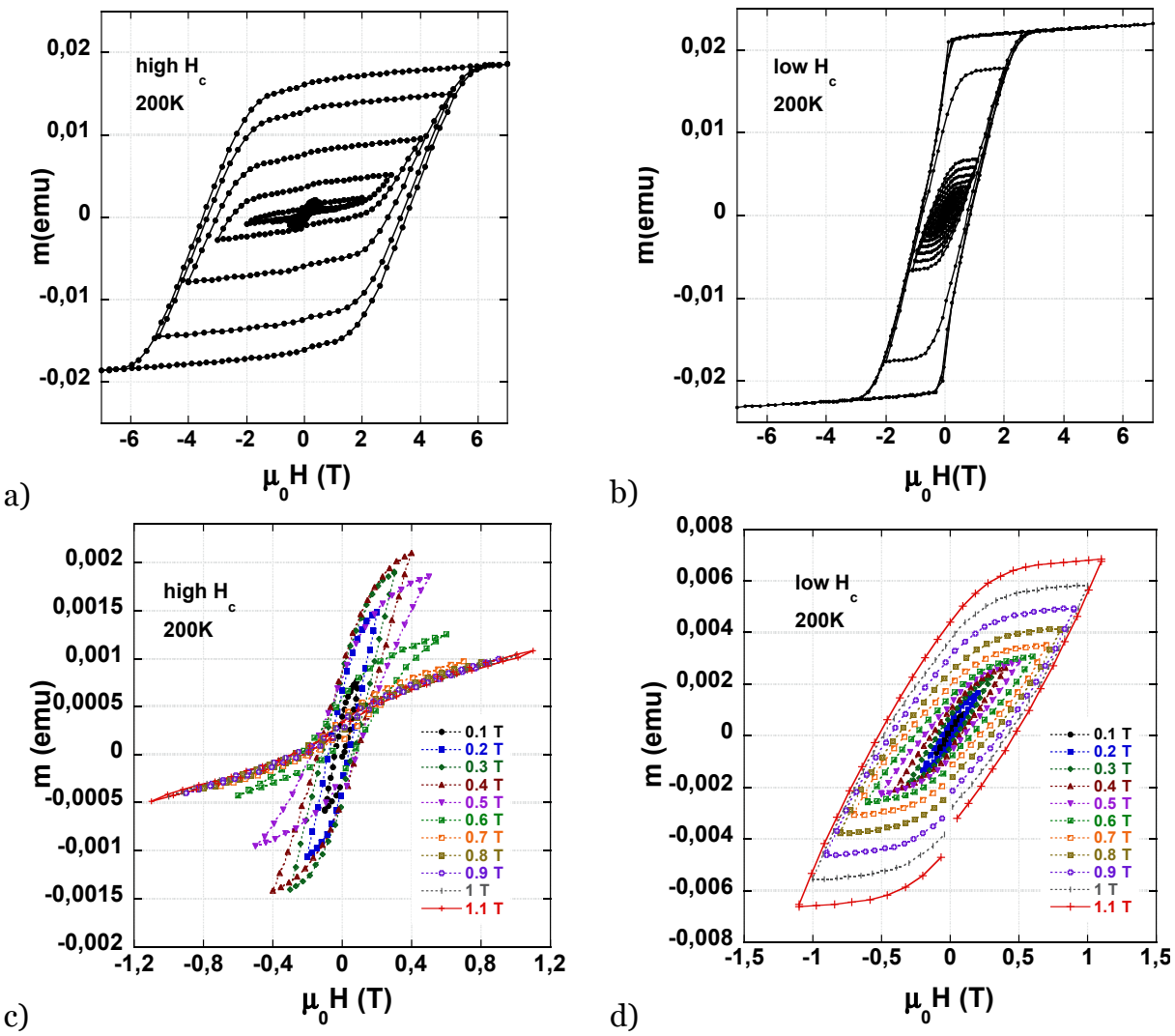

Fig. 4. 29 Experimental minor loops measured at 200 K, corresponding to the high H_c ((a) and (c)) and low H_c ((b) and (d)) thick films.

The coercive field as a function of the applied field is plotted in **Fig. 4. 30**a for the high H_c sample at 200 K and 300 K and **Fig. 4. 30**b for the second sample, at the same temperatures.

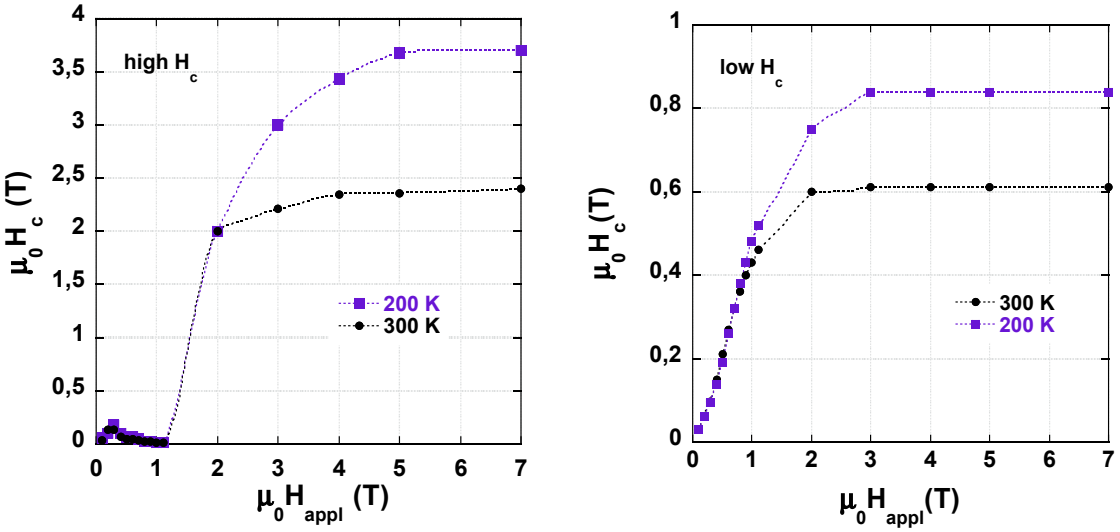

Fig. 4. 30 $H_c(H_{appl})$ for high H_c thick film at 300 K and 200 K (a) and low H_c thick film at the same two temperatures (b).

We propose the following interpretation of these results:

- high H_c thick film = mono and multi - domain grains which are essentially decoupled.

In the initial demagnetized state, both mono- and multi-domain grains are present. The reversible susceptibility measured for $H_{app} \leq 1.2$ T represents free domain wall motion in the multi-domain grains, i.e. there is no pinning in the bulk of the grains. As the field is increased above 1.2 T, the grains become single domain (or equivalently, the domain walls become very strongly pinned at grains boundaries). Once the grains are single domain, reversal requires that the applied field overcome the grain coercive field. One passes abruptly from low - coercivity reversible magnetization processes to high - coercivity irreversible processes.

The vertical shift of the minor loops is simply understood under such circumstances. It is obtained in the field range where a (relatively) low positive field of about 1 T has permitted to turn grains to single domains, but a negative field around 2 T (of the order of the H_c) is needed to reverse its magnetization.

This description of the "magnetic microstructure" of the high H_c is also consistent with MFM observations that are presented in the next chapter, chapter V, section V.3.1.

- low H_c thick film = magnetic domains encompassing many grains (Interaction domains)

The low H_c sample appears, on the contrary to the high H_c one, as being made of grains, between which exchange coupling cannot be neglected. In the initial magnetic state, magnetic domains exist encompassing several grains, in full agreement with MFM observations presented in chapter V, section V.3.1. The

microstructure seen by the domain wall is fundamentally heterogeneous and the domain walls are expected to occupy positions where their energy is lower. A distribution of energy barrier is expected to appear, thus explaining that irreversible processes are found already at low applied field of approximately 2 T.

[1] S. Heisz and G. Hilscher, JMMM 67, 20 (1987);

[2] D. Givord, H. S. Li and R. Perrier de la Bâthie, Solid State Comm. 51, 857 (1984);

[3] M. Sagawa, S. Fujimura, H. Yamamoto, Y. Matsuura and S. Hirosawa, J. Appl. Phys. 57, 4094 (1985);

[4] K. D. Durst and H. Krönmuller, JMMM 59, 86(1986);

[5] D. Givord, P. Tenaud and T. Viadieu, IEEE Trans. Magn. 24, 1921 (1988);

[6] D. W. Taylor, V. Villas-Boas, Q. Lu, M.F. Rossignol, F.P. Missell, D. Givord and S. Hirosawa, JMMM 130, 225 (1994);

[7] H. Krönmuller and K. D. Durst, JMMM 74, 291 (1988);

[8] D. Givord, P. Tenaud and T. Viadieu, JMMM 72, 247 (1988);

[9] G. Martinek and H. Krönmuller, JMMM 86, 177 (1990);

[10] F. Cebollada, M. F. Rossignol and D. Givord, Phys. Rev. B 52, 13522 (1995);

[11] A. N. Dobrynin, V.M.T.S Barthem and D. Givord, Appl. Phys. Lett. 95, 052511 (2009).

V. Analysis of magnetization reversal in NdFeB-based thick films using Magnetic Force Microscopy

The relationship between the microstructure and the mechanism of magnetization reversal is of great interest in permanent magnet research, as discussed in chapter II. In this chapter, this relation is studied experimentally, using magnetic force microscopy (MFM). It is the tool of choice for imaging magnetic domains since it can provide good spatial resolution (50 nm routinely)[1,2,3,4] under ambient conditions. What is more, no sample preparation is needed when imaging films if the surface is smooth enough.

The purpose of this study was to observe the evolution of the magnetic domain structure of NdFeB-based thick films with different microstructures (and thus different coercivities) with the applied field. The comparison of samples with different microstructures will help us to see (indirectly) how the microstructure influences the magnetic behavior of the materials. There have already been a number of reports on MFM studies of NdFeB. Gouteff et al.[5] and Woodcock et al.[6] studied films of NdFeB in the thermally demagnetized state. Magnetization of granular thin films deposited by PLD is reported by Neu et al.[7] who identified a nucleation type magnetization process in these films, that can be considered as an "assembly of small micron-sized, rectangular NdFeB single crystals"[8]. A complete study of magnetization and demagnetization of a die-upset NdFeB bulk magnet with in-situ applied magnetic field was reported recently by Thielsch et al[9].

Before presenting the study of domain structures of films in different states of magnetization, the choice of the tip will be discussed and specific features associated with MFM analysis of hard magnetic films will be reported.

V.1 Choice of the probe

The choice of the appropriate probe is an important step in MFM. Parameters such as the coercivity of the tip's magnetic coating and the cantilever stiffness have to be carefully chosen as a function of the sample to be imaged. One of the first papers reporting on the importance of the probe coating's coercivity is the one of Folks et al.[10].

MFM imaging consists in bringing very close together two magnetic materials – the sample on the one hand and the tip on the other hand. Naturally there will be a magnetic interaction between them. Depending on the strength of the interaction, three types of magnetic contrast may be considered[11]: charge, susceptibility or hysteresis contrast. While the last two situations correspond to reversible/irreversible changes in the magnetic structure of either the tip or the sample, in the first case, no such changes are registered. We aimed for this case, since the reduction of the number of variable parameters will ease the process of understanding. In the second and third cases, it can be difficult to make the difference between the information related to the sample and the information given by the interaction between the tip and the sample since the tip and/or the sample may change in an unpredictable way.

Considering that we want to image permanent magnets with coercive field larger than 0.2T (typically much higher), the probability of the magnetic domain structure of the sample being altered by the magnetic field produced by an MFM tip (of the order of mT[12]) is very small, and may be considered negligible. However, the stray field arising from our samples, at the distances where the MFM is typically performed, has significant values (of the order of 1T)[13]. We can conclude that the tip cannot alter magnetically the sample but depending on the coercivity of the magnetic material covering the tip, the sample may modify the tip. Three types of probes were assessed, their characteristics are listed in **Table 5. 1**. "Flexible cantilever soft coating" and "flexible cantilever hard coating" are standard MFM probes from Nanosensors having a spring constant of 2.8N/m and being covered with a magnetic material with coercivity around 0.03T and 0.5T respectively. "Stiff cantilever hard coating" are customized probes provided by Asylum, with a higher cantilever spring constant (42N/m) and coated with a $\mu_0 H_c$=0.5 T magnetic material.

	"Flexible cantilever soft coating"	**"Flexible cantilever hard coating"**	**" Stiff cantilever hard coating"**
coating	$Co_{80}Cr_{20}$	hard magnetic material	hard magnetic material
$\mu_0 H_c$ (T)	0.03	>0.5	>0.5
Tip radius (nm)	<50	<50	<50
Cantilever width/length/thickness (μm)	28/225/3	28/225/3	50/160/4.6
k(N/m)	2.8	2.8	42
Res. Freq.(kHz)	75	75	300

Table 5. 1 Comparison of the characteristics of "flexible cantilever soft coating", "flexible cantilever hard coating" and "stiff cantilever hard coating" MFM probes.

Test experiments showed that the stiff cantilever probes with high coercivity coating were best suited to our needs for the following reasons:

First of all, when using flexible soft tips, magnetization reversal of the tip was observed and detected at different locations depending on the scan direction. This is illustrated in **Fig. 5. 1** where the two images were obtained for the same scan, the first one when the tip went from left to right (forward) and the second one when the tip returned (backward). The second scan allows checking for instabilities in the system.

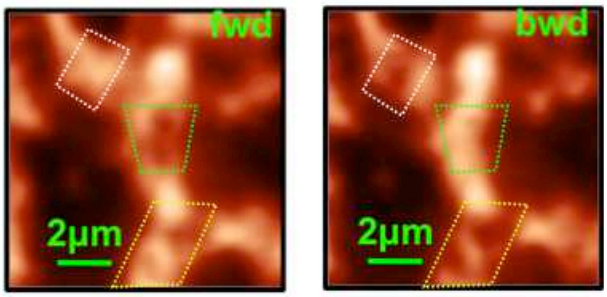

Fig. 5. 1 In plane forward (left) - backward (right) MFM images of a thermally demagnetized NdFeB film taken with a "flexible cantilever soft coating" probe.

Secondly, the influence of the cantilever stiffness was studied. Imaging electric or magnetic forces with an amplitude modulation technique requires a compromise between a cantilever stiff enough to image reliably the topography while avoiding sticking of the probe to the surface during the second pass. However, it has to be flexible enough to allow for a reasonable signal over noise ratio. Typically, cantilever stiffness is in the range 1-4 N/m and resonance frequency between 50 and 100 kHz.

Fig. 5. 2 shows topographic (a and b) and magnetic images (e) of a thermally demagnetized NdFeB film. The "flexible cantilever hard coating" (see **Table 5. 1**) probe was used. The force between the tip and the sample is so large that the phase shift often exceeds $\pm\pi/4$, which is detrimental for the imaging. The phase shift could be converted to the frequency shift to recover the linearity with the sensed force but the change of amplitude of oscillation due to the shift of resonance angular frequency changes the probing range and resolution depending on the value of the force. In principle, this effect could be corrected with a feedback on the amplitude during the second step.

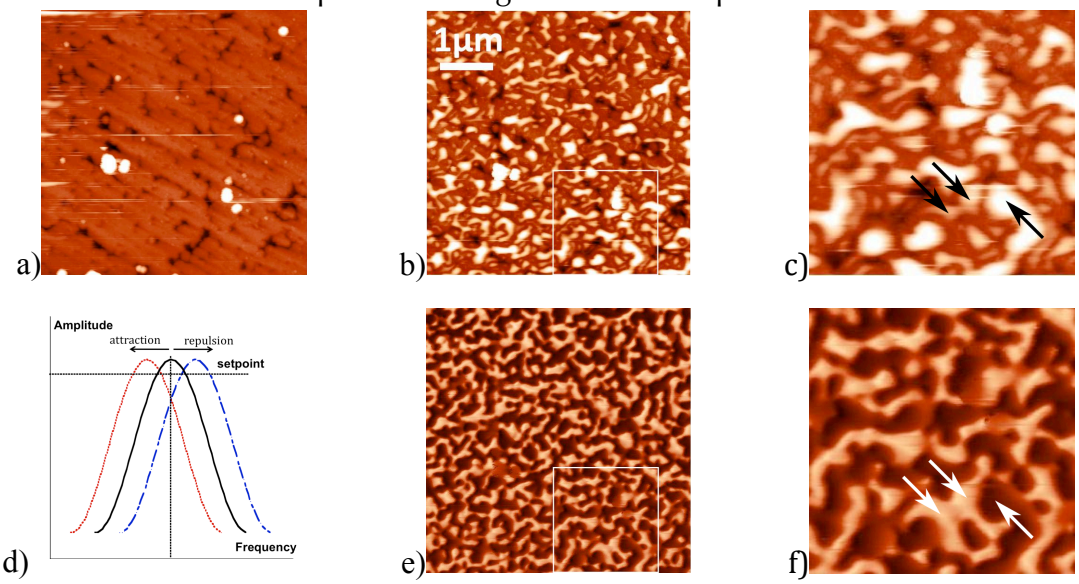

Fig. 5. 2 Topographic **(a)**, **(b)** and corresponding second pass phase **(e)** imaging with flexible cantilever hard coating MFM probes, under hard tapping **(a)** and soft tapping **(b)** conditions; zoom in of the white squares from (b) and (e), **(c), (d)**; Downward (resp. upward) arrows highlight regions with repulsive (resp. attractive) forces. The excitation frequency was set slightly higher than the resonance frequency, resulting in a greater sensitivity to repulsive than attractive forces in creating artifacts; sketch of the resonance peak shift due to attractive (short red dots) or repulsive (long blue dots) forces **(d)**.

The second problem is that, when performed in a light tapping mode (setpoint about 1% lower than the free amplitude), topographic images display artifacts due to the spontaneous lifting of the tip from the surface, **Fig. 5. 2**b. In the case of indifferently repulsive or attractive strong forces, the shift of resonance frequency results in a decrease of the cantilevers' amplitude of vibration (**Fig. 5. 2**d). This decrease is wrongly interpreted by the feedback loop as an increased tapping interaction with the surface. The tip is thus retracted to recover the high amplitude. So, if the value of the amplitude becomes smaller than the setpoint, the tip will be lifted from the surface. This happens for both attractive and repulsive forces, as the arrows in **Fig. 5. 2**c and **Fig. 5. 2**f indicate.

These artifacts may be avoided by setting an amplitude setpoint well below the free oscillation value. This results in stronger interaction between the tip and sample and it may accelerate the abrasion of the magnetic material of the tip.

These drawbacks can be overcome through the use of much thinner magnetic coatings but the desired coercivity may be difficult to achieve. For all these reasons, we made the choice for our MFM studies of a type of tip based on a stiff cantilever and a hard magnetic coating. Phase shifts are then of a few degrees at maximum, which is clearly in the linear range. The magnetic coating composition and thickness remain unchanged.

V.2 Phase contrast in MFM images of thick hard magnetic films

To understand some specific features that we observed while imaging thick hard magnetic films, model systems with magnetic domain patterns of known size and shape were prepared. Analysis of the MFM images of such model systems will now be presented.

As shown in Annex 1, in MFM the information about the magnetic force F_{ts} between tip and sample is mapped as the phase shift induced on the cantilever when excited at its natural resonant frequency, eq. A.1.4. This phase shift is proportional to the force's derivative along the direction of vibration and also to the quality factor and spring constant characterizing the cantilever. The difficulty of the analysis of magnetic contrast arises when trying to model the force. Seen from two equivalent points of view, this force can represent the force exerted on the tip's magnetization by the magnetic field arising from the sample or the force exerted on the samples' magnetization by the field arising from the tip. Either way, simplifying assumptions on the tip and sample are needed. We restrict our discussion to the case of a perfectly rigid sample and tip magnetization. This assumption is valid in the case of samples considered in our study, as it was shown in V.1. We model the tip-sample interaction using the most common approximation found in literature, the point probe approximation[14]. The mathematical modeling for this case is presented in Annex 2. Within this model, the entire magnetic coating of the probe is approximated with a magnetic monopole or dipole located at one point within the probe, at a distance d from the tip's apex, like in **Fig. 5. 3**.

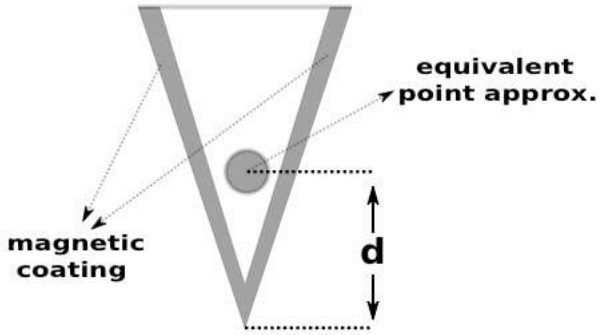

Fig. 5. 3 Scheme of the point probe approximation; the magnetic coating of the tip is replaced by a point mono/dipole located at a distance d along the probe's axis.

The simple multiplication of the monopole charge by the first derivative of the sample's stray field or of the magnetic dipole moment with the second derivative of the stray field will give the actual MFM signal (i.e. the phase shift). Based on MFM measurements at various heights in the well-controlled magnetic field produced by current rings, it was concluded that both models could account for the experimental data. The magnetic charge for a monopole and magnetic moment for a dipole, as well as their imaginary position on the tip's axis were determined by few groups[15,16].

We followed the procedure of the above groups, i.e. mapping of the phase shift at various lift heights and compare experimental with theoretical results. For

that, we needed samples of well-controlled magnetic structure for which we could calculate the field and its derivatives. Thermo-Magnetic-Patterning (TMP)[17] was used to obtain "model" micromagnets from continuous hard magnetic films. Using this process, the direction of magnetization can be imposed by laser beam heating. First, the entire film is saturated along a direction perpendicular to its surface. Then it is irradiated, through a mask, with a laser beam. The heated areas will experience a drop in coercivity and their magnetization may be reversed with the aid of a relatively small external field applied opposite to the films direction of magnetization. If the coercivity of the sample at room temperature is much higher than the applied field, the magnetization of the matrix remains unchanged. Thus, micromagnets with perpendicular magnetization in a matrix uniformly magnetized in the opposite direction are obtained. For this particular study, a TEM grid was used as a mask to produce an array of micromagnets of surface 7X7μm^2 separated by a distance of 10μm, with an estimated depth of around 1μm[17]. Because of the presence of ripples on the surface of high H_c NdFeB films (see Annex 6), SmCo hard magnetic films were used to produce these model systems.

The calculation of the stray field and gradients for this type of structure was done using the model described in Annex 5. For the experiments, the stiff cantilevers with hard magnetic coating, magnetized prior to imaging in a field of 8T, were used. We assume, at first, that z is the direction normal to the sample's surface and that the magnetic material capping the tip is magnetized along z on average and the vibration direction is also z. The experimental results are therefore compared with the vertical component of the stray field and its space derivatives along the same direction.

In **Fig. 5. 4** a, experimental scan lines above a set of three micromagnets, for 4 different scan heights: 0.005, 0.5, 1 and 2.5 μm are displayed. For comparison, the calculated z- field (**Fig. 5. 4** b), z-field's first derivative (**Fig. 5. 4** c) and z-field's second derivative (**Fig. 5. 4** d) for the same heights, are shown.

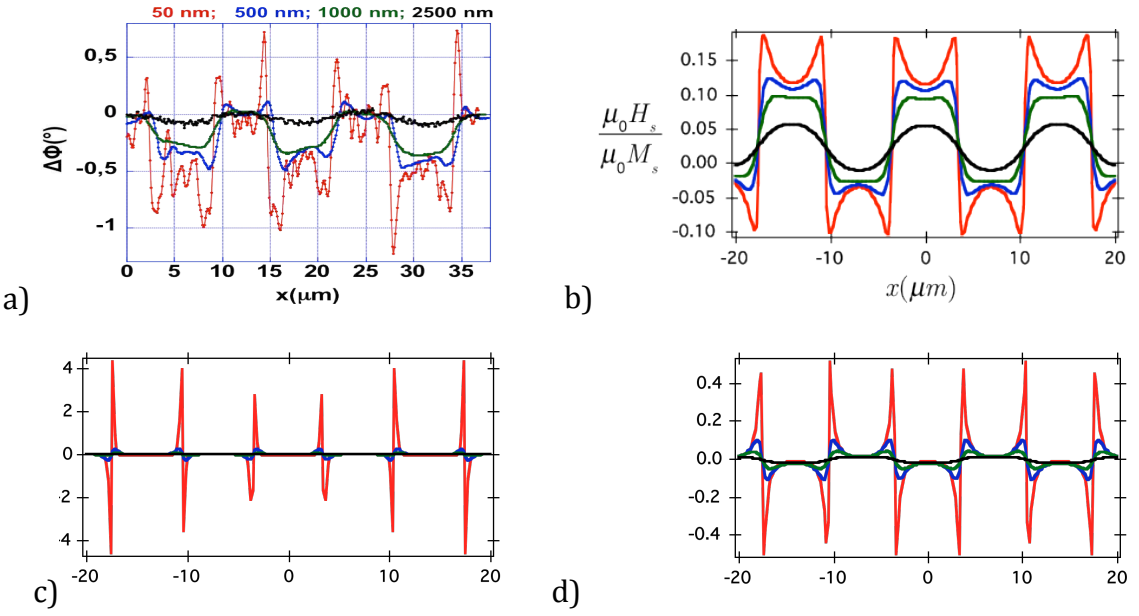

Fig. 5. 4 Experimental scan lines of the phase shift at different scan heights (a) compared to calculated vertical field (b), its first derivative (c) and its second derivative (d) along z.

The z-scale in **Fig. 5. 4** cannot be compared since for the experimental lines, the phase shift is given (unit: deg) while for the calculation, the field (induction units) is plotted.

Note that:

a) films are protected with 100nm Ta which is not removed when MFM is performed. The Ta layer is considered in the calculation of the stray field.

b) each experimental line scan in fig. 5.4a represents an average made over 50 real line scans.

Both experiments and theory show that the contrast consists of two contributions: one contribution is essentially uniform above the μ-magnets and the matrix, the other varying sharply at the edges of the μ-magnets. Later on, the first contribution will be considered in more detail and it will be observed that experimentally it changes with the lift height, due to the granular nature of the films, but for the moment this aspect is not important.

By looking at the 4 graphs in **Fig. 5. 4**, it is clear that the experimental contrast is best reproduced by the map of the stray field itself. The calculated derivatives are decaying much faster with height than the experimental data. The second derivative is the least convincing. This finding is in contradiction with previous reports from literature[12,16,18,19,20]. Mapping the stray field is predicted for a tip modeled by a cone capped with magnetic material of uniform thickness as shown in Annex 2. While this is theoretically the case, in practice, the situation is different. Most of the samples measured by MFM produces short-range stray fields. This implies that only a small part of the magnetic tip is active during the imaging and the monopole and/or dipole models are more appropriate to be used. This effect is amplified by the finite radius of curvature of the tip apex combined with the typically normal incident deposition of magnetic material, resulting in a larger thickness of material at the apex than on the sides of the tip.

The phase shift reflecting the stray field itself, rather than one of its derivatives, is therefore an aspect specific to permanent magnets with potentially long-range stray fields.

Let's have a look now at the 2D phase maps. **Fig. 5. 5**a shows the calculated stray field above a 3X3 μ–magnet array. Four-fold symmetry with dark-light contrast on all four sides of each prism can be observed.

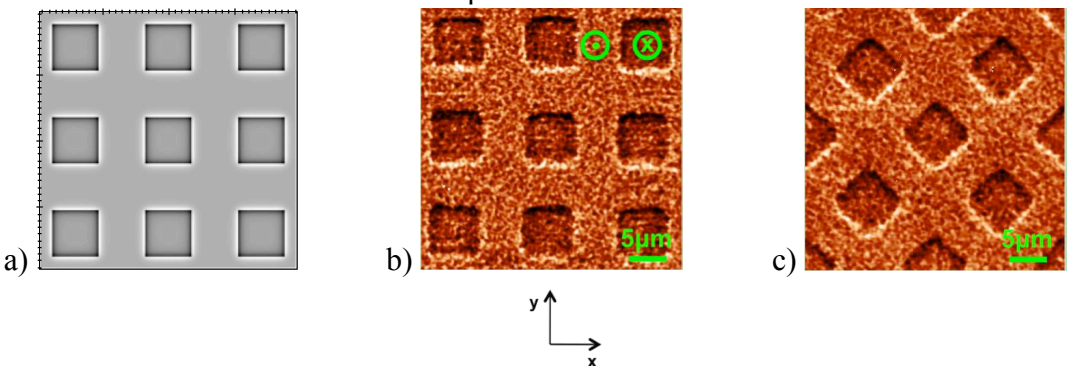

Fig. 5. 5 Calculated 2D stray field map (a) compared to experimental phase shift map (b) and experimental map after a 45 deg rotation of the sample (c).

In the experiment, **Fig. 5. 5**b, the behavior is different, an obvious difference between x and y directions being observed. This asymmetry does not depend on the choice of the fast and slow scan directions. It can have several origins, related to the sample, probe or both, as will now be discussed.

First, if the μ-magnets are not completely out of plane oriented (if the field is not perfectly aligned during patterning), the in plane component of the magnetization could give this kind of behavior. To test this, MFM imaging was done after rotating the sample by different angles. The symmetry of the black-white contrast does not change (i.e. the direction of alternation remains vertical), as can be seen for example in **Fig. 5. 5**c, where the sample was rotated through 45 degrees. If there was an in-plane sample magnetization, the direction of alternation should rotate with the sample, as it does in **Fig. 5. 6**. In this case, the TMP was done on purpose with the magnetization in-plane and the above experiment was repeated. Thus the asymmetry observed in **Fig. 5. 5** can not be due to an in-plane component of the μ–magnets' magnetization.

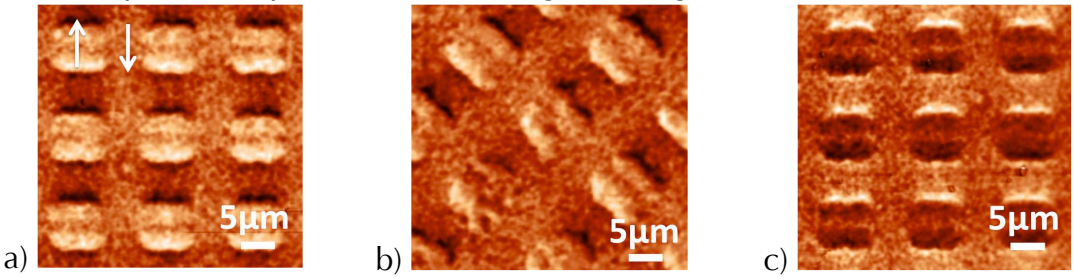

Fig. 5. 6 MFM images for a matrix of in-plane micromagnets at 0 deg (a); after rotating the sample 45 deg (b) and 180 deg (c).

Asymmetric signals due to the probe were already reported by Rugar et al.[21]. A first effect is related to a potential in-plane component of the tip magnetization. In this case, the component of the stray field from the sample, that is parallel to the in-plane magnetization of the tip, will be revealed during imaging. This can not be the case here, since the alternation was always observed along the same direction.

Another probe related effect comes from the fact that in most microscopes the cantilever does not oscillate exactly in the z direction, as we assumed in the beginning. Because of space restraints, the oscillation direction makes always an angle with the normal to the sample, **Fig. 5. 7**.

In the general formalism (see Annex 2) this brings both: i) sensitivity to an in plane component of the stray field, as part of the moment of the tip is in the plane of the sample (even though it may be aligned along the axis of the tip) and ii) the y gradient of the force. The second term does not count for us, since we are sensitive directly to the field.

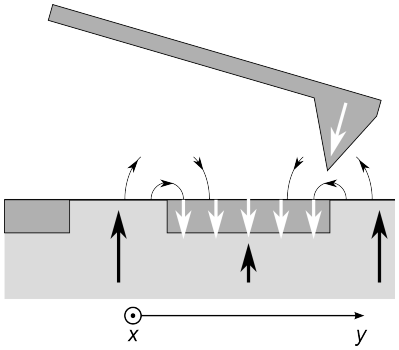

Fig. 5. 7 Schematic of the real tip-sample geometry during scanning.

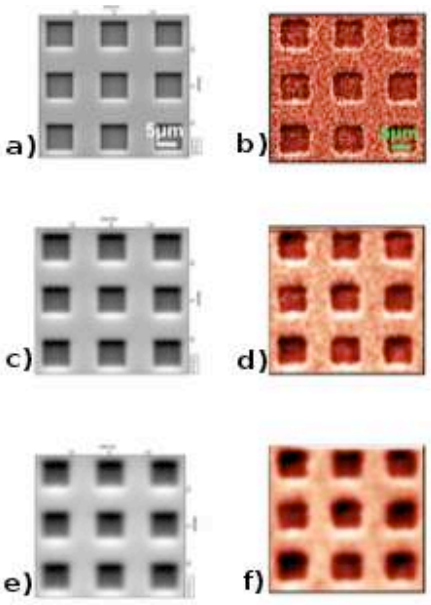

Fig. 5. 8 Calculated $H_z\cos\beta-H_y\sin\beta$ (a,c,e) with β =15 deg and experimental maps (b, d, e) registered at 50, 500 and 1000nm respectively.

Thus, for a tilt angle β, not just the z-component of the stray field should be considered but rather $H_z\cos\beta-H_y\sin\beta$. The result of the calculation, for β =15 deg is shown in **Fig. 5. 8** a), c) and e) for three different lift heights: 50 nm, 500 nm and 1000 nm. The value of the angle was estimated on the basis of a photo of the MFM microscope used. The experimental maps taken at the same distances from the sample as considered in the calculations are shown in parallel(**Fig. 5. 8** b), d) and f). A good agreement of the experiment with the calculation can be observed at all the heights as far as the coarse magnetic features are concerned. At low lift heights a second type of contrast is observed in the experiment, in both the reversed and non-reversed regions. This fine magnetic contrast is attributed to the granular nature of the films. When very close to the sample, the MFM probe is sensitive to the local stray field arising from individual grains. This field decays fast with distance, considering the grain size (30-40 nm in this case) and it is not observed at bigger scanning heights.

Observation: the here-described asymmetry appears only in the case of tips with hard magnetic coating. In the case of "flexible cantilever soft coating" probes, the map is completely symmetric and the contrast above the micro-magnets is always dark which is indicative of attractive forces, see **Fig. 5. 9** a). The direction of magnetization of these tips is controlled by the stray field arising from the sample, due to the small coercivity of their magnetic coating.

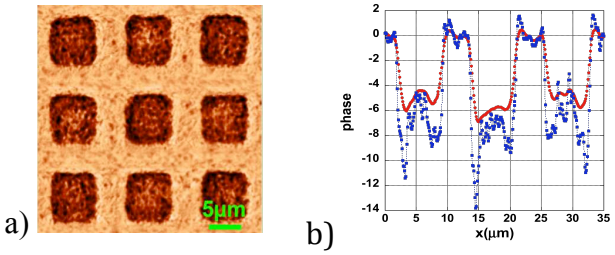

Fig. 5. 9 MFM map of a matrix of 3X3 SmCo µ-magnets imaged with a "flexible cantilever soft coating" probe (a) and scan lines corresponding to the same sample as (a) at two scan heights, (b).

Fig. 5. 9 b) presents two line scans above the µ-magnets, for two different scan heights. These scans clearly show the always-negative signal above the µ-magnets and also the close to zero signal in between the isolated µ-magnets, i.e. above the matrix. This is due to the fact that the surface area ratio between the part of the film that was not reversed (matrix) and the reversed µ-magnets remains

sufficiently large so that the non-reversed part behaves like an infinite saturated continuous film that produces no stray field.

A calculated stray field map is shown again in **Fig. 5. 10** a) with the z-scale this time. By comparison, another geometry, where the surface ratio between up and down areas is 1 was considered in **Fig. 5. 10** b). It can be seen that, in this case, the signal varies from +0.3 to -0.3 while in the first case, in between the micromagnets we are close to zero.

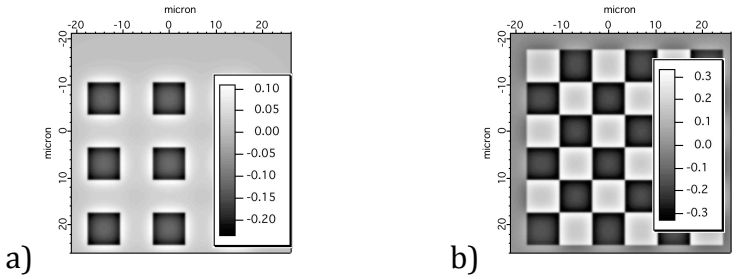

Fig. 5. 10 Calculated z-component stray field for two geometries, corresponding to two values of the "up" and "down" ratio.

Conclusions:

a) MFM imaging of permanent magnets – the stray field is mapped when coarse magnetic domains with long-range stray fields are imaged;

b) cantilever tilt – explains asymmetric contrast at edges of domains in the case of probes with hard magnetic coatings.

This study of model μ-magnets served in the interpretation of magnetization reversal in NdFeB films studied by MFM imaging – see Section V.3.

V.3 Magnetization reversal in NdFeB thick films

NdFeB-based thick films ($t \sim 5\mu m$) with different microstructures and thus different coercivities were prepared by triode sputtering. The variation in microstructure can be achieved by varying the parameters during preparation[22]. In **Table 5. 2** are listed the samples that were analyzed by MFM and chosen to be discussed in this section. The first column in the table represents the given name for each sample in the form S_x, with x being the value of the coercive field at room temperature, a value given also in the second column. All films have grains elongated in the out-of-plane direction. In the case that the individual grains traverse the entire film, we name them columnar films.

Sample	$\mu_0 H_c$(T)	Grain type	State
$S_{0.2}$	0.2	elongated	continuous
$S_{0.7}$	0.7	elongated	continuous
$S_{1.2}$	1.2	columnar	patterned
$S_{2.55}$	2.55	elongated	continuous
$S_{2.6}$	2.6	elongated	patterned

Table 5. 2 List of NdFeB samples for which magnetization reversal was analyzed by MFM.

Two types of samples were imaged: continuous films (i.e. non-patterned) and thermo magnetically patterned films. The TMP process of patterning was already described in section V.2.

The patterned films were studied on the basis that the demagnetization of an object could be observed while the surroundings stay unchanged and they could thus be used as reference. As shown schematically in **Fig. 5. 11**b, one single object, in this case a micro-cylinder, was "printed". The result is an object with magnetization in one direction (M_{up}) within a magnetic material magnetized in the opposite direction (M_{down}). A magnetic field applied in the same direction as M_{down} will demagnetize the material inside the cylinder and will leave the matrix unchanged. The matrix can thus be used as a reference during demagnetization of the micro-object.

a) b)

Fig. 5. 11 Schemes of the two types of magnetic surfaces that were imaged: continuous (i.e. non-patterned) film (a) and TMP film (b).

A limitation in using thermo magnetically patterned samples is that the starting point is always a saturated state so that only the demagnetization process can be studied while our interest is in both magnetization and demagnetization.

V.3.1 Role of the intergranular phase ($S_{2.55}$ vs. $S_{0.7}$)

To begin, the results obtained for two oop-textured samples, $S_{0.7}$ and $S_{2.55}$, will be presented. These samples are part of the same deposit but taken from different positions on the substrate. Due to the relatively large size of the substrate (Si/SiO_2 wafer of 10cm in diameter) and that of the target, the Nd/Fe content varies across the wafer. Considering the results obtained from SEM, TEM, 3DAP, VSM and XRD measurements of the two samples (see Annex 7), we tentatively attribute the difference in coercivity to magnetic decoupling of the grains[23]. MFM is used to test experimentally this assumption.

V.3.1.1 Magnetization

The first MFM images presented here, **Fig. 5. 12** a) and **Fig. 5. 12** b**,** correspond to thermally demagnetized states of the low and high H_c samples, respectively. The magnetic structure is similar, the width of the features observed being in the same size range as the width of the grains. The domains in the low coercivity sample are slightly elongated and bigger than the ones in the high coercivity film.

A magnetic field was applied perpendicular to the sample's surface and its value was increased step by step. After each field application, the field was reduced to zero and the sample was imaged in the corresponding remanent magnetic state. The red points in **Fig. 5. 13** indicate the corresponding remanent magnetic states, for both samples (the curves were measured with the VSM).

Successive MFM images were made on the same part (10X10μm) of the film and the results are shown in **Fig. 5. 12**. The bright domains in the images correspond to those magnetic domains in the sample that are oriented in the same direction as the applied external field and the black ones correspond to oppositely magnetized domains.

The first steps of magnetization do not show big differences between the samples. For applied magnetic fields smaller than 1T for $S_{0.7}$ and 0.7T for $S_{2.55}$, the size of the observed features does not change significantly. This behavior is attributed to the fact that the magnetization processes in this field range are mainly reversible events (free magnetic domain wall movement) as could actually be directly derived from the first magnetization curve (**Fig. 5. 13**). Upon application of the magnetic field, the magnetic domain walls are moved so that the magnetization in the field direction increases. Once the field is removed, the walls can either move back or be pinned in some more energetically favorable positions, depending on the value of the applied field and the microstructure of the sample. The "remanent" state corresponding to each value of the applied field depends on how much "freedom" to move the domain walls have. In higher fields, the magnetic structure changes significantly: i) for the same sample with increasing field but also ii) from one sample to the other.

In the case of $S_{0.7}$, the low H_c sample, large magnetic domains corresponding to the direction of the applied field ("white") separated by smaller oppositely magnetized domains ("black") can be observed when fields superior to 2T are applied, **Fig. 5. 12**g, **Fig. 5. 12**i and **Fig. 5. 12k**. The white domains can have lengths and widths of a few micrometers while the black ones are more

elongated, with widths of maximum 2μm and lengths of a few micrometers. The domain dimensions are significantly bigger than the width of the grains (100-150 nm from SEM images) indicating magnetic coupling between grains(i.e. the formation of interaction domains). The area of white domains reaches a plateau for an applied field of 2.3T. Each time the sample sees a field bigger than 2.3T, the magnetic domains reorganize. The shape and size of the domains vary but the ratio between up and down domains is similar. The three images just mentioned have been binarized (**Fig.5.19bis**). The calculation of the ratio of white surface to total surface gave 67.5% for 2.3 T applied field, 68 % for 4T and 74% for 8T.

The high coercivity film presents a magnetic structure that is more granular-like for all values of the applied field (**Fig. 5. 12**, right column). The smallest feature size is comparable to the grain width (200-250 nm for this sample). The spatial extent of magnetic coupling in this sample is much reduced, compared with the low coercivity sample. This is consistent with a better magnetic decoupling of the grains due to the presence of a continuous non-magnetic grain boundary phase.

Several aspects of the MFM images made following the application of the maximum applied field, for the two samples, are considered further:

*low H_c sample (**Fig. 5. 12** k):

- the presence of big reversed domains;
- the appearance of strong black and white contrast at the edges of the big saturated domains.

* high H_c sample (**Fig. 5. 12**l): granular contrast.

The presence of reversed domains in the low H_c sample after applying even 8T can be interpreted in the following manner: the self demagnetizing field alone is sufficient to induce nucleation at some low anisotropy defect points. Because the grains are magnetically coupled between them (as the presence of big magnetic domains indicate), big areas can be involved in the reversal and they form the big black domains seen in the remanent state, even after saturation under 8T. The reduced value of remanent magnetization, after applying 8T, measured in the VSM is in agreement with this.

The second point related to the low H_c sample, the edge black-white contrast is due to the tilt of the probe during MFM imaging – discussed in section V.2.

To understand the granular contrast specific to the high H_c film, the comparison between the two samples becomes important. Let's consider a small part (white square indicated in **Fig. 5. 12**k) of a saturated white domain in the low coercivity sample (**Fig. 5. 14**a) and a similar sized part (white square in **Fig. 5. 12**l) of the high coercivity one (**Fig. 5. 14**b). The z-scale shows that the actual interaction between the sample and the tip – the phase shift in this case - is of the same order of magnitude. Two line scans, corresponding to the two samples are displayed for comparison in **Fig. 5. 14**c. Moreover, if the two line scans are compared to one that corresponds to a transition from up to down domains in the low coercivity sample (white dotted line **Fig. 5. 12**k), it can be seen that the interaction is one order of magnitude higher. These three line scans are presented together in **Fig. 5. 14d.**

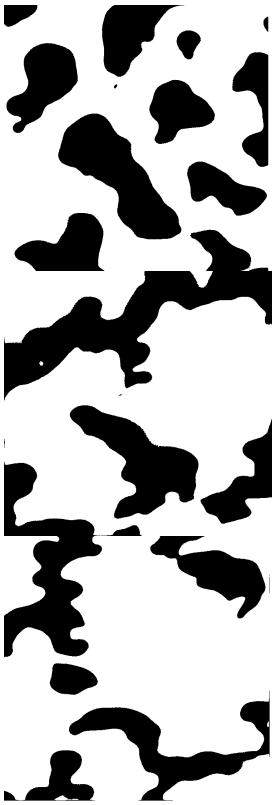

Fig.5.12bis
Binarization of the last three MFM images corresponding to $S_{0.7}$.

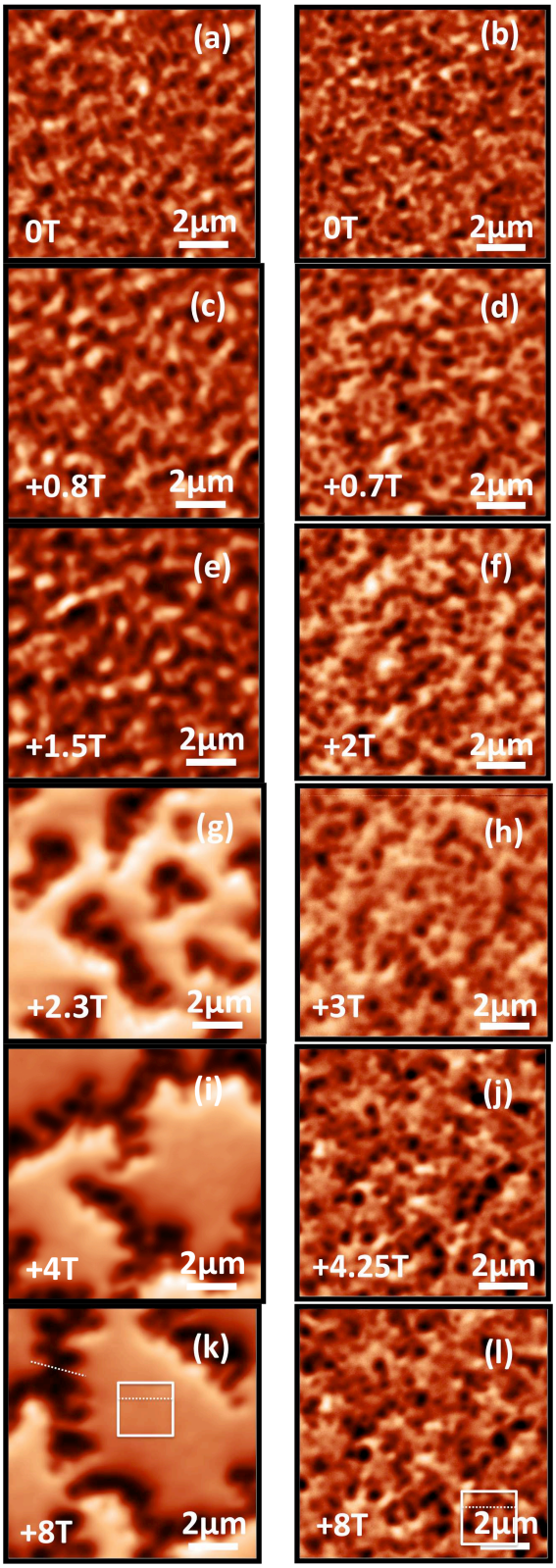

Fig. 5. 12 MFM images corresponding to different remanent magnetic states on the magnetization curve for $S_{0.7}$(left column) and $S_{2.55}$(right column).

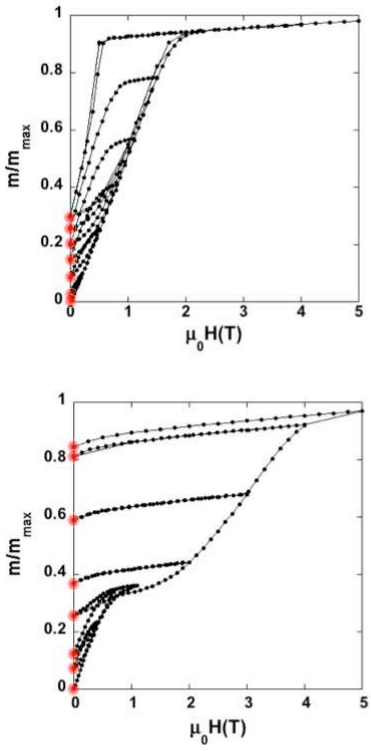

Fig. 5. 13 VSM magnetization step by step for $S_{0.7}$ and $S_{2.55}$. Red points mark the magnetic states corresponding to the MFM images shown in **Fig. 5. 12**.

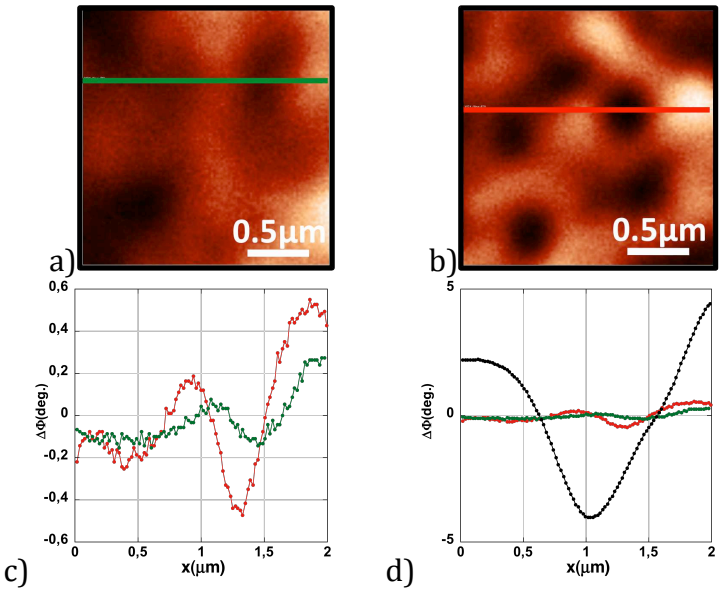

Fig. 5. 14 cuts from **Fig. 5. 12**k and **Fig. 5. 12**l (a and b)

Scan lines corresponding to the two images (c) and the two images + an up-down transition (d).

This analysis shows that the granular structure, clearly evident in the high coercivity sample, is also present in the "saturated" regions of the low coercivity sample but it does not appear as obviously because of the one-order of magnitude higher signal contrast present in the same image, at the transition from an up-domain to a down-domain. This suggests that the small black domains present in the high H_c sample are not an indication of reversed domains but rather a reflection of local variations in grain texture, which are detected because of the tilt of the probe. This may also explain the M/M_{max} value of 0.85 seen in the VSM measurement. In addition to this, some reversed domains (on the scale of the grain size) may be present as well.

V.3.1.2 Demagnetization

The demagnetization process was also followed with the MFM. Imaging was done in remanent states, as in the previous case, but the direction of the field was inverted. The red points in **Fig. 5. 15**a and **Fig. 5. 15**b indicate the remanent magnetic states that were imaged for the low and high H_c samples, respectively.

Representative images are shown in **Fig. 5. 16**. Starting from the remanent state in maximum applied field in a positive direction going towards maximum field in the negative direction, the domain configuration evolution followed by the two samples is distinct.

For the low coercivity sample (column 1 and 3 in **Fig. 5. 16**), the domains that are already in the direction of the field increase constantly with the applied field. The MFM image taken after applying -8T (**Fig. 5. 16**o) is similar to the one registered after +8T (**Fig. 5. 16**a), consisting of big domains oriented with the field (black) plus reversed elongated domains (white).

For the high H_c sample (column 2 and 4 in **Fig. 5. 16**), the reversal proceeds in a different manner. In the beginning, small reversed nuclei (a few grains wide) form in different parts of the sample. When the field is increased two things happen: i) formation of new reversed zones and ii) a slight increase in the size of the already existing nuclei. This is evidence for the already-mentioned magnetic decoupling of the grains in these samples.

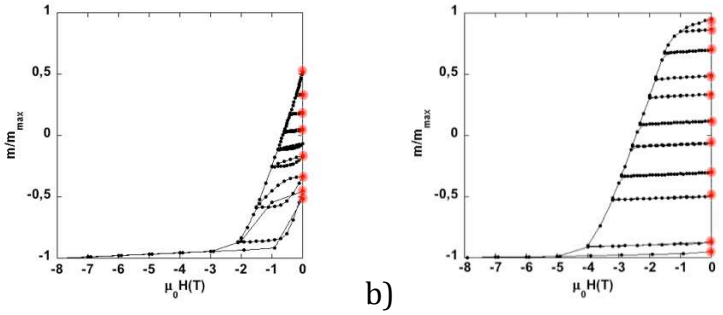

Fig. 5. 15 VSM recoil loops for $S_{0.7}$ (a) and $S_{2.55}$(b); red points indicate the magnetic states that were MFM imaged.

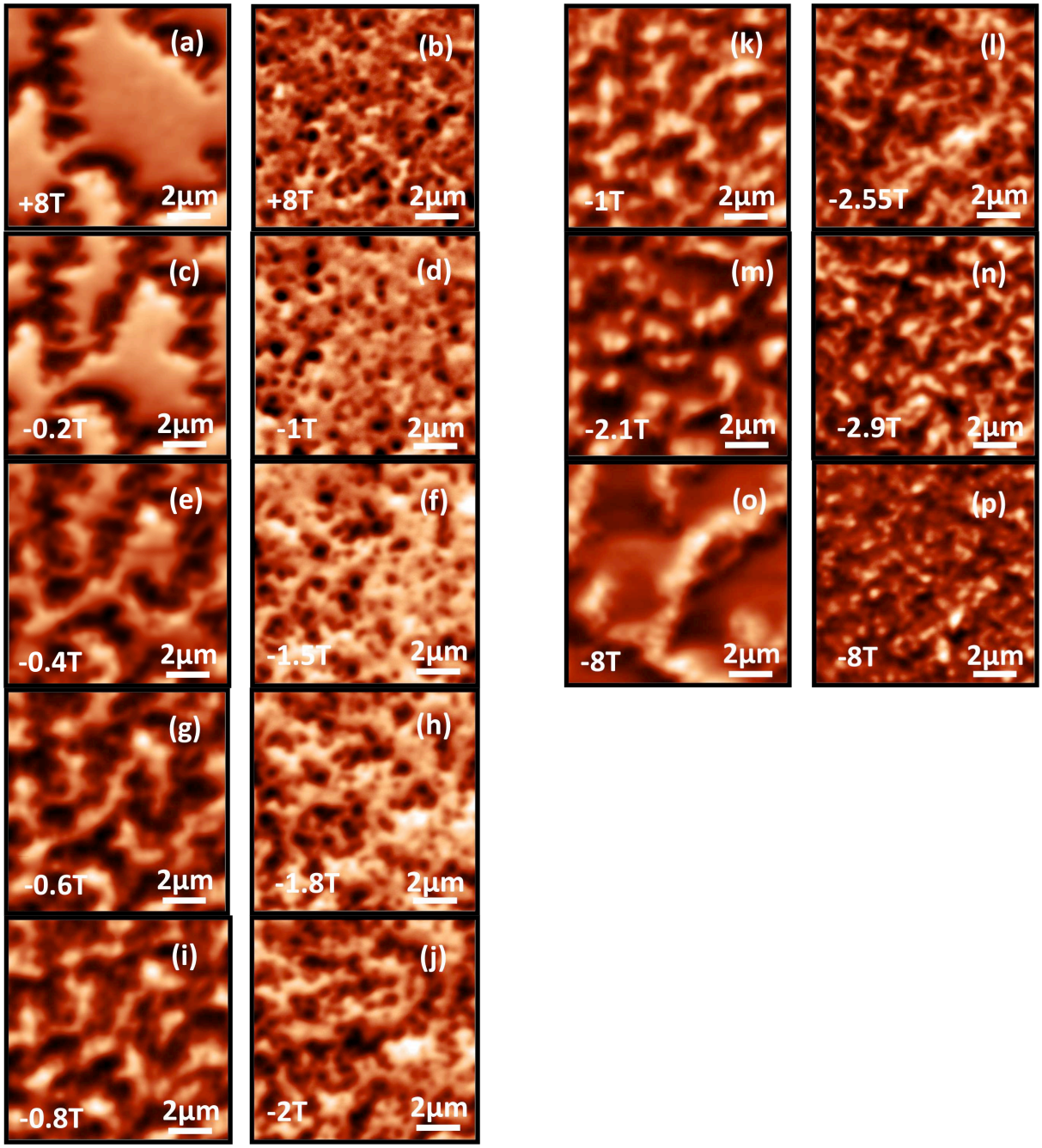

Fig. 5. 16 MFM demagnetization maps for low ($S_{0.7}$) / high ($S_{2.55}$) coercivity NdFeB film column 1 and 3 / column 2 and 4.

Comparing the images of the remanent states, after applying ±8T, is also instructive. The up-down images corresponding to the high coercive sample, **Fig. 5. 17**a and **Fig. 5. 17**c, are symmetrical, white becomes black and black becomes white. Different geometrical shapes are used to emphasize a few examples of features that just change sign from one image to the other.

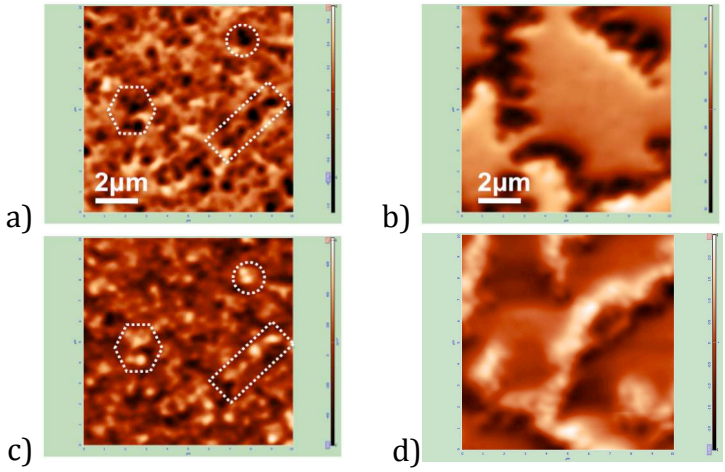

Fig. 5. 17 Comparison of magnetic states after applying +8T and -8T for high coercivity NdFeB film (a and c) and lower coercivity NdFeB film (b and d).

For the low coercivity sample, the two images (**Fig. 5. 17**b and **Fig. 5. 17**d) are not mirror images and energy minimization following the removal of the applied field is obtained for different arrangements of magnetic domains.

To conclude, if the results above are compared to the physical microstructure, we can say that in the demagnetized state, the two samples are similar with the domain size being comparable to a few grains. When a magnetic field is applied, large interaction domains form in the low coercivity sample while the behavior is much less collective in the high coercive sample, the size of domains being limited in space. There is still a certain degree of connectivity in the high coercive sample but much less than in the low coercive one.

V.3.2 Role of the grain shape/size ($S_{2.6}$ vs. $S_{1.2}$)

The two samples that were compared in the previous section have a microstructure characterized by grains that had a similar aspect ratio but very different intergranular structure due to a difference in Nd content. In this section, two samples with similar composition but very different grain shape/size will be compared. The first sample is a high coercivity one, with elongated grains (length/width ≅ 3-4) and is comparable to $S_{2.55}$ in V.3. The second sample, $S_{1.2}$ has a columnar grain structure as shown in **Fig. 5. 18**a, with the length of the columns equal to the film thickness and the width being around 200 nm (length/width ≅ 20). The coercive field of the two samples are 2.6T and 1.2T respectively. The $S_{2.6}$ ($S_{1.2}$) film was deposited by triode sputtering in two steps: deposition at 450°C (500°C) and annealing at 700°C for 10 min.

In this case, the MFM study was performed on 20µm diameter TMP single objects, hence only the demagnetization was studied. In **Fig. 5. 18**b VSM recoil loops (measured after MFM) are presented for the columnar sample. The red points indicate the remanent states corresponding to the MFM images that will be shown. For the high coercivity one, the curves shown in **Fig. 5. 15**b may be considered.

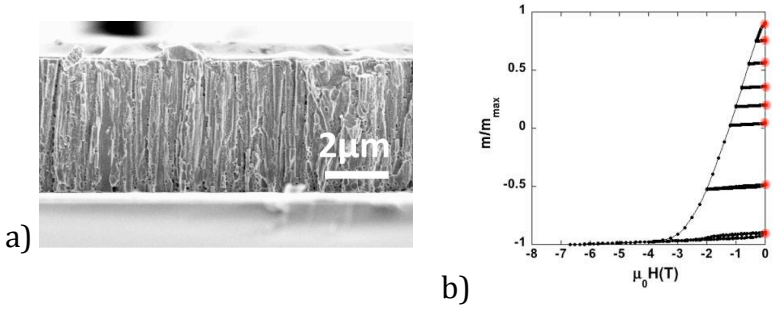

Fig. 5. 18 Scanning Electron Microscopy (a) and recoil loops (b) of a columnar structure NdFeB film ($S_{1.2}$)

Topographic images of the scanned area are depicted in **Fig. 5. 19**a and **Fig. 5. 19**b for $S_{2.6}$ and $S_{1.2}$, respectively. The next two images, **Fig. 5. 19**c and **Fig. 5. 19**d are the corresponding magnetic images. It can be seen that the Ta capping layer is slighty modified by the TMP impact (roughness of tens of nm). Both films are magnetically patterned: one object, magnetized in one direction sank in a material magnetized in the opposite direction. The evolution of the magnetic contrast with an applied field oriented in the same direction as the surrounding material is shown in **Fig. 5. 19**. After TMP, the reversed feature in the high coercivity sample is well defined, **Fig. 5. 19**c, with the black-white asymmetry due to cantilever's tilt and grainy contrast both inside and outside the feature, a signature of the granular nature of films – points discussed before. The medium-coercivity columnar sample however is not saturated, neither inside nor outside the reversed feature, **Fig. 5. 19**d. The situation is similar to the low coercivity sample shown in the previous section and it may be attributed to partial demagnetization due to the samples' self demagnetizing field.

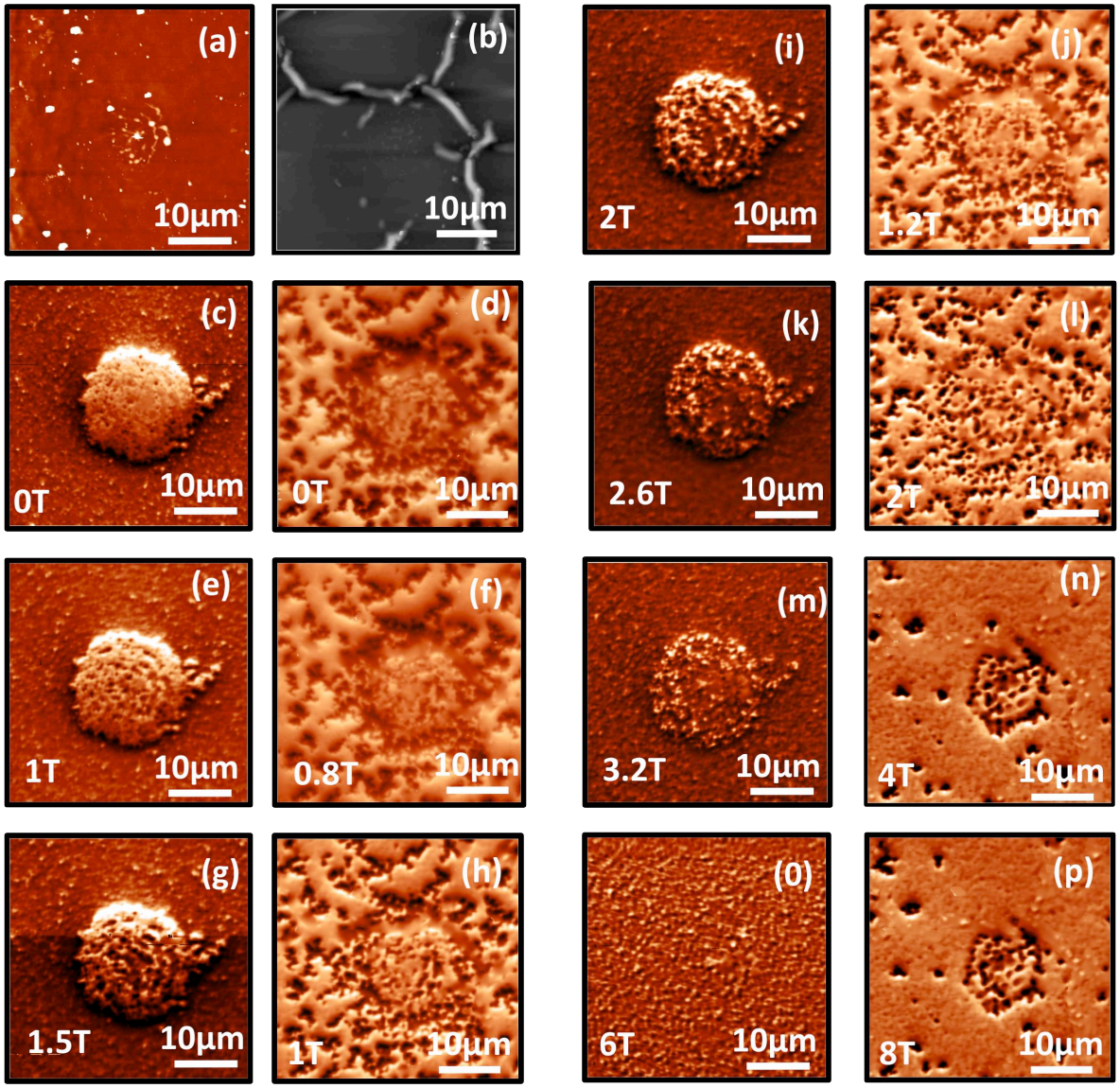

Fig. 5. 19 MFM magnetization reversal for a high H_c NdFeB film with elongated grains, $S_{2.6}$ (column 1 and 3) and a medium coercivity NdFeB film with columnar grains, $S_{1.2}$ (column 2 and 4). The ripples in (b) are due to the squeeze out of a Nd-rich phase during the post deposition annealing step.

However, when magnetized in the opposite direction, **Fig. 5. 19**p, the TMP feature is still not saturated while the matrix is closer to saturation than in **Fig. 5. 19**d. This suggests that the matrix has become partially demagnetized during the patterning process. As a reminder, during the TMP process, a magnetic field of about 0.5T is applied on the entire sample. This field is enough to reduce the magnetization by about 35%, as we can see in the VSM graph, **Fig. 5. 18**b. To understand demagnetization inside the TMP feature, we should consider again the image **Fig. 5. 19**p. The area corresponding to the position of the dot stays partially demagnetized. This indicates that the magnetic material impacted by the laser was modified during the TMP process and the coercivity was lowered locally.

The reversal behavior of magnetization inside the reversed feature of the high coercivity patterned sample, **Fig. 5. 19** (column 1 and 3), is in close agreement with our previous results on a non-patterned sample of similar H_c. The matrix remains unchanged.

The medium coercivity sample was modified during the patterning as explained above. Nevertheless, we can learn something from these images (**Fig. 5. 19** column 2 and 4) also. First, it shows that the patterning process can be destructive. Both the magnetic field applied during patterning and the heat from the laser are potential factors that can alter the magnetic state of the sample, especially in the case of lower corcivity samples. From the magnetization reversal point of view, it is more instructive to analyze the matrix. The material in the TMP feature has been affected by the laser so it is no more representative for the sample. In **Fig. 5. 19**d, the matrix's state corresponds to an applied field (in the direction opposite to the matrix' magnetization) of about 0.5T. It can be seen that reversed interaction domains are formed. Note that in **Fig. 5. 19** the entire image is 50X50μm while in the previous MFM images, the scan size was 10X10μm. By applying higher and higher fields in the opposite direction (to reverse back the magnetization inside the reversed feature), the matrix starts to be re-saturated. It is seen in **Fig. 5. 19**n that many reversed domains disappear and the matrix is saturated over large areas. The domains that were reversed in the non-heated matrix during the TMP process with a relatively small field (0.5T) start to switch direction only in higher fields, >2T. This can be ascribed to the fact that the domains reversed during TMP are stabilized by the stray field from neighboring domains. Consistently, starting from a saturated state and going back to saturation after applying -0.5T the magnetization measurements show that saturation is recovered for fields ≥ 2T(see **Fig. 5. 20**).

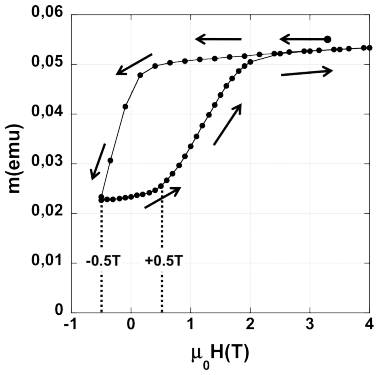

Fig. 5. 20 Minor loop measured for a non-patterned columnar film

As a conclusion to this part, it can be said that the sample with slightly elongated grains present less connectivity than the sample with columnar grains. The lower coercivity of the columnar sample is tentatively attributed to the fact that all grains are in contact with the top/bottom Ta layers, interfaces at which the nucleation of reversed domains may easily start and then propagate through the entire grain. The volume of the columnar grains is on average three times bigger than that of elongated grains so more magnetic material can be reversed starting from the same weak points. Ideally, TEM and/or 3DAP analysis should be carried out to check the grain boundary phase in the case of the columnar film.

As a last example, a very low coercive sample, $S_{0.2}$, is presented in **Fig. 5. 21**. The film is continuous with slightly elongated grains that have widths of 100-200nm.

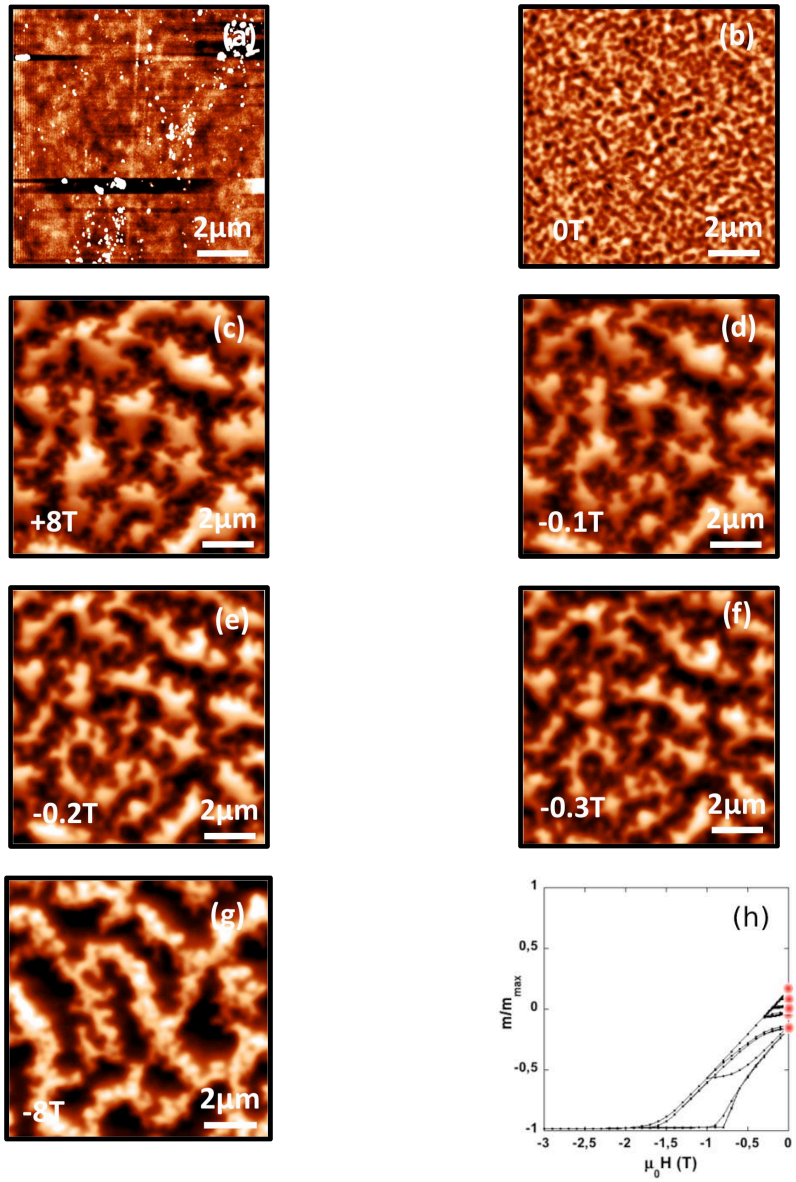

Fig. 5. 21 AFM (a), MFM images in the thermally demagnetized state + different states of remanent magnetisaztion (b-g) of a low coercive film and VSM recoil loops indicating the magnetic remanent states corresponding to the MFM images, (h).

In **Fig. 5. 21**a) the topography is displayed, then the magnetic image in the demagnetized state, **Fig. 5. 21**b. This image is not much different from the two images corresponding to the demagnetized states of the two samples presented in the beginning, **Fig. 5. 12**a and **Fig. 5. 12**b. The next image show the remanent state following magnetization in 8T applied field, **Fig. 5. 21**c. The coercivity is so low that already in this state, the sample is in big part demagnetized. Upon application of a negative field, the magnetic structure does not change much, the size of the black domains increase slightly and after -8T the reversed area is slightly bigger than the rest.

In this chapter, it was shown experimentally, using a local probe technique (MFM), how the magnetic domain structure of NdFeB-based thick films varies with the coercivity. This variation was tentatively linked (with reservations) to differences in the µ-structure. **Fig. 5. 22** presents for comparison 10X10 µm images corresponding to three films analyzed and discussed before (from left to right: $S_{2.55}$, $S_{0.7}$ and $S_{0.2}$). This

figure illustrates how the magnetic connectivity increases with the decrease of sample coercivity.

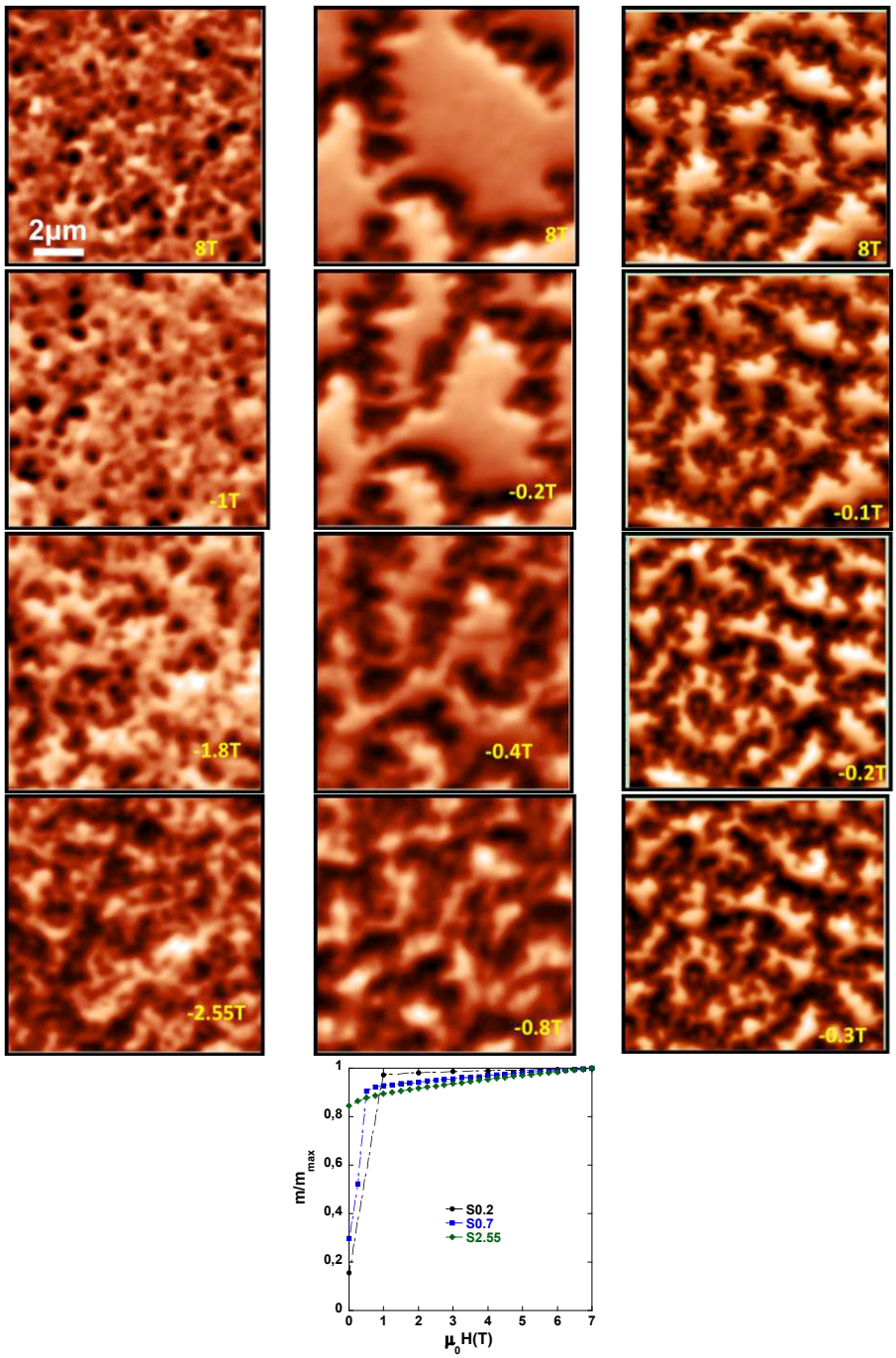

Fig. 5. 22 MFM images corresponding to the first steps of demagnetization of a high H_c film, $S_{2.55}$ (1st column), low H_c, $S_{0.7}$(2nd column) and lower coercivity, $S_{0.2}$ (3th column) and +8T-0T part of hysteresis loops for the 3 samples .

[1] Y. Martin, D. Rugar and H. K. Wickramasinghe, Appl. Phys. Lett. 52, 244 (1988);

[2] H.J. Mamin, D. Rugar, J. E. Stern, R. E. Fontana and P. Kasiraj, Appl. Phys. Lett. 55, 318 (1989);

[3] A. DiCarlo, M. R. Scheinfein and R. V. Chamberlin, Appl. Phys. Lett. 61, 2108 (1992);

[4] L. Abelmann, S. Porthun, M. Haast, C. Lodder, A. Moser, M. E. Best, P. J.A van Schendel, B. Stiefel, H. J. Hug, G. P. Heydon, A. Farley, S. R. Hoon, T. Pfaffelhuber, R. Proksch and K. Babcock, JMMM 190, 135 (1998);

[5] P.C. Gouteff, l. Folks and R. Street, JMMM 177-181, 1241-1242 (1998);

[6] T.G. Woodcock, K. Khopkov, A. Walther, N. M. Dempsey, D. Givord, L. Schultz and O. Gutfleisch, Scripta Mat. 60, 826 (2009);

[7] V. Neu, F. Grosmann, S. Melcher, S. Fähler and L. Schultz, JMMM 290-291, 1263-1266 (2005);

[8] V. Neu, S. Melcher, U. Hannemann, S. Fähler and L. Schultz, Phys.Rev.B 70, 144418 (2004);

[9] J. Thielsch, H. Stopfel, U. Wolff, V. Neu, T. G. Woodcock, K. Güth, L. Schultz and O. Gutfleisch, J. Appl. Phys. 111, 103901 (2012);

[10] L. Folks and R. C. Woodward, JMMM 190, 28 (1998);

[11] A. Hubert, W. Rave and S. L. Tomlinson, Phys. Stat. Sol. (b) 204, 817 (1997);

[12] R. Engel-Herbert, D. M. Schaadt and T. Hesjedal, J. Appl. Phys. 99, 113905 (2006);

[13] M. Kustov, P. Laczkowski, D. Hykel, K. Hasselbach, F. Dumas-Bouchiat, D. O'Brien, P. Kauffmann, R. Grechishkin, D. Givord, G. Reyne, O. Cugat and N. M. Dempsey, J. Appl. Phys. 108, 063914 (2010);

[14] U. Hartmann, Phys. Lett. A 137, 475 (1989);

[15] L. Kong and S. Y. Chou, Appl. Phys. Lett. 70, 2043 (1997);

[16] J. Lohau, S. Kirsch, A. Carl, G. Dumpich and E. F. Wassermann, J. Appl. Phys. 86, 3410 (1999);

[17] F. Dumas-Bouchiat, L. F. Zanini, M. Kustov, N. M. Dempsey, R. Grechishkin, K. Hasselbach, J. C. Orlianges, C. Champeaux, A. Catherinot and D. Givord, Appl. Phys. Lett. 96, 102511 (2010);

[18] A. Wadas and H. J. Güntherodt, Phys. Lett. A 146, 277 (1990);

[19] T. Arie, N. Yoshida, S. Akita and Y. Nakayama, J. Phys. D: Appl. Phys. 34, L43 (2001);

[20] T. E. Schäffer, M. Radmacher and R. Proksch, J. Appl. Phys. 94, 6525 (2003);

[21] D. Rugar, H. J. Mamin, G. Guethner, S. E. Lambert, J. E. Stern, I. McFadyen and T. Yogi, J. Appl. Phys. 68, 1169 (1990);

[22] N. M. Dempsey, A. Walther, F. May and D. Givord, Appl. Phys. Lett. 90, 092509 (2007).

[23] N. M. Dempsey, T. G. Woodcock, H. Sepehri-Amin, Y. Zhang, H. Kennedy, D. Givord, K. Hono and O. Gutfleisch, Acta Materialia, accepted (2013);

VI. Conclusions and perspectives

Conclusions

This thesis work concerned the study of magnetization reversal in NdFeB - based magnets, with the aim to better understand and thus improve coercivity in these technologically important materials. Magnetization reversal was studied using both **"global"** (magnetometry) and **"local probe"** (magnetic force microscopy) techniques. Two types of samples were considered: **bulk magnets** provided by the Toyota Motor Corporation, and **thick film magnets** prepared at Institut Néel, within the framework of this thesis. An original infiltration process had been applied to the bulk magnets to introduce a NdCu grain boundary phase, which resulted in an increase in coercivity. The main results of this work will now be recalled:

Thick films as model systems

Thick films may be considered as model systems in which the μ-structure can be modified by varying different process parameters (film composition, deposition temperature…). During this work, triode sputtering was used to prepare highly textured NdFeB films (typical thickness around 5 μm) with coercivity ranging in value from 2.7 T down to 0.2 T. The grain shape was varied from equiaxed to columnar.

- Coercivity analysis

The first major part of the work concerned the development of coercivity analysis in both the bulk and thick film samples. The aim here was to assess whether phenomenological models (the Micro-Magnetic Model "MM" and the Global Model "GM") could be used to characterize the behavior of these hard magnetic materials. Two distinct contributions are considered in coercivity analysis: i) the "α" parameter that concerns the region where the reversed nucleus is formed, ii) a demagnetizing field parameter ("N") that is associated with the heterogeneous nature of the hard magnetic material.

Analysis of the bulk samples within both the Micro-Magnetic Model and the Global Model shows that the change in coercivity owing to the infiltration process is associated with a change in the demagnetizing field parameter (N), while the parameter characterizing the formation of a reversed domain is essentially unchanged. This suggests that coercivity enhancement is not due to a modification of the nucleation process, but may be associated with decoupling of the main phase grains, in agreement with microstructural observations. Strikingly, at a given temperature, the activation volume is very similar for the different samples.

In the films, on the contrary, the activation volume is found to differ, the higher the coercivity, the lower the activation volume. Note that this behavior is in agreement with the so-called "Barbier plot", according to which the inverse of the activation volume varies as the coercivity.

Analysis of the angular dependence of coercivity is in agreement with previous studies of bulk NdFeB magnets, showing that coercivity is not governed by coherent rotation but expansion of a preformed nucleus. This is compatible with the notion of "pinning", but also with that of "passage-expansion".

In all cases, the fact that the global model gives a fair account of the temperature dependence of coercivity and activation volume, implies that the magnetic properties within the activation volume are close to those of the main phase. This hypothesis, which has been debated for a long time, has recently received support from numerical modeling.

- Magnetic Force Microscopy

The second major part of this thesis concerned a study of magnetization processes in thick films of NdFeB, using magnetic force microscopy. As part of this study, we examined specific aspects of the MFM imaging of hard magnet films. We demonstrated that mechanically stiff MFM probes coated with a hard magnetic material are best suited to the study of thick hard magnetic films, owing to strong probe-sample interactions. One consequence of using hard magnetic probes is the detection of an in-plane component of the sample's stray field, due to the inclination of the probe during scanning. By comparing experimental results with calculated field profiles of model micro-magnets prepared using a thermomagnetic patterning technique, it was found that in the case of permanent magnet films with coarse magnetic domains (and thus long-range stray fields) the stray field of the sample, as opposed to it's derivatives, is imaged in MFM.

Magnetization and demagnetization of NdFeB-based films with different values of coercivity and different microstructures was studied using the MFM. The magnetic domain structure of the thermally demagnetized state is similar for all the samples, irrespective of their coercivity. On the contrary, the magnetization/demagnetization behavior is seen to depend on the coercivity. In low fields, reversible events occur, so that the remanent domain structures do not evolve much, in agreement with the minor hysteresis loop analysis carried out on high and low coercivity films in the magnetometer. However, after application of higher fields, the remanent domain structures are coercivity dependent. Large interaction domains are clearly observed to develop in the low coercivity sample, while high coercivity samples are characterized by a fine granular magnetic structure. Note that the persistence of this granular structure, even after the application of 8 T, when the film is practically saturated, may be explained by the sensitivity of the hard MFM tip to in-plane field components associated with local variations in the alignment of individual grains. The collective nature of reversal seen in the magnetization and demagnetization sweeps of medium to low coercivity samples is due to exchange coupling between grains. This results from direct contact between neighboring hard magnetic grains. Magnetization reversal in the high coercivity films, which are known to have continuous Nd-rich grain boundary phases, occurs by a mixture of nucleation and growth of existing reversed domains.

Perspectives

Based on recent progress made by a number of groups with grain boundary engineering of NdFeB magnets, there is much potential to further increase the coercivity of this technologically important material. Films may be considered as model samples, in which the microstructure can be controlled through various processing parameters. Multi-phase structures may be produced by the annealing of single layer alloy deposits or alternatively multi-layer deposition may be used to directly produce a multi-phase architecture in which the composition and thickness of the individual phases is controlled. Multi-layer deposition also allows for the study of diffusion between phases or along grain boundaries.

As an example of multi-phase structures produced by the annealing of single layer alloy deposits, some preliminary experiments have been carried out in the framework of this thesis, to study the influence of the addition of Cu in Nd-rich NdFeB films (in this case, a piece of Cu was added to the NdFeB target). Results presented in Annex 9, confirm the positive benefit of adding Cu on the coercivity of NdFeB thick films. Further structural (TEM, 3DAP) and magnetic (coercivity analysis, MFM..) studies are required to better understand and optimize this approach. Controlled diffusion in multi-layer structures has also begun. We think that these various film-based approaches hold much potential for the development of magnets with reduced RE-content, including RE-lean hard-soft nanocomposites, as well as RE-free materials.

Concerning coercivity analysis, this could be further developed together with micro-magnetic simulations that take into account thermal activation effects. We believe that the activation volume is an important parameter to be considered in the study of magnetization reversal in hard magnetic materials.

Magnetic Force Microscopy is a powerful tool that may serve in the understanding of magnetization reversal. In the case of thick films, imaging of the cross section of films should shed more light on the influence of grain shape and interfaces on reversal. The development of quantitative MFM imaging, with the use of probes of known magnetization, is also of interest.

The development of permanent magnets relies on a triangular approach combining sample preparation, characterization (structural and magnetic) and modeling. Recent advances in all three domains (press-less processing, infiltration, thin and thick film processing; atomic scale resolution imaging (TEM, 3DAP), MFM imaging under high field; molecular dynamics and micromagnetic simulations including thermal activation) has already led to significant improvements in the extrinsic properties achievable, and holds the key to improving our understanding of these materials.

Annex 1. Model of an AFM cantilever

We recall the usual description of a cantilever for atomic force microscopy with a harmonic oscillator along a direction with coordinate z, with inertia m, stiffness k and damping Γ, subject to an external force F:

$$m\frac{d^2z}{dt^2} + \Gamma\frac{dz}{dt} + kz = F(z,t) \qquad \textbf{(A1. 1)}$$

This description is very adequate for the physics of magnetic force microscopy. F may contain the cantilever excitation at a given angular frequency ω, as well as the force created by the sample F_{ts}. The latter is classically expanded to first order to remain within the frame of a harmonic oscillator. As dF/dz is much smaller than the cantilever stiffness, this results simply in a linear shift of the resonance angular frequency from its natural value, $\omega_0 = \sqrt{k/m}$, to $\omega = \omega_0(1 - \frac{1}{2k}\frac{dF}{dz})$. In magnetic force microscopy the information about the magnetic force is then mapped as the phase shift induced on the cantilever when excited at $\omega = \omega_0$:

$$\Delta\Phi = -\frac{Q}{k}\frac{dF}{dz} \qquad \textbf{(A1. 2)}$$

$Q = \sqrt{mk}/\Gamma$ is the quality factor of the cantilever.

The linear relationship in (A1. 2 remains valid as long as the phase shift is reasonably smaller than π/4. As the force is the gradient of energy, we may rewrite the phase shift as:

$$\Delta\Phi = \frac{Q}{k}\frac{d^2E_{ts}}{dz^2} \qquad \textbf{(A1. 3)}$$

This expression is particularly useful for the analysis of magnetic forces.

Annex 2. Model of the tip-sample magnetic interaction

Formalisms for describing the tip-sample interaction in magnetic force microscopy were reported in a number of papers[1,2,3]. We recall the basic features here, with a view to providing notations for the discussion in the manuscript. We consider the interpretation based on sample surface charges[4], which may be considered suited for imaging surfaces of bulk materials and thick films. We also assume that both tip and sample have a rigid distribution of magnetization, *i.e.* we do not consider mutual (susceptibility) effects.

The tip-sample energy at fly height *z* may be expressed in the most general way as:

$$E_{ts}(z) = -\mu_0 M_i \int_{-\infty}^{+\infty} H_i(z+h)s(h)\,dh \qquad \textbf{(A2. 1)}$$

where *i* is summed over all three directions, *h* is the coordinate along the axis of the tip, and *s*(*h*) is the integrated area of magnetized material at height *h* on the tip, calculated from its apex. This convoluting function was called a *probe* function[4].

In the following we assume that the tip oscillates along the vertical direction so that only spatial derivatives along *z* need to be considered to calculate phase shifts (See [1] for the general description).

$$s_{dip}(h) = v_0\delta(0) \text{ (for dipole model)} \qquad \textbf{(A2. 2)}$$

with δ being the delta function and v_0 the dipole volume;

$$s_{mono}(h) = s_0 H(h) \text{ (for monopole model)} \qquad \textbf{(A2. 3)}$$

with *H* the Heaviside function and s_0 the area of the equivalent cylinder of magnetic material.

Integrating by parts and neglecting boundary conditions with the argument that *H* decays towards infinity, the phase shift may be expressed in different ways:

$$\Delta\Phi = -\mu_0 M_i \int_{-\infty}^{+\infty} \frac{d^2 Hi}{dz^2}(z+h)s(h)\,dh \qquad \textbf{(A2. 4)}$$

$$\Delta\Phi = \mu_0 M_i \int_{-\infty}^{+\infty} \frac{dH_i}{dz}(z+h)\frac{ds}{dz}\,dh \qquad \textbf{(A2. 5)}$$

$$\Delta\Phi = -\mu_0 M_i \int_{-\infty}^{+\infty} H_i(z+h)\frac{d^2 s}{dz^2}(h)\,dh \qquad \textbf{(A2. 6)}$$

For simple models, one should use the expression for which the probe function is a delta function: **(**(A2. 4**)** for a dipole and **(**(A2. 5**)** for a monopole, showing in a straightforward fashion that within these models, is it the second or first *z* derivative of the stray field at height *h* which is being considered.

Let us discuss the suitability of these models to describe different situations.

In the case of a very fast decay of stray field above the sample, and rapid lateral variation, only the magnetic capping at the nearly flat end of the apex is involved in the tip-sample force, and the dipole model is the best suited.

The monopole model is more appropriate for a slower vertical decay and lateral variation, typically on the range of about 100 nm. In this case all the magnetic material deposited around the tip apex is involved in the interaction. Assuming that deposition is performed in a directional manner from above a tip with parabolic shape, it can be readily shown that in the case where the deposit thickness is smaller than the apex radius, the amount of material per unit z is constant. This justifies the monopole model.

When the stray field extends way above the apex of the tip, then the predominant shape is not anymore parabolic but rather conical. To describe this case, which is most relevant for the measurements presented here, we thus consider the model of a cone capped with a uniform layer of thickness e (measured along the direction perpendicular to the local surface of the cone) and half angle α:

$$s_{cone}(h) = 2\pi h e \tan\alpha \qquad \textbf{(A2. 7)}$$

Note that within a constant, s_{dip} is the derivative of s_{mono}, which itself is the derivative of s_{cone}. Thus, equation **(**(A2. 6**)** shows that in this case it is the stray field along the direction of magnetization of the tip that is imaged.

---

[1] D. Rugar, H.J. Mamin, P. Guethner, S.E. Lambert, J. E. Stern et al., J. Appl. Phys. 68, 1169 (1990);

[2] J. Lohau, S. Kirsch, A. Carl, G. Dumpich and E.F. Wassermann, J. Appl. Phys. 86, 3410 (1999);

[3] R. Proksch & D. Dahlberg, Y. Zhu *(ed.),* Modern techniques for characterizing magnetic materials, Magnetic force microscopy, *Springer*, 411 **(2005);**

[4] A. Hubert, W. Rave and S.L. Tomlinson, Phys. Stat. Sol. (b) 204, 817 (1997).

Annex 3. Calculation of hysteresis loops and derived angular dependence of coercivity for an assembly of magnetically decoupled uni-axial particles

Hysteresis loops were analytically calculated for an assembly of uni-axial, magnetically decoupled, particles. Since the purpose of this calculation was to apply the results to the angular dependence of coercivity experiments, two models, one corresponding to the Stoner Wohlfarth approach and the other one corresponding to a $1/\cos(\theta)$ law (see chapter II) were developed.

The general formalism is similar for the two models:

- consider a system made of an assembly of independent uni-axial particles characterized by their spontaneous magnetization and anisotropy constant (in our case, $Nd_2Fe_{14}B$). The particles are characterized by a certain distribution of orientations with respect to a privileged direction, **O**. The associated distribution function is assumed to be described by:

$$p(\Theta_K, \Phi_K) = \frac{N+1}{2\pi}\cos(\Theta_K)^N \qquad \textbf{(A3. 1)}$$

The angles used in equation (A3. 1) are as shown schematically in **Fig. A3. 1.**

For each given particle in the assembly, the energy includes two terms, the anisotropy energy and the Zeeman energy:

$$E(\Theta, \Phi) = K\sin^2(\Theta) - MH\cos(\Phi) \qquad \textbf{(A3. 2)}$$

In this expression, the applied field is assumed to be vertical and the angles Θ_K and Φ_K, characterizing the direction K of easy magnetization ($0 \le \Theta_K \le \frac{\pi}{2}; 0 \le \Phi_K \le 2\pi$) and Θ_M and Φ_M ($0 \le \Theta_M \le \pi; 0 \le \Phi_M \le 2\pi$), the direction of the magnetization, M, are expressed with respect to it (**Fig. A3. 1**).

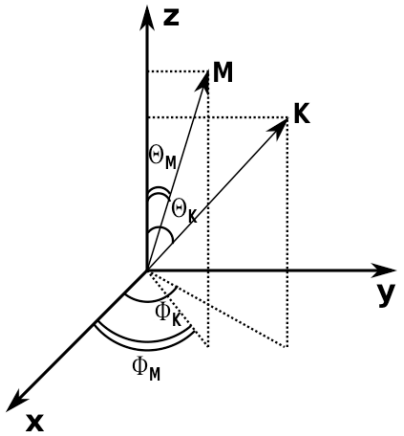

Fig. A3. 1 Definition of angles characterizing the direction of easy axis (Θ_K and Φ_K) and magnetization (Θ_M and Φ_M).

For each given grain, characterized by its specific orientation (i.e. a certain value of the two angles Θ_K and Φ_K) calculation starts from a completely saturated state. The field is decreased step by step and for every value, the angles Θ_M and Φ_M corresponding to the minimization of the energy (expression (A3. 2) are

derived. The calculation is repeated for each possible orientation of the particles. The total magnetization is the sum of the magnetization obtained for each particle weighted by the probability that the corresponding orientation occurs.

In order to calculate the hysteresis loops for different orientations of the applied field, the angle between the average easy axis and the z-axis can be changed as schematically shown in **Fig. A3. 2**.

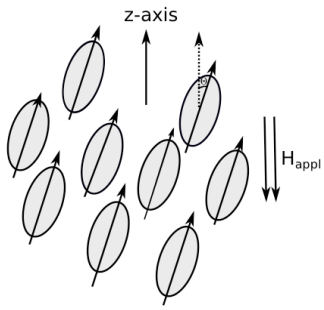

Fig. A3. 2 Scheme that shows how the angle between the applied field and magnetization can be changed.

Remarks concerning the distribution function of easy directions:

In equation (A3. 1), N is a parameter that characterizes the degree of orientation with respect to **O**. N can take any value ≥ 0, N = 0 meaning random distribution. **Fig. A3. 3**a shows the plots of $\cos(alpha)^N$ for different values of N, from 1 to 10^6. It can be seen in **Fig. A3. 3**b how the Half Width at Half Maximum (HWHM) decreases by increasing the value of N, up to 1000.

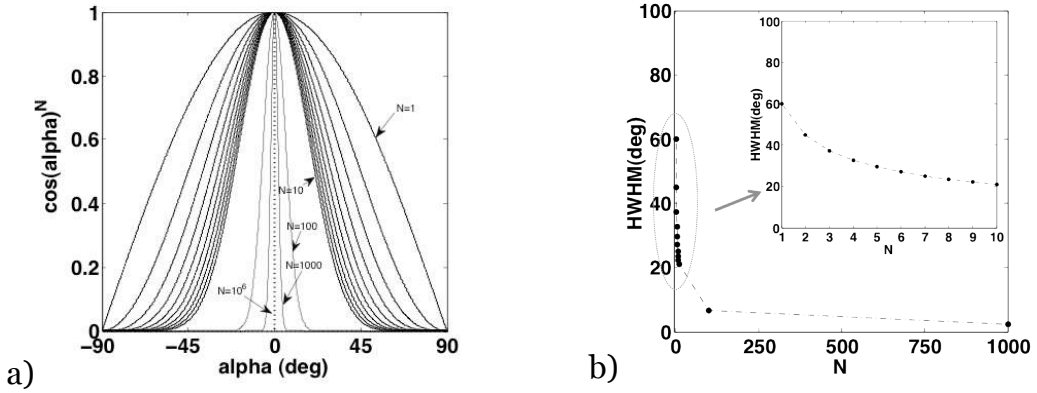

Fig. A3. 3 Evolution of $\cos(\alpha)^N$ with increasing value of N **(a)**; HWHM of the curves in **Fig. A3. 3**a function of N **(b).**

The distribution of grains depending on the value chosen for N is shown schematically in **Fig. A3. 4**. If N = 0, particle orientation is completely random, **Fig. A3. 4**a, while, for a value of 10^6 (dotted line in **Fig. A3. 3**a) all grains can be considered aligned along the z-direction, **Fig. A3. 4**c.

In real samples, there is always an angular distribution around z-axis, the particles looking more like in **Fig. A3. 4**b. In sintered magnets, we use typically N = 10 which corresponds to a HWHM of around 21°.

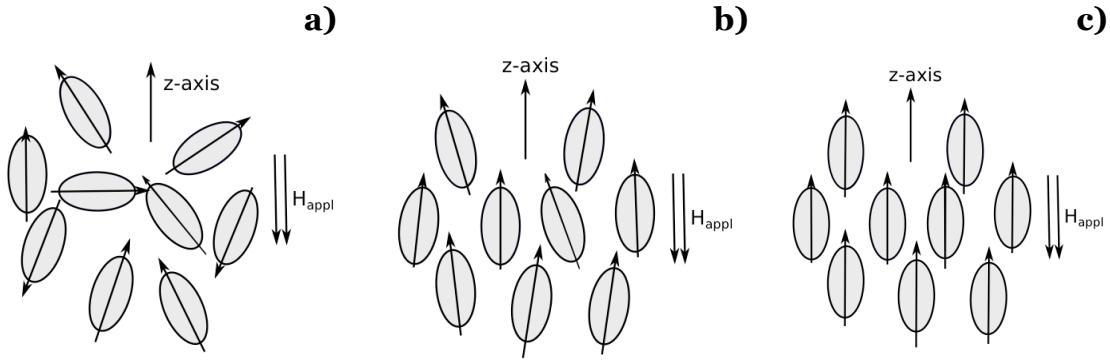

Fig. A3. 4 Schematics of the particle distribution for: random orientation, N = 0 **(a)**; a certain distribution around z-axis, intermediate N **(b)** and fully z-aligned grains, N = 10^6 **(c).**

As mentioned above, the behavior of particles following either the SW or the $1/\cos(\theta)$ law were modeled. The difference between the two models is apparent in the way the energy maximum is tested at each step. The theory behind the two models was described in chapter II. Here, the differences in the calculations are only specified.

1. Stoner Wohlfarth(SW) Model This case corresponds to the behavior of an ideal system, as described by expression ((A3. 2)). For any given applied field, there are two energy minima in general, separated by an energy barrier. The magnetization is assumed to lie along the energy direction corresponding to the closest local energy mininum, although the energy may be higher than the one corresponding to the other moment orientation. This explains the possible occurrence of hysteresis, and thus coercivity.

2. $1/\cos(\theta)$ **Model**

In this case, energy minimization is conducted as above until the projection of the applied field along the easy direction reaches an arbitrarily defined critical value. Above this value, the magnetization is assumed to align along the direction corresponding to the absolute energy minimum. This permits that reversal occurs at field values that are smaller than the anisotropy field, as always found in experiments. The value of the critical field is set to be αH_a where H_a is the anisotropy field and α is a parameter ≤ 1, typically around 0.2 - 0.3. When $\alpha = 1$, the usual Stoner Wohlfarth model is recovered.

Test calculations:

1.Random distribution of the grains. Calculation using the first model and comparison to SW original paper[1]

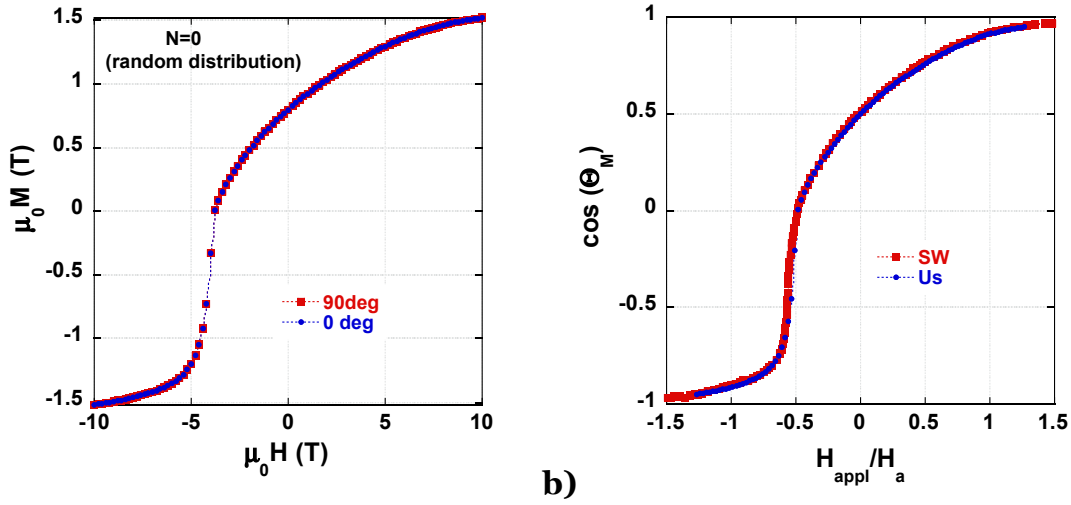

Fig. A3. 5 Demagnetization loops calculated for two orientations of H_{appl} in the case of an assembly of randomly distributed uniaxial particles using SW model **(a)**; comparison between the loops obtained from the calculations presented in this work and the one published by SW[1] **(b).**

The demagnetization loops were calculated for the case of a random distribution of particle orientation (N = 0, **Fig. A3. 4**a). The spontaneous

[1] E. C. Stoner and E. P. Wohlfarth, Phil. Trans. of the Roy. Soc. Lond. Series A, Math. And Phys. Sc. 240, 599 (1948);

magnetization and anisotropy constant that were used are the ones corresponding to $Nd_2Fe_{14}B$, at 300 K and presented in Annex 4. It is observed that the curves do not change if the angle of the applied field is modified. In **Fig. A3. 5**a, two curves, for θ = 0° and θ = 90° are presented as examples. Moreover, if the result is compared to the curves published in the original paper written by Stoner and Wohlfarth[1], a good agreement is found – **Fig. A3. 5**b. Notice that in the second figure, the x and y-axis are the applied field normalized to the anisotropy field and the cosinus of the angle between the magnetization and the magnetic field, respectively. It was plotted in this manner to keep the notations used in the cited paper.

2. Fully textured systems. Calculation of $H_c(\theta)$ curves with the two models

The demagnetization loops calculated for a fully textured (N = 10^6) assembly of $Nd_2Fe_{14}B$ particles are shown in **Fig. A3. 6**a for the Stoner Wohlfarth model and **Fig. A3. 6**b for the $1/\cos(\theta)$ one, considering α = 0.2.

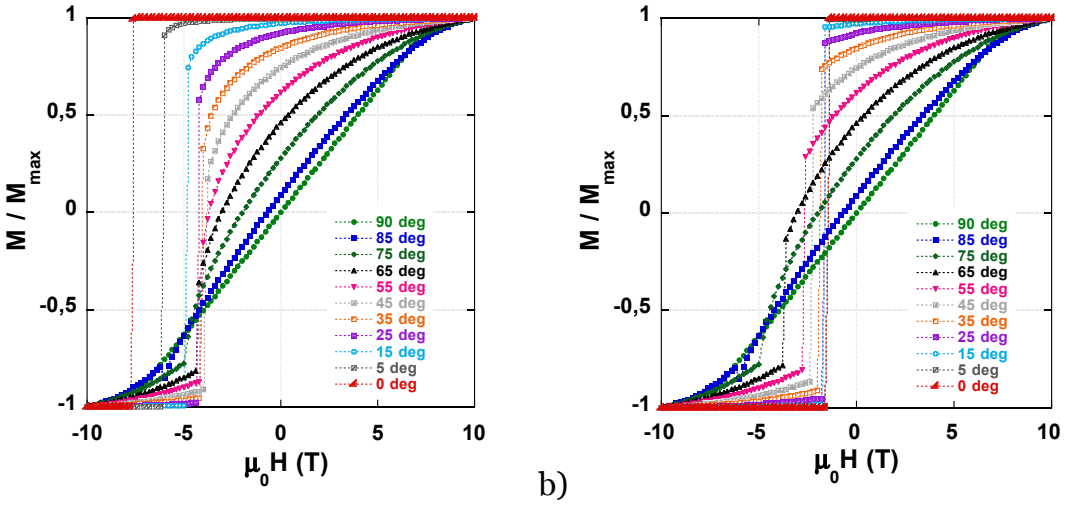

Fig. A3. 6 calculated demagnetization loops for a fully textured assembly of particles (N=10^6) in the framework of the Stoner Wohlfarth model **(a)** and calculated demagnetization loops for a fully textured assembly of particles (N=10^6) in the framework of the $1/\cos(\theta)$ model **(b).**

The switching field function of the direction of the applied field is derived from the calculated loops. In the case of the SW model, the well-known angular dependence of the coercive field is recovered. H_c decreases from $H_c=H_a$ at $\theta = 0°$ to $H_c=1/2H_a$ at 45° and then it increases again up to H_a at 90°, as shown in **Fig. A3. 7**a.

For the $1/\cos(\theta)$ law, the behavior is a little bit more complex, depending on the value of the α parameter, i.e. on the value of the switching field at 0°. In **Fig. A3. 7**b, three parameters are plotted as a function of θ: $1/\cos(\theta)$, $H_c(\theta)/H_c(0)$ for α = 0.06, a coercivity of 0.4 T and $H_c(\theta)/H_c(0)$ for α = 0.2, coercivity of 1.5 T. In the case of very small values of α, the curve is behaving very closely to $1/\cos(\theta)$. However, if α is closer in value to experimental observations, the curve changes at high angles and the increase of coercivity is not as for lower coercivity

field values. This effect is due to the fact that the moment rotation under field is no more negligible.

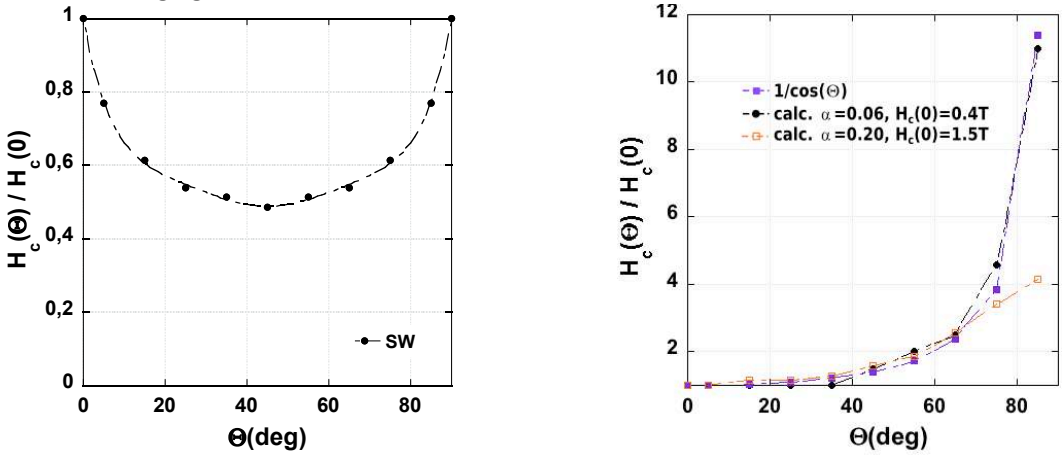

Fig. A3. 7 Angular dependence of coercivity obtained from the loops calculated using the SW model for N=10^6 **(a)**; Angular dependence of coercivity obtained from the loops calculated using the $1/\cos(\theta)$ model for N=10^6, for two values of α, 0.06 and 0.2; $1/\cos(\theta)$ is also shown for comparison **(b).**

When the angular distribution of easy axes is taken into account, the above curves, describing the angular dependence of coercivity, are altered further. This is illustrated in **Fig. A3. 8**. Two curves are shown for each model, one for N = 10^6 (fully textured) and one for N = 10 (HWHM = 21°).

a) b)

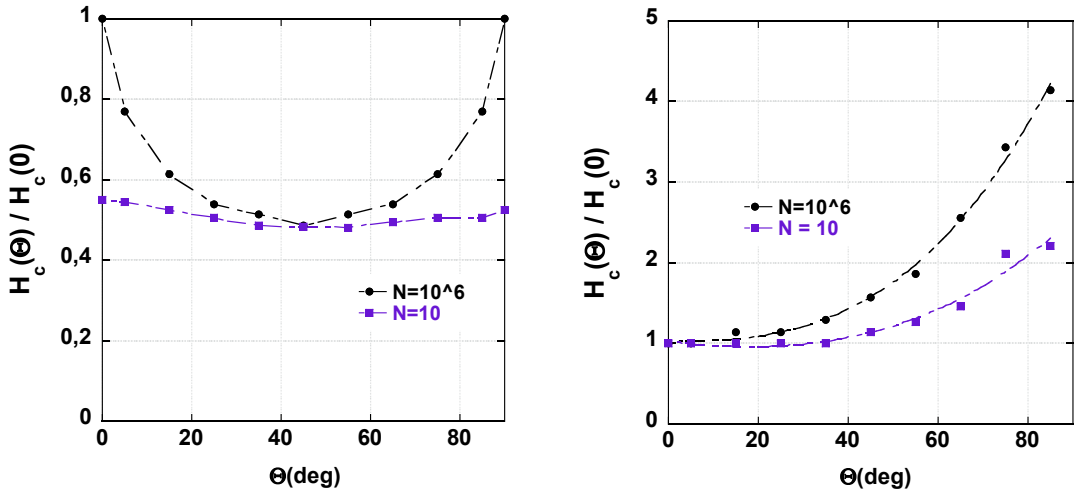

Fig. A3. 8 Angular dependence of coercivity obtained from the loops calculated using the SW model for N=10^6 and N=10 **(a)**; Angular dependence of coercivity obtained from the loops calculated using the $1/\cos(\theta)$ model for N=10^6 and N=10 **(b)**.

Annex 4. $Nd_2Fe_{14}B$ Spontaneous magnetization and anisotropy constants

The table and graphs below show the values of spontaneous magnetization and anisotropy constants that were used in the previous analyses.

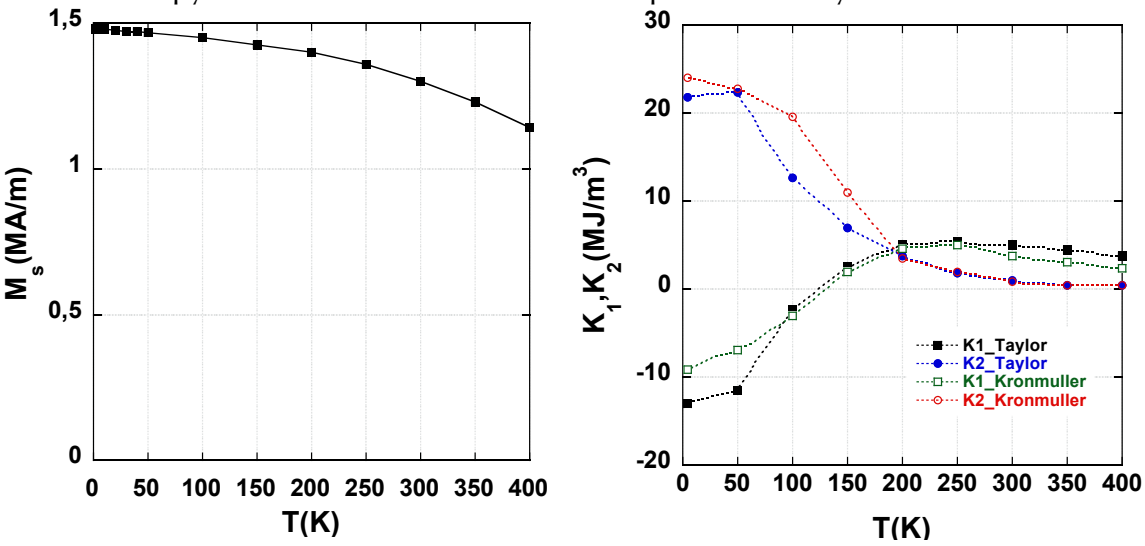

Fig. A4. 1 $M_s(T)$, $K_1(T)$ and $K_2(T)$ for $Nd_2Fe_{14}B$. Two sources are used, for comparison[1,2].

The numbers are given in **Table A4. 1**:

T(K)	M_s(MA/m)	M_s(T)	K_1^t(MJ/m^3)	K_2^t(MJ/m^3)	K_1^k()_kron	K_2^k()_kron
400	1.14	1.4326	3.75	0.4	2.4	0.4
350	1.23	1.5457	4.5	0.45	3	0.45
300	1.3	1.6336	5.05	1	3.75	0.9
250	1.36	1.7090	5.4	1.75	5	2
200	1.4	1.7593	5	3.75	4.6	3.5
150	1.425	1.7907	2.5	7	2	11
100	1.452	1.8246	-2.4	12.6	-3	19.6
50	1.468	1.8447	-11.5	22.3	-7	22.8
40	1.47	1.8473	-	-	-	-
30	1.473	1.8510	-	-	-	-
20	1.476	1.8548	-	-	-	-
10	1.478	1.8573	-	-	-	-
4.2	1.478	1.8573	-12.996	21.8	-9.11	23.97

Table A4. 1 M_s, K_1 and K_2 of $Nd_2Fe_{14}B$ at temperatures between 4.2 K and 400 K.

[1] D. W. Taylor, PhD thesis (1992);

[2] K. D. Durst et al., JMMM 59, 86 (1986).

Annex 5. Calculation of spatial derivatives of the stray field of a uniformly magnetized prism

Analytical formulas have long been used for calculating the stray field arising from uniformly magnetized prisms[1]. A concise formalism for the use of these formulas was introduced by Hubert, based on the core Green function $F_{000} = \frac{1}{r}$ and its space primitives F_{ijk} of any order and along any direction[2]. For instance, F_{000} integrated once along *x* and once along *z* is written F_{101}. The scalar potential arising at any point of space from a charged plate can be expressed using these functions. The stray field arising from a uniformly magnetized body may then be expressed using these functions, summing over its oppositely charged surfaces.

For the present case we needed to calculate first and second derivatives of the stray field arising from uniformly magnetized prisms, thus described by sets of two plates with opposite charges. For flexibility and ease of calculation we extended the notation of Hubert and calculated F_{ijk} for various and indifferently positive or negative exponents. For instance, $\frac{dH_x}{dz}$ arising from a rectangular plate in the *xy* plane involves F_{01-1}: the potential involves F_{110}, calculating H_z turns it into F_{010}, and the *z* derivative into F_{01-1}. The function is then used in the following way for a plate centered on (0,0,0) and of side length *a* and *b*:

$$H_z(r) = -\frac{M_s}{2} \sum_{\varepsilon_i=\pm1;\varepsilon_j=\pm1} \varepsilon_i \varepsilon_j F_{01-1}(x - \varepsilon_i \frac{a}{2}, y - \varepsilon_j \frac{b}{2}, z) \qquad \textbf{(A5. 1)}$$

Below is the expression of the functions required to calculate the second spatial derivative of field arising from plates.

$$F_{11-1} = -\frac{P_z}{z} \qquad \textbf{(A5. 2)}$$

$$F_{1-10} = -\frac{xy}{r(v+w)} \qquad \textbf{(A5. 3)}$$

$$F_{11-2} = \frac{xy}{wr^2 + uv}(r + \frac{w}{r}) \qquad \textbf{(A5. 4)}$$

$$F_{-100} = -xF_{000}^3 \qquad \textbf{(A5. 5)}$$

$$F_{-11-1} = \frac{xyz}{r^3}\frac{3r^2 - v}{(r^2 - v)^2} \qquad \textbf{(A5. 6)}$$

$$F_{1-20} = \frac{x(2v - w)r^2 - xuv}{r^3(v+w)^2} \qquad \textbf{(A5. 7)}$$

$$F_{11-3} = \frac{xyzr}{(uv + wr^2)}\left[\begin{array}{l} -\frac{2r^2}{uv + wr^2}(1 + \frac{w}{r^2})^2 \\ +\frac{1}{r^2}(3 - \frac{w}{r^2}) \end{array}\right] \qquad \textbf{(A5. 8)}$$

With these we use the same notations as Hubert:

$$u = x^2; v = y^2; w = z^2 \qquad \textbf{(A5. 9)}$$

$$P_z = z \cdot a\tan(\frac{xy}{zr}) \qquad \textbf{(A5. 10)}$$

[1] P. Rhodes and G. Rowland, *Demagnetizing energies of uniformly magnetized rectangular blocks,* Proc. Leeds Philos. Lit. Soc. Sci. Sect., 6, 191-210 (1954);

[2] A. Hubert and R. Schäfer, *Magnetic Domains, the Analysis of Magnetic Microstructures,* Springer.

Annex 6 Influence of topographic features on MFM imaging

In this annex, information about the surface state of NdFeB and SmCo thick films for MFM imaging, is given. Even though the material of interest is NdFeB, in all the study presented in Chapter V, section V.2, the patterned samples were thick films of SmCo because their surface is smoother, thus more appropriate for analysis of MFM imaging. For comparison, two topographic images are shown in **Fig. A6. 1**, corresponding to SmCo and NdFeB thick films, respectively. The z-scale represents the height of the samples and it is seen here that there is an order of magnitude difference between the two.

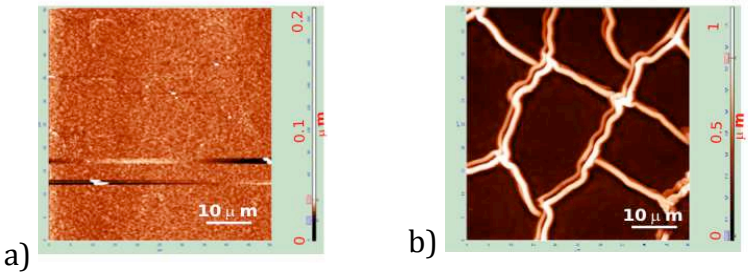

Fig. A6. 1 Surface topography imaged using the atomic force microscope for SmCo (a) and NdFeB (b) thick films.

The big line features in **Fig. A6. 1**b correspond to bumps on the surface of the NdFeB films as a result of the squeeze out of the Nd-rich secondary phase during annealing. These features can be even 1 µm high, which could be problematic for MFM imaging for two reasons:

1) the tip gets damaged very easily – the magnetic material may be removed by friction or even the entire tip may be broken;

2) when very close to the surface, in the case of very rough samples, the magnetic image presents traces of the topographic image, as can be seen in **Fig. A6. 2**a. In this case, a TMP NdFeB film is imaged. The pattern has a chessboard structure with alternating up and down 50x50 µm squares.

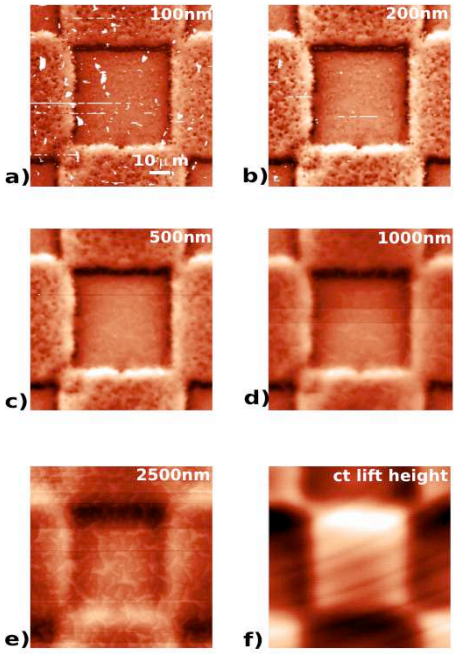

Fig. A6. 2 MFM maps of TMP NdFeB film for different lift heights (a-e) and the map corresponding to constant height,1-step MFM (f).

For higher lift heights (dz) the influence of the topography becomes less important but it appears again under another shape at very big dz - **Fig. A6. 2**e. The white irregular maze-like structure correspond to the surface roughness and is not of magnetic origin. To check that, another type of imaging was tried, instead of the typical 2-step MFM technique. The height was fixed during the 2nd step, without registering the topography initially. In this case, the height being constant,the tip is at different distances from the magnetic material at different places on the sample. The exact distance is not known. By comparison with images taken before, we assumed the distance is big enough to observe the white structures observed in **Fig. A6. 2**e, but it is not the case as it can be seen in **Fig. A6. 2**f.

A second test of the nature of this white structure consists in performing MFM-like measurement with an AFM probe, with no magnetic coating. Results are shown in **Fig. A6. 3**. The height measured during the first step (a) and the phase shift during the 2nd step (b) look alike, the features being present in both cases. In case b there should be no signal since the probe is not magnetic and it is far away from the sample.

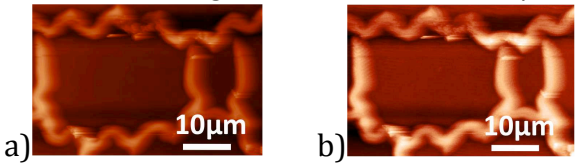

Fig. A6. 3 1st (a) and 2nd (b) step signal measured with a non-magnetic probe.

It was shown experimentally that the features present on the surface of the NdFeB film are non magnetic and they can alter the magnetic image registered during the 2nd step of the MFM process.

Annex 7. Structural and magnetic characterization of the low H_c and a high H_c thick films studied by MFM (chapter V).

Structural and magnetic characterization (VSM, SEM, TEM and XRD) was performed on two NdFeB thick films with different coercivities (0.7 T and 2.55 T), **Fig. A7. 1**.

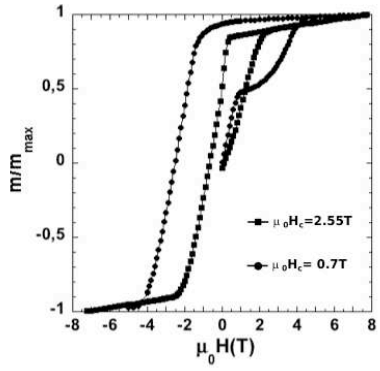

Fig. A7. 1 Hysteresis loops measured on the low ($S_{0.7}$) and high ($S_{2.55}$) H_c films.

The two films have microstructures with slightly elongated grains as the SEM images in **Fig. A7. 2** show. The size of the grains is different for the two films (length of 0.1 - 0.35μm, width 0.1 - 0.15μm for $S_{0.7}$; length of 0.5 - 1.0 μm and width 0.2 - 0.25μm for $S_{2.55}$) but the aspect ratio is similar.

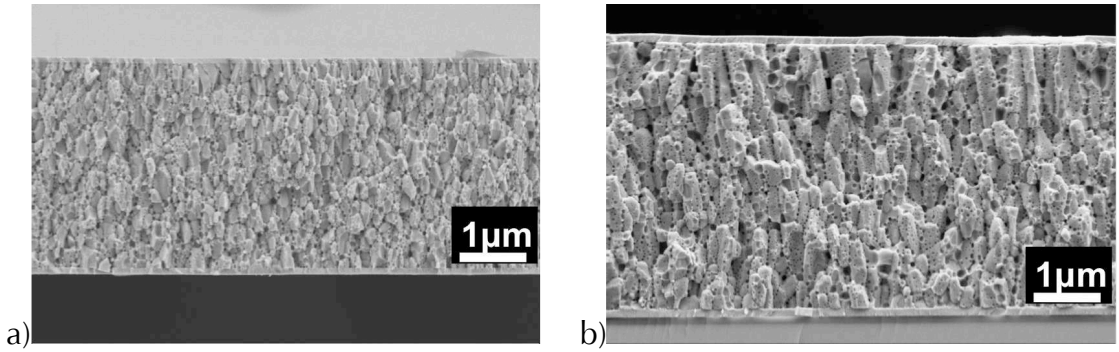

Fig. A7. 2 SEM side view image corresponding to the low H_c , $S_{0.7}$(a) and high H_c $S_{2.55}$(b) films.

The (006) XRD pole figures shown in **Fig. A7. 3** for the two samples indicate that the grains c-axes are perpendicular to the films' surface within an angle of 25 deg for the low coercivity sample and 20 deg for the high coercivity sample.

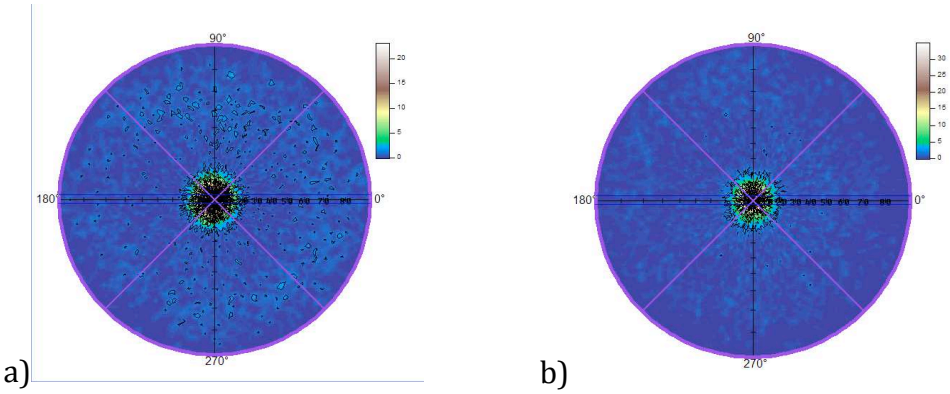

Fig. A7. 3 (006) pole figures corresponding to the low H_c ,$S_{0.7}$(a) and high H_c, $S_{2.55}$(b) films.

High resolution analysis (TEM, atom probe) were performed on similar samples. In **Fig. A7. 4**, TEM images corresponding to the two samples are shown. The sample with higher H_c has significantly more intergranular phase.

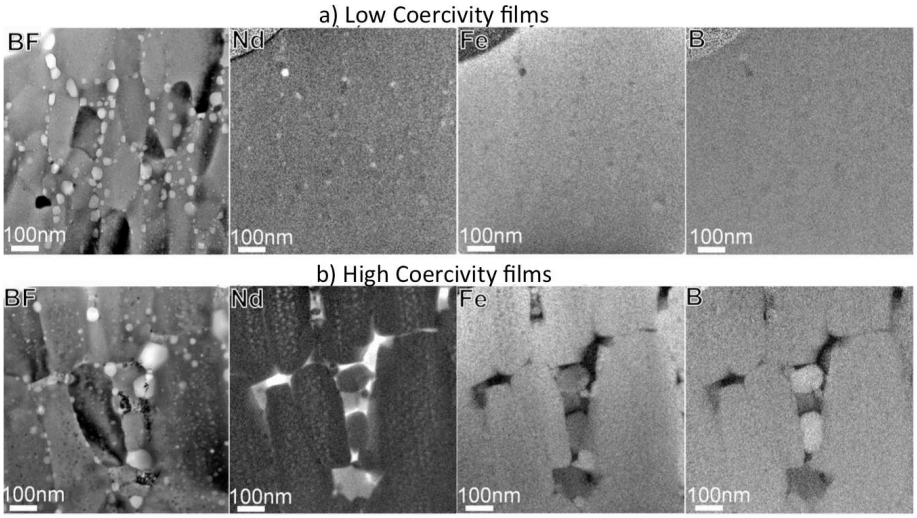

Fig. A7. 4 TEM bright field images and energy filtered elemental maps (Nd, Fe, B) of the low H_c,$S_{0.7}$ (a) and high H_c $S_{2.55}$(b) films (***H. Sepehri-Amin and K. Hono, NIMS, Japan***).

A high resolution TEM image of a grain boundary corresponding to the high coercivity film is shown in **Fig. A7. 5**.

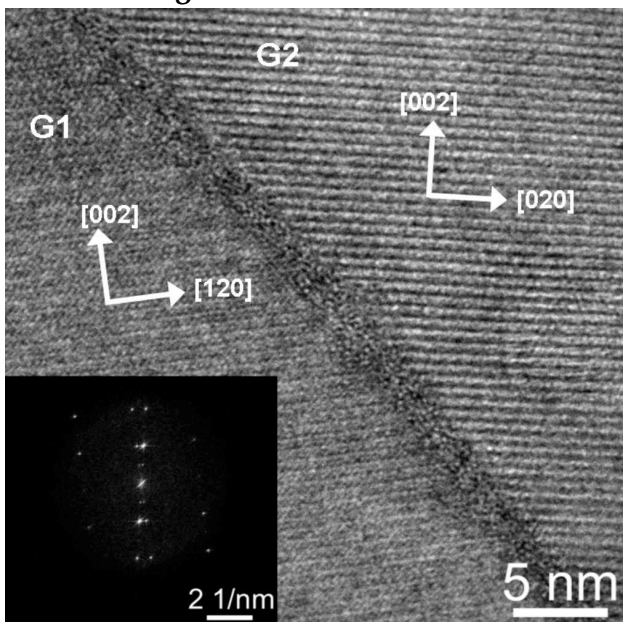

Fig. A7. 5 High resolution TEM image of a grain boundary of the high H_c film, $S_{2.55}$; inset: FFT of the image ***(T. Woodcock and O. Gutfleisch, IFW, Germany)***.

For the same sample, high H_c, atom probe analysis revealed the presence of Cu at the grain boundary, **Fig. A7. 6**.

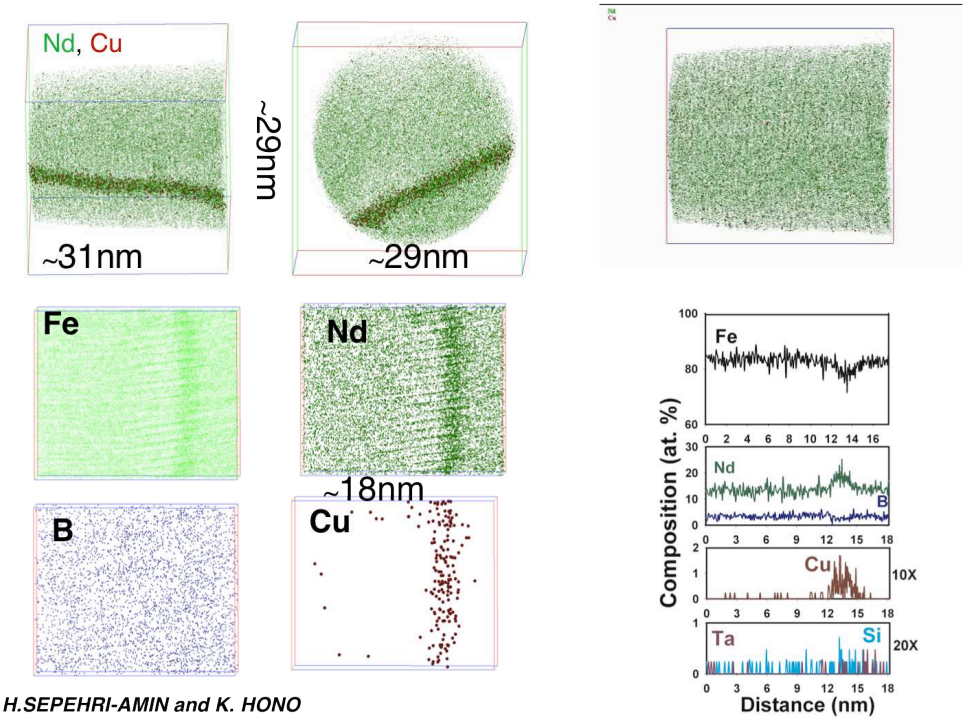

Fig. A7. 6 Atome probe maps and elemental analysis of the high H_c film, $S_{2.55}$, grain boundary.

Annex 8 . Phase diagrams

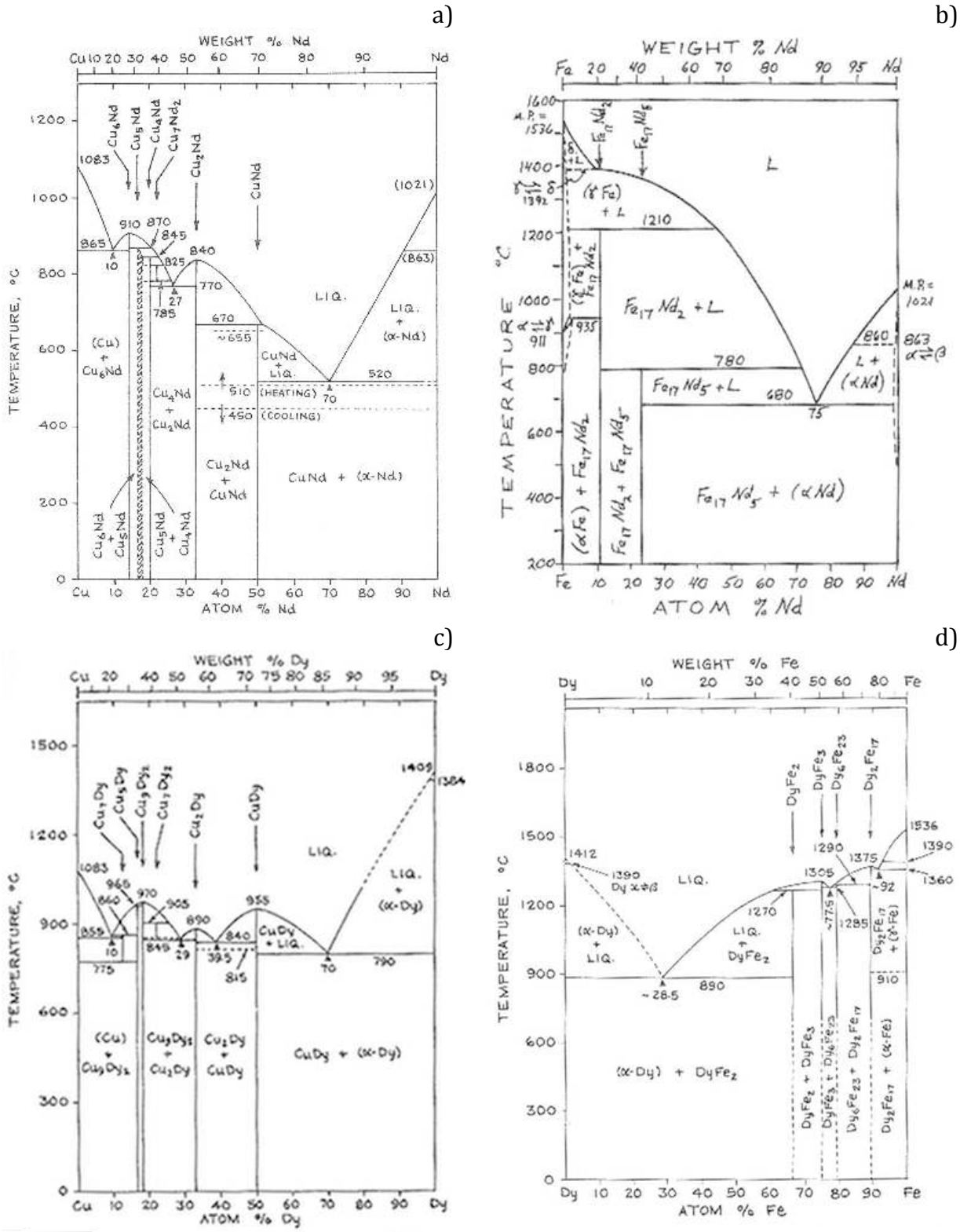

Fig. A8. 1 Phase diagrams for Cu-Nd (a), Fe-Nd (b), Cu-Dy (c), Fe-Dy (d).

Annex.9 Effect of Cu addition on the magnetic properties of NdFeB thick films

For samples presented in chapter V, Section V.3.1, atom probe analysis indicated the presence of Cu in the grain boundary phase (see Annex 7), though the amount of Cu in the films was too small to be detected by EDX. Here we will present results of a study where Cu was deliberately introduced into the film.

Before showing these results, the preparation of the films will be briefly described. In order to study the influence of Cu, the samples were deposited on a non-rotating wafer. In this way, the quantity of the deposited elements varies across the 10 cm diameter substrate. Samples with different Nd, Fe and Cu compositions, allowing a study of the influence of composition, can be obtained with only one deposition.

The variation of Nd/Fe across the substrate is a cumulative effect of: i) differences in the solid angle of sputtering for Nd and Fe and ii) an asymmetry of the distribution of the plasma, due to an asymmetry in the applied field that concentrates it, with respect to the center of the target and substrate. Results of a previous investigation of Nd/Fe ratio along the diameter of the substrate (**Fig. A9. 1**b), when only NdFeB material was deposited, are displayed in **Fig. A9. 1**a. The blue dotted line corresponds to the 2:14:1 phase.

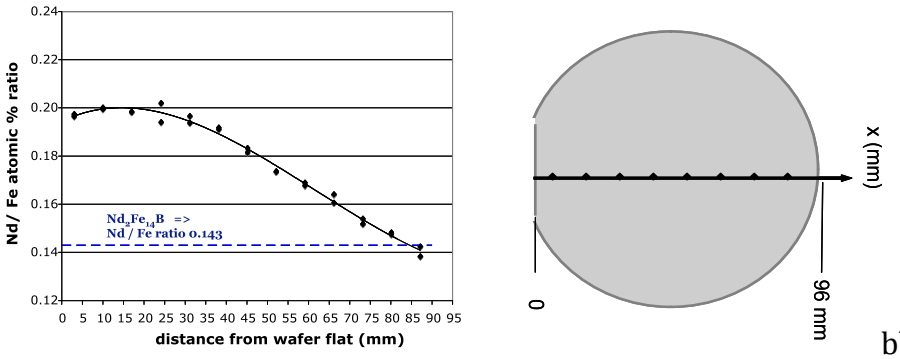

a) b)

Fig. A9. 1 Nd/Fe atomic ratio (a) measured along wafers' bisector (b).

The target that was used for NdFeBCu deposition is a Nd-rich NdFeB target ($Nd_{19.6}Fe_{72.5}B_{7.9}$) on which a small cylindrical piece of Cu was glued, as shown schematically in **Fig. A9. 2**.

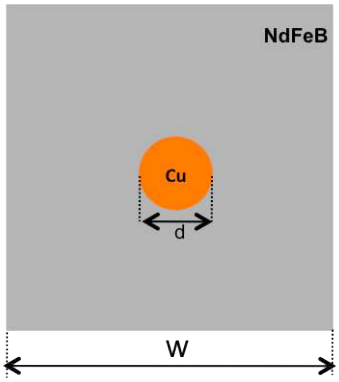

Fig. A9. 2 Schematics of the NdFeB-Cu target; d = 0.5 cm and w = 10 cm.

Two films were deposited, one before and one after adding the Cu piece. A part of the Cu-free film, corresponding to the maximum Nd/Fe ratio in **Fig. A9. 1**a (Nd/Fe ≈ 0.2), and its counterpart from the Cu-containing sample are discussed in parallel. The composition, measured before annealing on the second sample is: 16.2 at % Nd, 82.8 at % Fe and 1 at % Cu. The ratio of Nd to Fe content is similar for the Cu-free and Cu-containing samples.

The samples were annealed for 10 minutes at different temperatures. In **Fig. A9. 3** the demi-hysteresis loops for both samples, following annealing at 425 °C, 475 °C, 575 °C and 650 °C are shown. It can be seen that the sample that contains Cu presents higher coercivities at each temperature, except 425 °C where both samples are still amorphous. The optimum temperature is 575 °C for both samples, the coercivity decreasing at 650 °C. The eutectic temperature of Nd-Cu is 520 °C (see Annex 8). The evolution of coercivity with the annealing temperature is plotted in **Fig. A9. 3**b.

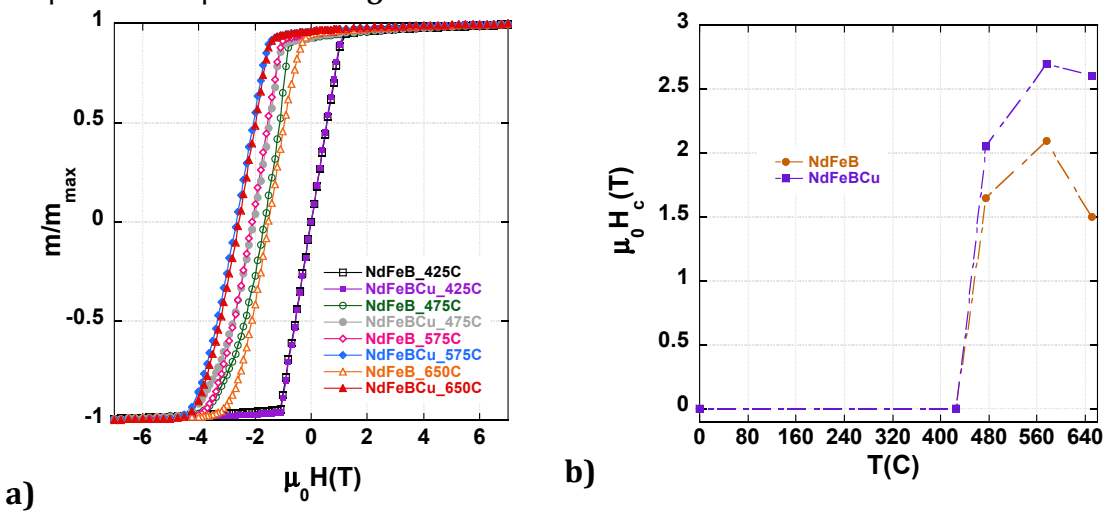

Fig. A9. 3 Hysteresis loops corresponding to Cu-free and Cu-containing samples annealed at 425 °C, 475 °C, 575 °C and 650 °C for 10min (a). Evolution of coercivity with the annealing temperature for Cu-free and Cu-containing sample (b).

SEM images taken on cross-sections of the two samples before annealing and after annealing at 475 °C and 575 °C are shown in **Fig. A9. 4**. It can be seen that the behavior of the films is quite similar at this scale: they are amorphous in the as-deposited state (**Fig. A9. 4**a and **Fig. A9. 4**b), crystalline after annealing at 475 °C (**Fig. A9. 4**c and **Fig. A9. 4**d) and crystalline with well defined grains after annealing at 575 °C (**Fig. A9. 4**e and **Fig. A9. 4**f). The last two images correspond to the samples with highest coercivities. The grains in the film with Cu are slightly more elongated along the direction perpendicular to the film that in the Cu-free sample. The bumps on top of the two films are a result of liquid Nd-rich phases being squeezed out during annealing. EDX analysis showed that in the case of the film containing Cu, the material in this bump is also rich in Cu.

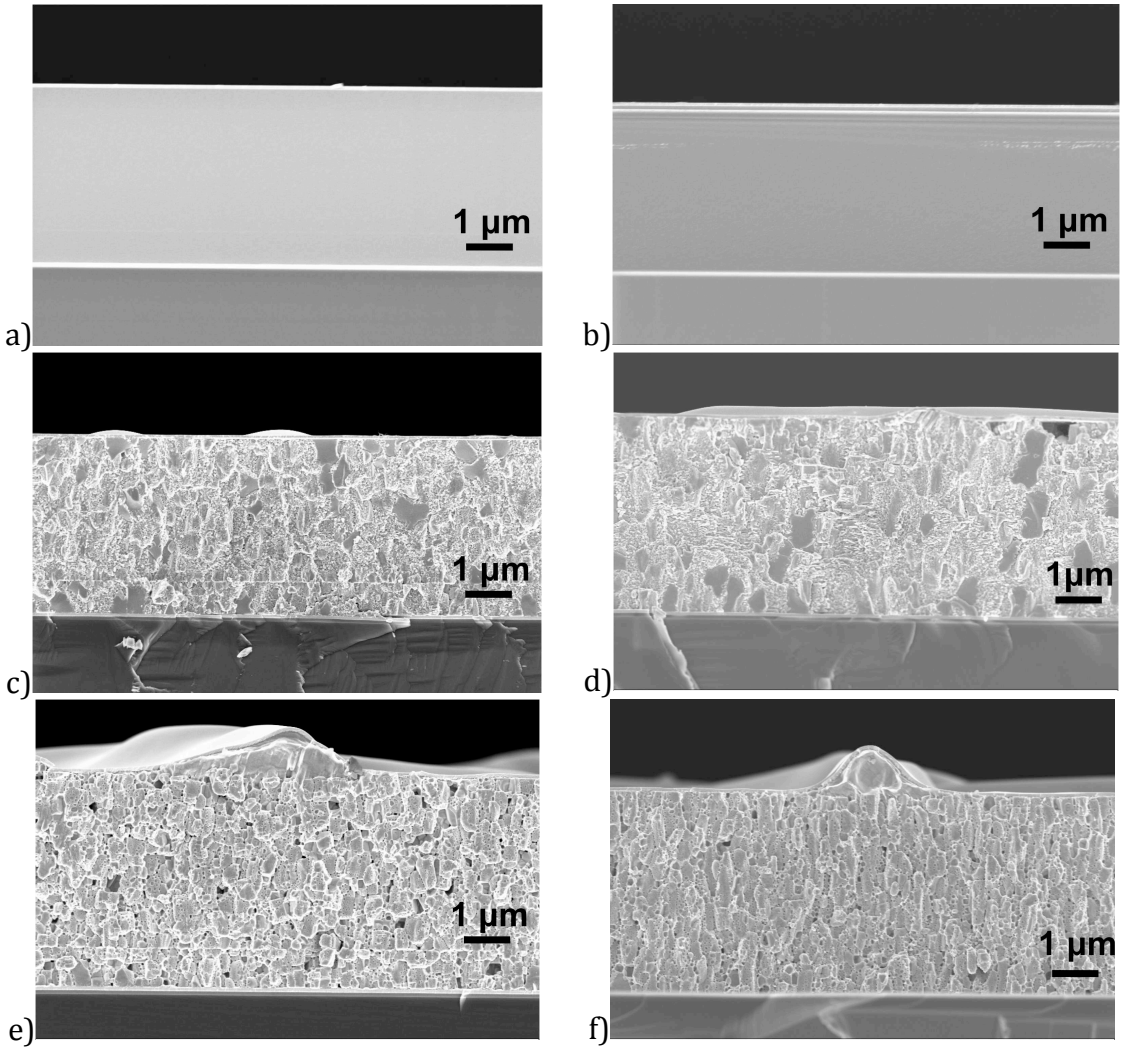

Fig. A9. 4 Cross - section SEM images of Cu-free and Cu-containing sample in the as deposited state (a and b), after annealing at 475 °C (c, d) and after annealing at 575 °C (e, f).

Measurements were performed on samples from different positions on the substrate. H_c is observed to increase in the Cu-containing sample with respect to the Cu-free sample, all over the substrate, but by different amounts. The variation of Nd/Fe ratio, Cu content and corresponding increase of coercivity for some points on the substrate are shown in **Fig. A9. 5**. The chemical composition investigation was performed using the EDX function of the electron microscope on amorphous, non-annealed Cu-containing samples. It is seen that the Cu content varies between 0.95 at % and 1.5 at %. The coercivity increases the most in the case of low Nd/Fe ratio and 0.95 at % Cu. Without Cu, the Nd/Fe ratio is not high enough to allow for the formation of sufficient inter-granular phases to decouple the grains. By adding Cu, the extra Nd is enough to form the Nd-Cu eutectic during annealing, decoupling better the grains and, as a result, increasing the coercive field value.

The samples with high Nd/Fe ratios present a smaller increase in coercivity because, even without Cu, the grains are already partially decoupled. Addition of Cu improves further the decoupling. Comparing two samples, with similar Cu content but different Nd/Fe ratio (center and bottom left rectangles in **Fig. A9. 5**), the coercivity is seen to increase more where there is more Nd. Thus, to

conclude, the effectiveness of Cu addition depends strongly on the amount of excess Nd in the film.

Magnetic remanence was estimated for the most favorable cases in terms of coercivity, and it decreases by about 5% with the addition of Cu.

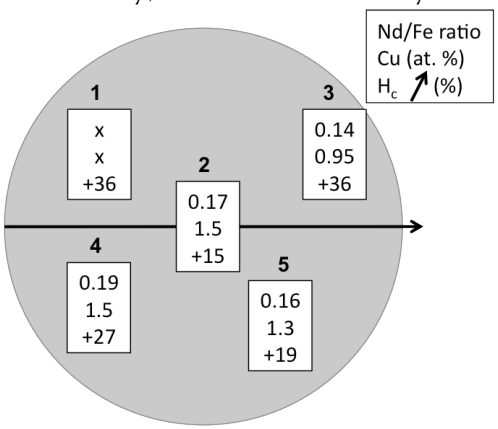

Pos.	H_c (T)_NdFeB	H_c(T)_NdFeBCu
1	1.8	2.46
2	2	2.3
3	1.5	2.05
4	2.1	2.66
5	1.68	2

Fig. A9. 5 Increase of coercivity (in percent) as a function of the position on the substrate. In the table on the right the respective values of coercivity are given.

Temperature dependent hysteresis measurements were made on two samples. The hysteresis loops between 200 K and 400 K are shown in **Fig. A9. 6**a for the Cu-free sample and **Fig. A9. 6**b for the sample with Cu. H_c was extracted for each case and the graphs of H_c as a function of temperature are displayed in **Fig. A9. 6**c and **Fig. A9. 6**d. In the second graph the values are normalized to the H_c value at 200 K. At 400 K, the sample with Cu has a coercive field value of 1.3T.

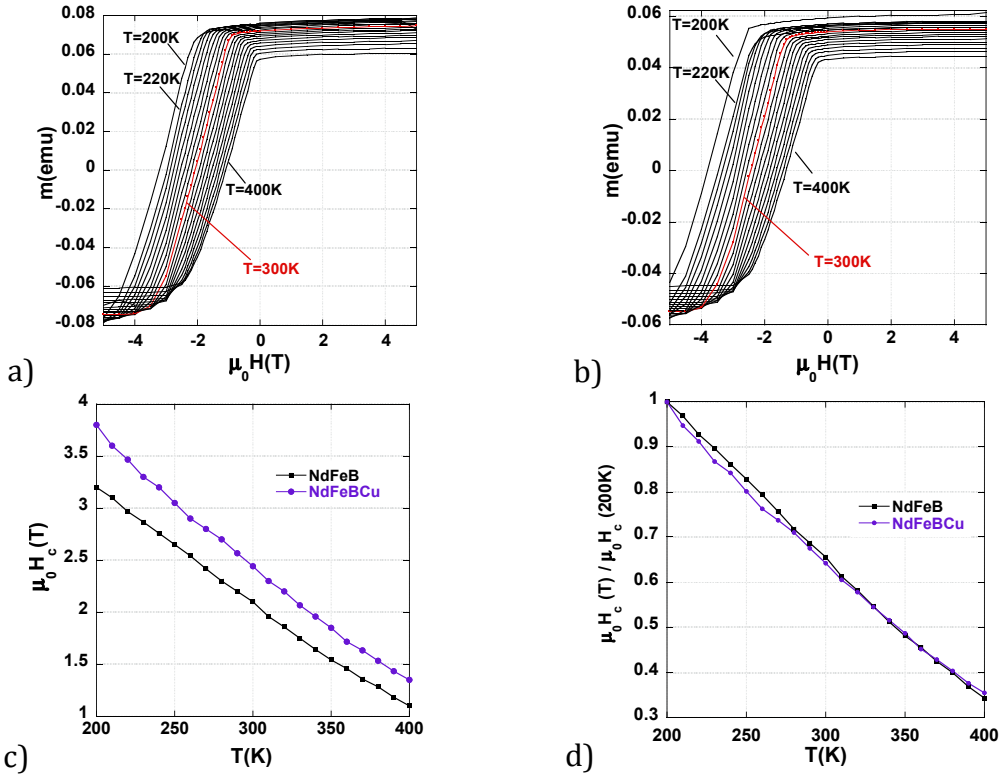

Fig. A9. 6 Hysteresis loops measured at temperatures between 200 K and 400 K for a Cu-free sample (a) and a Cu-containing sample (b); variation of coercive field with the measuring temperature (c) and H_c(T)/H_c(200 K) as a function of temperature (d).

So, room temperature coercivities up to 2.7 T were obtained in Dy-free, Nd-less* NdFeB-based thick films by adding Cu.

* Similar coercive field was obtained in NdFeB thick films with no Cu addition but with higher Nd content (Nd/Fe ratio ≈ 0.23)

Annex 10 TMC bulk samples data

Coercive field function of temperature

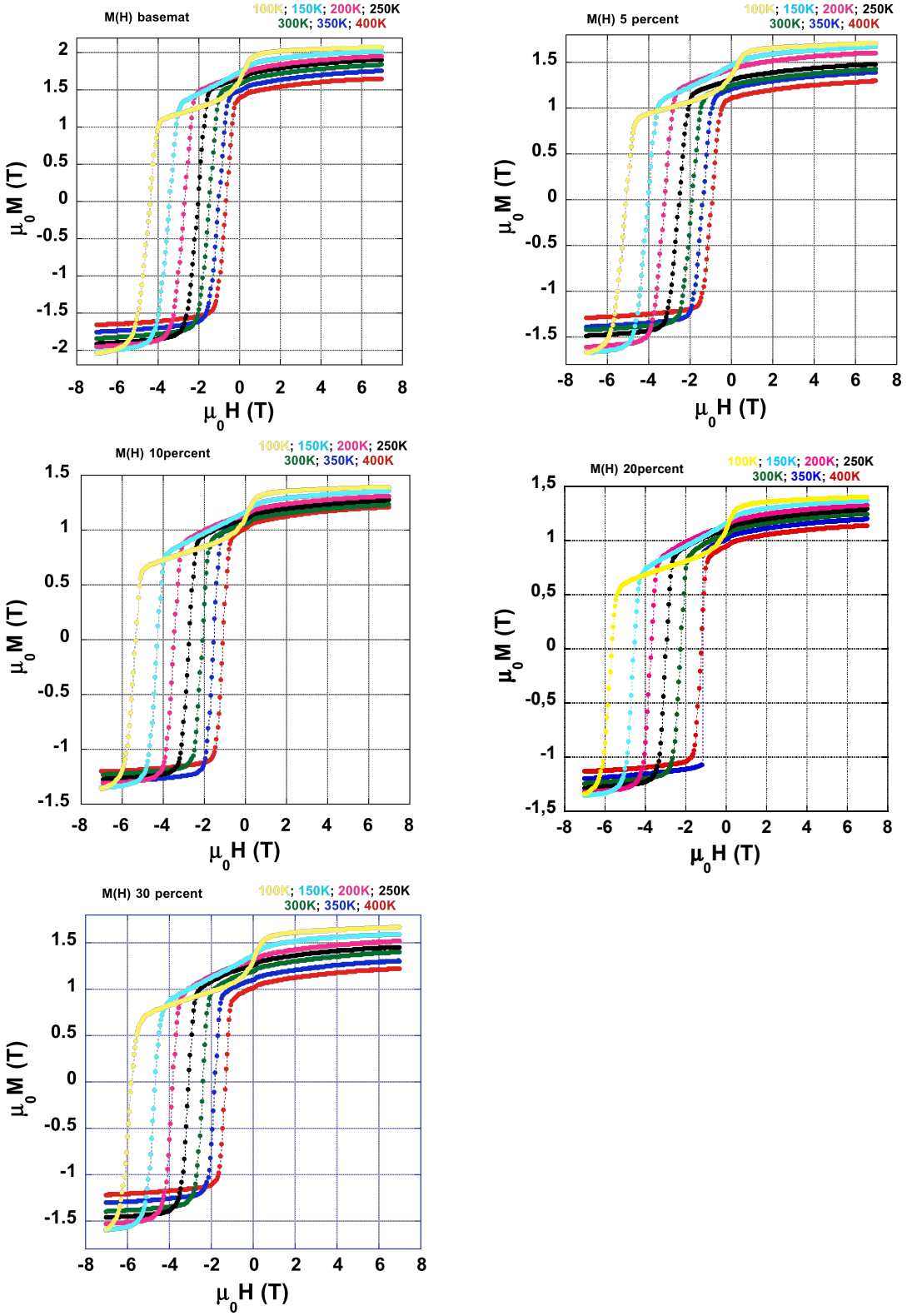

Fig. A10. 1 Hysteresis loops measured at different temperatures for the base material (a), 5 % infiltrated (b), 10 % infiltrated (c), 20 % infiltrated (d) and 30 % infiltrated (e).

The $H_c(T)$ for all the bulk samples are shown in **Fig. A10. 2**.

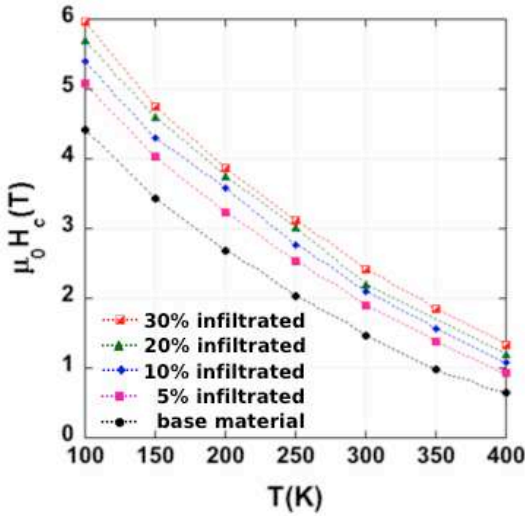

Fig. A10. 2 $H_c(T)$ for the series of 5 bulk samples.

The values from **Fig. A10. 2** are given in **Table A10. 1**.

T(K)	$H_c(T)$ Base material	5% infil.	10% infil.	20%infil.	30% infil.
400	0.65	0.94	1.08	1.2	1.34
350	0.98	1.38	1.57	-	1.84
300	1.46	1.9	2.1	2.2	2.42
250	2.04	2.53	2.76	3.01	3.1
200	2.7	3.24	3.58	3.75	3.87
150	3.44	4.04	4.3	4.6	4.75
100	4.41	5.09	5.4	5.7	5.96

Table A10. 1 Coercive values of bulk samples at different temperatures

The values of the calculated activation volume are given in **Table A10. 2**.

T(K)	$v_a(nm^3)$ Base material	$v_a(nm^3)$ 5% infil.	$v_a(nm^3)$ 10% infil.	$v_a(nm^3)$ 20% infil.	$v_a(nm^3)$ 30% infil.
400	550	527	531	508	558
350	403	392	404		417
300	334	317	309	305	325
250	245	242		238	233
200	167	163		163	144
150	103	103		93	81
100	60	60		42	33

Table A10. 2 Activation volume of the bulk samples, at different temperatures.

Abstract

Magnetization reversal in NdFeB-type permanent magnets was studied in this thesis, based on both global (magnetometry) and local (magnetic force microscopy) experimental techniques. Two types of samples were analyzed: bulk magnets of which magnetic properties are greatly improved as a result of NdCu infiltration along the grain boundaries (samples provided by Toyota Motor Corporation) and thick film magnets with different microstructures and thus different coercive fields. The temperature dependence of the coercive field and that of the activation volume were analyzed in the framework of two models: the micromagnetic and the global model. The derived values of the two main parameters characterizing coercivity (N representing demagnetizing field effects and α linking the coercive field to the intrinsic magnetic properties of the hard phase) indicate that, in bulk magnets, the difference in coercivity between different samples is related mainly to N whereas in films the parameter α plays the leading role. The activation volume derived from magnetic after effect measurements is similar for all bulk samples at a given temperature. On the opposite, it varies in the case of films: the higher the coercive field, the smaller the activation volume. Altogether, it is concluded that the magnetic properties within the activation volume are close to those of the main phase. The link between microstructure and coercivity was studied in thick films, using magnetic force microscopy. Imaging of films that present different microstructures was performed in different remanent states along the hysteresis cycle. Interaction domains were observed in the case of films with lower coercive field. In such low coercivity films, as well as in medium coercivity ones, magnetization reversal is dominated by domain wall propagation, instead of nucleation + propagation in high coercivity films.

Keywords: hard magnetic materials, coercivity, microstructure, magnetization reversal, interaction domains, micromagnetic model, global model, magnetic force microscopy (MFM).

Résumé

Les processus d'aimantation dans des aimants de type NdFeB ont été étudiés dans le cadre de cette thèse, sur la base de mesures d'aimantation macroscopiques et de caractérisations locales (MFM). Deux types d'échantillons ont été analysés : des aimants massifs dont les propriétés excellentes résultent d'un processus d'infiltration de NdCu le long des joints de grain (échantillons fournis par Toyota Motor Corporation) et des échantillons sous forme de couches épaisses, dont les microstructures, et, de ce fait les propriétés magnétiques, diffèrent. La variation thermique du champ coercitif et celle du volume d'activation ont été analysées dans le cadre de deux modèles, respectivement dénommé micromagnétique et global. Les valeurs déduites des deux paramètres principaux caractérisant la coercitivité (N représentant les effets du champ démagnétisant et α reliant le champ coercitif aux propriétés magnétiques intrinsèques de la phase dure) indiquent que dans les aimants massifs les différences de coercitivité entre échantillons sont dues pour l'essentiel à la variation de N alors que dans les films, c'est la variation du paramètre α qui joue le rôle principal. Le volume d'activation à une température donnée, dérivé de mesures de trainage magnétique, a des valeurs proches pour tous les échantillons massifs. Au contraire, il varie d'un échantillon à l'autre dans le cas des films : plus le champ coercitif est fort, plus petit est le volume d'activation. Une conclusion générale de cette étude est que les propriétés magnétiques au sein du volume d'activation sont proches de celles de la phase dure $Nd_2Fe_{14}B$. Le lien entre microstructure et coercivité a été examiné dans les films épais par microscopie de force magnétique (MFM). Des observations de films dans différents états rémanents le long du cycle d'hystérésis ont été réalisées. Des « domaines d'interactions » ont été révélés dans les films de faible coercitivté. Dans de tels films, comme dans ceux de coercitivité moyenne, le renversement d'aimantation est dominé par la propagation de domaines, alors que dans les films de plus forte coercitivité, la nucléation suivie de la propagation de domaines d'orientation inverse à celle de l'aimantation principale dominent.

Mots-clés : matériaux magnétiques durs, coercitivité, microstructure, renversement d'aimantation, domaines d'interaction, modèle micromagnétique, modèle global, microscopie de force magnétiques (MFM).